

**LOOP RADIOFREQUENCY COILS FOR CLINICAL  
MAGNETIC RESONANCE IMAGING AT 7 TESLA**

Oliver Kraff

Erwin L. Hahn Institute for Magnetic Resonance Imaging



# LOOP RADIOFREQUENCY COILS FOR CLINICAL MAGNETIC RESONANCE IMAGING AT 7 TESLA

DISSERTATION

to obtain

the degree of doctor at the University of Twente,

on the authority of the rector magnificus,

prof.dr. H. Brinksma,

on account of the decision of the graduation committee,

to be publicly defended

on Wednesday, June 22<sup>nd</sup>, 2011 at 14.45

by

**Oliver Kraff**

born on November 07, 1977

in Mönchengladbach, Germany

Promoter: Prof. Dr. rer. nat. David G. Norris

Co-Promoter: Prof. Dr. rer. med. Harald H. Quick

The studies presented in this thesis were performed at the Erwin L. Hahn Institute for Magnetic Resonance Imaging in Essen, Germany.

ISBN: 978-90-365-3163-4

Copyright © 2011 by Oliver Kraff, all rights reserved.

The copyright of the articles and illustrations that have been published or accepted for publication has been transferred to Investigative Radiology, Wolters Kluwer Health, Baltimore, MD, and to Medical Physics, American Institute of Physics, College Park, MD. The author has obtained the rights for their reproduction in this thesis.

Printed by: Universitätsdruckzentrum Duisburg-Essen, Duisburg, Germany

*For my parents.*



# Contents

<b>List of Original Publications</b>	<b>8</b>
<b>1 Introduction</b>	<b>9</b>
1.1 A brief historical survey of MRI	9
1.2 Principles of magnetic resonance imaging	12
1.3 The RF System	17
1.4 Objective of this thesis	23
<b>2 High-Resolution MRI of the Human Parotid Gland and Duct at 7 T</b>	<b>28</b>
2.1 Introduction	29
2.2 Material and Methods	31
2.3 Results	34
2.4 Discussion	43
<b>3 An Eight-Channel Phased Array RF Coil for Spine MR Imaging at 7 T</b>	<b>50</b>
3.1 Introduction	51
3.2 Material and Methods	53
3.3 Results	58
3.4 Discussion	65
<b>4 A Transmit/Receive RF Array for Imaging the Carotid Arteries at 7 T: Coil Design and First In-Vivo Results</b>	<b>71</b>
4.1 Introduction	72
4.2 Material and Methods	74
4.3 Results	78
4.4 Discussion	87
<b>5 An Eight-Channel Transmit/Receive Multi-Purpose Coil for Musculoskeletal MR Imaging at 7 T</b>	<b>96</b>
5.1 Introduction	97
5.2 Material and Methods	99
5.3 Results	104
5.4 Discussion	113
<b>6 Summary</b>	<b>122</b>
<b>7 Samenvatting</b>	<b>124</b>
<b>Acknowledgements</b>	<b>126</b>
<b>Curriculum Vitae</b>	<b>129</b>

## List of Original Publications

Portions of this thesis are published in the following international peer-reviewed journal articles with the author of this thesis as first author:

**Kraff O**, Theysohn JM, Maderwald S, Kokulinsky PC, Dogan Z, Kerem A, Kruszona S, Ladd ME, Gizewski ER, Ladd SC. High-resolution MRI of the human parotid gland and duct at 7 Tesla. *Investigative Radiology*, September 2009; 44(9): 518-524. Impact factor: 4.850

**Kraff O**, Bitz AK, Kruszona S, Orzada S, Schaefer LC, Theysohn JM, Maderwald S, Ladd ME, Quick HH. An eight-channel phased array RF coil for spine MR imaging at 7 T. *Investigative Radiology*, November 2009; 44(11): 734-740. Impact factor: 4.850

**Kraff O**, Bitz AK, Dammann P, Ladd SC, Ladd ME, Quick HH. An eight-channel transmit/receive multi-purpose coil for musculoskeletal MR imaging at 7 Tesla. *Medical Physics*, December 2010; 37(12): 6368-6376. Impact factor: 2.704

**Kraff O**, Bitz AK, Breyer T, Kruszona S, Maderwald S, Brote I, Gizewski ER, Ladd ME, Quick HH. A transmit/receive RF array for imaging the carotid arteries at 7 Tesla: Coil design and first in-vivo results. *Investigative Radiology*, 2011; 46(4): 246-254. Impact factor: 4.850

Additionally, another article has been published as first author which is not part of this thesis:

**Kraff O**, Theysohn JM, Maderwald S, Saylor C, Ladd SC, Ladd ME, Barkhausen J. MRI of the knee at 7.0 Tesla. *RöFo–Fortschritte auf dem Gebiet der Röntgenstrahlen und der bildgebenden Verfahren*, December 2007; 179(12): 1231-1235. Impact factor: 2.025



# Chapter 1 Introduction

## 1.1 A brief historical survey of MRI

Since William Roentgen first discovered the x-ray phenomenon in 1895 <sup>1</sup> medical imaging techniques have become an irreplaceable tool in the diagnosis, prediction and treatment supervision of diseases. Thereby, magnetic resonance imaging (MRI) is recognized as one of the most important advances in medicine of the last century. It has revealed non-invasively three-dimensional anatomical information of the human body with a level of detail that would have been unimaginable only decades ago.

Looking back to the origin of MRI, the synergy between nuclear magnetic resonance (NMR) chemistry and x-ray imaging has laid the foundations for the development of MRI. NMR is a property of magnetic nuclei with an angular and magnetic moment in an external magnetic field where they absorb or irradiate electromagnetic energy at a certain frequency. This phenomenon was first observed by Edward Purcell, and independently Felix Bloch who, therefore, were both awarded with the Nobel Prize for Physics in 1952 <sup>2-3</sup>. Interest in the potential of NMR for medical diagnostic purposes began in 1971, when Raymond Damadian studied the differences in relaxation times between normal and cancerous tissue <sup>4</sup>. In 1973, Paul Lauterbur presented a 2-dimensional NMR image of a water-filled structured object. Being familiar with projection-reconstruction techniques used in computerized tomography (CT), Lauterbur could reconstruct this cross-sectional image out of a number of 1-dimensional NMR measurements each obtained under a linear field gradient with a different direction. This process was first described as “Zeugmatography” <sup>5</sup>, meaning “that which joints together”, namely static magnetic fields and radiofrequency (RF) fields for imaging. Paul Lauterbur was awarded the Nobel Prize for medicine in 2003 together with Sir Peter Mansfield, another pioneer in MRI. Thus, the synergy between NMR and x-ray imaging has led to a remarkable diagnostic tool, which has

experienced a rapid and significant technical advancement and has had an enormous impact on the practice of medicine.

The first clinical MR systems were installed in 1983 at low field strengths of 0.35-0.5 Tesla (T) <sup>6</sup>, followed by the development of 1 T and 1.5 T magnets. Over the past 25 years, these two have been the main field strengths in clinical settings. Over the last 10 years, 3 T MR scanners were introduced as a clinical modality. Increasing the magnet field strength has always been the driving force for improving the capabilities of MRI since the signal-to-noise-ratio (SNR) scales approximately linearly with the field strength. This makes it possible either to invest the increased SNR into reducing scan time or to obtain higher spatial resolution, for example. After the successful development of an 8 T MRI system at the Ohio State University in 1998, the first 7 T magnet was installed in the Center for Magnetic Resonance Research at the University of Minnesota in 1999, followed by the second 7 T system, which is in operation at the Massachusetts General Hospital in Boston since 2002. Numerous installations followed over the last decade, among them the 7 T system at the Erwin L. Hahn Institute for Magnetic Resonance Imaging in Essen in October 2006. Currently, there are approximately 40 research systems in operation worldwide. Due to strong inhomogeneities of the transmit  $B_1$  field at 7 T, for a long time the main focus of investigations was on the brain, where the artifacts were still acceptable. However, for the last two years more advances in whole-body imaging have facilitated the very first abdominal images at 7 T <sup>7-9</sup>.

Although even higher magnetic field strengths of 9.4 T <sup>10</sup> and higher are currently explored, 7 T seems to have become a standard in human whole-body MR research. The 7 T magnets with a 900 mm bore allow the use of standard clinical gradient coils and other components of the technical periphery. They are becoming generally more affordable and active-shielded magnets have been recently introduced which solve limitations in finding suitable sites and building costs, since they must otherwise be surrounded by enormous amounts of steel for passive magnetic field shielding. For example in Essen, the steel shielding weighs 430 tons with wall dimensions in the thickest sections exceeding 50 cm. With the U.S. Food and Drug Administration

(FDA) currently reviewing patient use of 7 T MRI as well as the recent technical advances in whole-body MRI at 7 T <sup>7-9</sup>, it is likely that 7 T will be considered for clinical diagnostics in selected applications in the very near future.

## 1.2 Principles of magnetic resonance imaging

### *Spins and magnetization*

Atomic nuclei are composites of protons and neutrons which themselves composites of fundamental particles, quarks, which possess a quantum mechanical property called spin. Depending on the type of the particle, the spin or spin quantum number can take half-integer (fermions) or integer (bosons) values. In a classical view, the spin can be thought of as a rotation of the particle around some axis. All quarks are fermions and neutrons and protons are each made up of three quarks (neutron: one up-, two down-quarks; proton: two up-, one down-quark), resulting again in a spin- $\frac{1}{2}$  system. Hence, all atomic nuclei with an odd number of protons and neutrons, which is roughly two-thirds of all stable atomic nuclei, possess a non-zero spin angular momentum  $S$ . Since quarks are electrically charged particles (e.g., the up-quark has a charge of  $+\frac{2}{3} e$ ; the down-quark of  $-\frac{1}{3} e$ ), the neutron or proton spin can be thought of as leading to a circulating electric current, and, hence, an associated magnetic moment

$$\vec{\mu} = \gamma \vec{S}. \quad (1.1)$$

The proportionality constant  $\gamma$  is called the gyromagnetic ratio and depends on the nucleus. Due to its huge abundance in humans, the hydrogen nucleus  $^1\text{H}$  is an ideal candidate for MRI. For  $^1\text{H}$ ,  $\gamma$  or more commonly known  $\gamma = \frac{\gamma}{2\pi}$  has a value of 42.58 MHz/T.

As a consequence of the non-zero spin momentum, these atomic nuclei possess potential energy in a magnetic field and magnetic resonance can be observed. According to quantum mechanics only discrete energy levels are allowed. In an external magnetic field of flux density  $\vec{B}_0$ , by convention applied along the z-direction, a nucleus with spin quantum number  $S$  may assume  $2S + 1$  discrete energy levels, called eigenstates

$$E_m = -\gamma\hbar B_0 m \quad (1.2)$$

with the reduced Planck's constant  $\hbar = h/2\pi = 1.05510^{-34} \text{ W s}^2$  and magnetic quantum number  $m$  ( $-S \leq m \leq S$ ). As shown in Fig. 1.1, the magnetic field causes  $S_z$  to be aligned either parallel or antiparallel to  $\vec{B}_0$ , and, hence, each eigenstate corresponds to a precession of the magnetic moment  $\vec{\mu}_z = \gamma S_z$  around the z-axis at a fixed angle. The energy difference between two possible eigenstates is

$$\hbar\omega = E_{m-1} - E_m = -\gamma\hbar B_0 \quad (1.3)$$

which is the resonance condition. The characteristic precession frequency of the magnetic moment of the nucleus  $\omega = \gamma B_0$  is called the Larmor frequency.

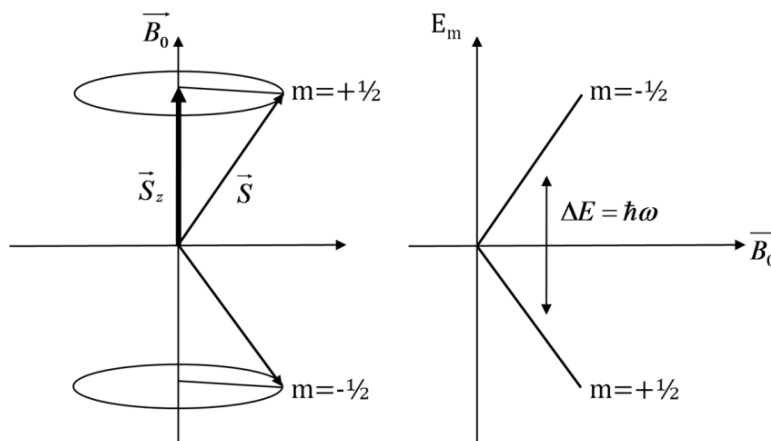


**Fig. 1.1** – Left: Orientations and precessions of a spin  $S = 1/2$  in a magnetic field  $B_0$ . Right: Energies of a spin  $S = 1/2$  as a function of  $B_0$ , where, according to equation (1.2), the eigenstate with a magnetic moment parallel to  $B_0$  has the lower energy. For a quantum transition,  $\Delta E$  has to be added or subtracted in form of electromagnetic quanta  $\hbar\omega$ .

Since nuclei do not occur as single spin systems but as large entities, the occupancy  $N$  of eigenstates can be described by Boltzmann statistics

$$\frac{N_{m-1}}{N_m} = e^{-\frac{\hbar\omega}{kT}} \quad (1.4)$$

with  $k$  being the Boltzmann's constant,  $k = 1.38 \cdot 10^{-23} \text{ WsK}^{-1}$ . Hence, there are more spins aligned parallel to  $\vec{B}_0$ , resulting in a small but measurable macroscopic magnetic moment along  $\vec{B}_0$ . This equilibrium magnetization is called longitudinal magnetization, which for  $^1\text{H}$  is given by

$$\vec{M}_0 = \frac{\rho\gamma^2\hbar^2\vec{B}_0}{4kT} \quad (1.5)$$

where  $\rho$  is the proton spin density. It is the maximum available magnetization for the formation of the MRI signal.

### *Spin excitation and relaxation*

The longitudinal magnetization can be perturbed from equilibrium by applying an external, transverse RF field  $\vec{B}_1$  with a rotational frequency that meets the resonance condition. Hence, individual spins in the system will undergo a state transition. If a  $B_1$  pulse is applied for time  $\tau = \pi/(2\omega_1)$ , i.e. a  $90^\circ$  pulse, the magnetization vector will be rotated into the transverse plane x-y. For a realistic pulse time of  $\tau = 1 \text{ ms}$ , for example, the value of  $B_1$  can be calculated to  $6 \mu\text{T}$  for a  $90^\circ$  excitation.

The notation of the  $\vec{B}_1$  field is commonly split up in a portion that rotates with the Larmor frequency along with the precession of the magnetic moment of the spin system ( $\vec{B}_1^+$ ) and a portion that rotates in the opposite direction ( $\vec{B}_1^-$ )

$$\vec{B}_1^+ = \frac{\vec{B}_{1,x} + i\vec{B}_{1,y}}{2} \quad (1.6)$$

$$\vec{B}_1^- = \frac{(\vec{B}_{1,x} - i\vec{B}_{1,y})^*}{2} \quad (1.7)$$

where  $i = \sqrt{-1}$ .  $\vec{B}_1^+$ ,  $\vec{B}_1^-$ ,  $\vec{B}_{1,x}$ , and  $\vec{B}_{1,y}$  are complex vectors and the symbol \*

indicates the conjugate of a complex quantity.  $\vec{B}_1^+$  is referred to as the local transmit RF field, and  $\vec{B}_1^{-*}$  is referred to as the local receive field.

After the excitation pulse, the magnetization  $\vec{M}$  starts to precess around  $\vec{B}_0$  with  $\omega_0$ , meaning that the changing magnetic flux can induce a measurable voltage in a conducting loop, placed orthogonal to  $\vec{B}_0$ . This voltage is the MR signal, called free induction decay (FID), which decays after some time due to relaxation.

The process of restoring thermal equilibrium of the magnetic moment  $M_0$  is called spin relaxation, which is determined by two time constants  $T_1$  and  $T_2$ . The  $T_1$  time constant describes the recovery of the longitudinal  $M_z$  component of the magnetization vector, referred to as spin-lattice relaxation. Thus, energy is transferred from the spin system to its environment. The  $T_2$  time constant describes the decay of the transverse  $M_{xy}$  component of the magnetization vector, referred to as spin-spin relaxation. The spin-spin interaction describes the loss of phase coherence of spins as they interact with each other via their own oscillating magnetic fields. As a result, the precession of spins moves out of phase and the overall transverse magnetization is reduced. While  $T_2$  includes only irreversible causes of dephasing, magnetic field inhomogeneities and susceptibility effects cause variations in the local magnetic field experienced by nuclear spins which leads to a much faster dephasing, described by the time constant  $T_2^*$ .  $T_2$  and  $T_2^*$  are related by the equation

$$\frac{1}{T_2^*} = \frac{1}{T_2} + \frac{1}{T_2'} \quad (1.8)$$

with  $T_2'$  being the characteristic time representing signal decay from local magnetic field inhomogeneities. As the system reaches equilibrium, the transverse magnetization will inevitably diminish to zero, and, therefore  $T_2^* \leq T_2 \leq T_1$  always holds.

There is a wide range of relaxation times in biological tissue, producing high levels of contrast and the different relaxation times involved enable one to clearly depict pathological areas. Additionally, relaxation times can be shortened dramatically by

introducing small concentrations of paramagnetic ions which expands the tools for medical diagnostics in MRI even further <sup>11</sup>.

For an in-depth description of spin dynamics and quantum mechanics the reader is referred to standard text books <sup>12-13</sup>.



## 1.3 The RF System

### *Transmitter and Receiver*

The task of the RF system is twofold. First, the RF transmitter (Tx) generates a  $B_1$  field that rotates the magnetization of the spin system away from the  $B_0$  axis at an angle  $\alpha$  determined by the strength and pulse duration  $\tau$  of the  $B_1$  field. Therefore, the Tx path of the MR system delivers amplitude and phase-controlled RF pulses to one or more RF antennas, called RF coils. The individual RF transmitter signals must be amplified to kW power levels by the RF power amplifier (RFPA) which consists of one or more RF driver stages and amplifiers as well as directional couplers for output power monitoring. The maximum power required for MRI scales as

$$P_{max} \propto \frac{\alpha^2 \omega^2}{\tau^2}. \quad (1.9)$$

The second task is to pick up the signal of the excited spin system, which is performed by the receive system (Rx). When considering a rectangular RF pulse of constant amplitude and duration, the measured image signal intensity SI can be written as

$$SI \propto \rho |\vec{B}_1^-|^* | \sin(V |\vec{B}_1^+| \gamma \tau) \quad (1.10)$$

with  $V$  being a dimensionless scaling factor proportional to the RF coil driving voltage. The Rx path consists of signal conditioning electronics, including low noise amplifiers (LNA), coil element selectors, RF receivers and automatic signal level adjustments. A large number of independent receiver channels for imaging based on RF phased array coils is advantageous. Array coils provide a superior SNR and allow for parallel acquisition techniques (PAT) to shorten image acquisition time<sup>14-16</sup>.

The SNR in a MR image is substantially influenced by the RF coil that receives the signals. In clinical MR systems, a volume RF transmit body coil generates the exciting  $B_1$  fields and dedicated RF receive-only coils pick up the signals from the

patient's body. At 7 T, however, no such body coil is integrated into the system due to technical limitations and each local coil must include RF transmit and receive capabilities. Hence, components such as transmit/receive (T/R) switches, hybrids and preamplifiers may be included.

### *The RF coil*

The RF coil generates a spatially dependent  $\vec{B}_1(\vec{r})$  field by an electrical current ( $I$ ) flow through a conductor. Strength and orientation of this field can be calculated using the law of Bio-Savart

$$\vec{B}_1(\vec{r}) = \frac{\mu_0 I}{4\pi} \int \frac{d\vec{l} \times \vec{r}}{|\vec{r}|^3} \quad (1.11)$$

where  $\vec{r}$  is the displacement vector in the direction pointing from the conductor element towards the point at which the magnetic field is being computed, the magnitude of  $d\vec{l}$  is the length of the differential element of the conductor, and  $\mu_0$  is the magnetic permeability constant in vacuum ( $\mu_0 = 4\pi \cdot 10^{-7} \text{ NA}^{-2}$ ).

For optimal transformation of RF power from the amplifier through coaxial cables into current through the conductors of the RF coil, impedance matching is mandatory; i.e., at the single frequency  $\omega_0$  the conjugated impedance ( $Z^*$ ) of the amplifier matches the transformed impedance ( $Z$ ) of the conductor, typically  $50 \Omega$ . Impedance is defined as the frequency domain ratio of the voltage to the current and can be split into a real part, resistance  $R$ , and a complex quantity, the reactance  $X$ . The resistance of the conductor consists of three parts: (1) the coil's ohmic resistance  $R_\Omega$  that depends on conductivity, as well as length and cross-section of the conductor, including skin effects at high operating frequencies; (2) radiation losses  $R_r$  which increase with the fourth power of frequency and square of the coil's area; and (3) tissue losses  $R_t$  that represent power being absorbed in conductive tissue due to  $B_1$  field-induced eddy-currents and electric field displacement currents (rises approximately quadratic with

frequency). While the inductive tissue losses are principally unavoidable, dielectric losses are associated with the distributed capacitance of the RF coil and should be minimized in the design process. Due to this strong frequency-dependence of R, RF engineers face more challenges at high magnetic fields<sup>17-18</sup>. The reactance can be capacitive (capacitance C),  $X_C = -(\omega C)^{-1}$ , or inductive (inductance L),  $X_L = \omega L$ , and when

$$\omega = \frac{1}{\sqrt{LC}} \tag{1.12}$$

both reactances cancel each other out. The ability of reactances to transform impedances is used for impedance matching.

The total impedance of a conductor  $Z = R_{\Omega} + R_r + R_t + i\omega L$  can be transformed to the impedance of the RF amplifier through a capacitive network using two capacitors as shown in Fig. 1.2. If a capacitor  $C_t$  is connected in parallel with the conductor, at some frequency  $\omega_a$  this parallel impedance  $Z_p$  can be the desired impedance of 50  $\Omega$ . By adding another capacitor  $C_m$  in series with the conductor, the reactance of this serial impedance may annul the reactance of  $Z_p$  at  $\omega_a$ , leaving simply to tune the parallel capacitor so that  $\omega_a$  is the Larmor frequency. Hence,  $C_m$  is commonly called the matching and  $C_t$  the tuning capacitor.

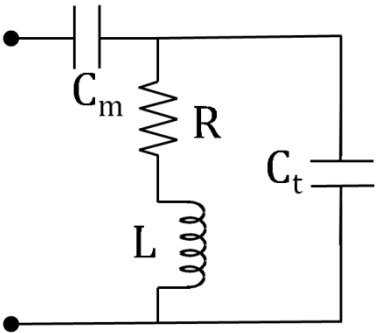


**Fig. 1.2** – A matching network using two capacitors  $C_m$  and  $C_t$  to transform the coil impedance to any desired impedance, in particular to the 50  $\Omega$  impedance of the RF amplifier.

Single surface coils offer high SNR but are limited in their field-of-view (FOV). This limitation can be overcome by deploying an array<sup>19</sup> of several surface coil elements with the signal of each element being independently fed into a separate receiver channel. This approach ensures that the high SNR of each array element is

preserved while the array offers a much larger FOV. However, the phased array depends on minimizing coupling and thus of noise correlation and power dissipation among the elements of the array. When two RF coils are brought close to another, the alternating field of one coil can pass through the other, inducing an electromotive force with a voltage that depends, among other factors, on the degree of coupling  $k$  between them. The factor describing current in one coil and induced voltage in the other is termed mutual inductance  $M$  with  $M^2 = k^2 L_1 L_2$ , where  $L_1$  and  $L_2$  are the two inductances. Inductive decoupling by carefully choosing the optimal element overlap so that the total flux generated by coil 1 and induced into coil 2 is zero, is the most common technique to minimize  $k$ .

### *RF heating*

According to Maxwell's equations, a time-varying magnetic field  $\vec{B}$  is always surrounded by closed  $\vec{E}$  field lines:

$$\vec{\nabla} \times \vec{E} = -\frac{\partial}{\partial t} \vec{B} \quad (1.13)$$

For a homogeneous magnetic field  $B_1$  varying harmonically in time, equation (1.13) yields after integration over an arbitrary area

$$2\pi r E = -\pi r^2 \omega B_1 \quad (1.14)$$

The electric field  $\vec{E}$  causes eddy currents of density  $\vec{j} = \sigma \vec{E}$  inside conductive tissue (conductivity  $\sigma$ ), such as the human body, which amounts to a power deposition of

$$P = \int \sigma E^2 dV = \frac{1}{4} \sigma B_1^2 \omega^2 \int r^2 dV \quad (1.15)$$

in a volume  $V$ . The electric power losses are proportional to the  $B_1$  field and Larmor frequency squared (same as equation 1.9) and can create heat in the human body.

Given that tissue temperatures are normally not accessible during MRI examinations, the RF power absorbed per kilogram of tissue, termed specific absorption rate (SAR), is used to set safety limits for in vivo imaging. The SAR within the exposed tissue of density  $\rho$  can be expressed as

$$\text{SAR} = \frac{\sigma}{\rho} E^2 \propto B_1^2 \omega^2 \quad (1.16)$$

Hence, doubling the magnetic field or pulse flip angle will quadruple the SAR, introducing major limitations for MRI at high field strengths, especially for short high peak power  $180^\circ$  pulses as used in the workhorse for clinical imaging: the turbo spin echo sequence<sup>20</sup>.

National and international standards, for instance the IEC standard 60601-2-33<sup>21</sup>, have been introduced to restrict the exposure of humans to RF heating by defining limits for the MR system. The SAR may not exceed 4 W/kg for body and 3.2 W/kg for head imaging. Local maxima in SAR (averaged over 10 g of tissue) are allowed up to 10 W/kg for head and trunk and up to 20 W/kg for the extremities.

Numerical simulations are used to describe the transmit RF field and its interaction with the human body. The most commonly used computational electrodynamics modeling technique for MRI is the Finite Difference Time Domain (FDTD)<sup>22</sup> approach, which solves the discretized, time-dependent Maxwell equations on a regular grid of voxels in an iterative way until a steady state is reached. Realistic voxel models of the human body enable one to determine the complex SAR distribution within the exposed part of the body. Additionally, in the first place, the simulations assist in optimizing a RF coil design for a specific application. This is of special importance since the wavelength is significantly shorter at 7 T compared to clinical field strengths of up to 3 T, and, hence, interference effects become more pronounced, resulting in strong signal inhomogeneities or even complete destructive interferences of the  $B_1$  field in some regions. Therefore, to obtain a homogenous  $B_1$  field in the anatomical region of interest, with an amplitude sufficient large enough to

turn the magnetization with a desired angle away from  $B_0$ , and to remain within the SAR limits is the biggest challenge for high field MRI with regards to the RF field.

For more information on MR systems, its components and functionality the reader may be referred to <sup>23-24</sup>.

## 1.4 Objective of this thesis

The aim of this thesis is to develop and investigate new techniques for 7 T MR imaging of the human body, with a strong focus on clinically oriented imaging outside the brain. For most of the studies, novel RF coils for signal transmission and reception are developed, thoroughly characterized, and tested with specially optimized sequences. The potential of 7 T imaging is discussed in the context of in vivo images of healthy volunteers as well as patients with known pathologies.

First, in chapter 2, a single loop coil is used to investigate 7 T MRI of the parotid gland and duct as an alternative to conventional sialography. Compared with 1.5 T images, it is demonstrated, that 7 T provides excellent image contrast and resolution, rendering very fine branches of the duct. An optimized scan protocol is proposed offering a non-invasive examination within 30 minutes.

To facilitate large field-of-view imaging of the spinal cord with high spatial resolution, a novel RF phased array coil is presented in chapter 3. Large FOV imaging is important for assessing patients with metastases or multiple sclerosis lesions in the spinal cord, for example. The prototype is characterized in numerical simulations and bench measurements. In vivo images demonstrate very high resolution in fine anatomical details, rendering it a promising new application in 7 T clinical research.

Since atherosclerosis causes high morbidity and disability worldwide, exploring the potential benefits of 7 T MRI to identify high-risk patients is obviously suggested. In chapter 4, a RF phased array coil for imaging the carotid arteries is introduced. The characterization of the coil is thoroughly described in numerical simulations, bench and phantom MR measurements. In vivo images reveal good signal excitation of both sides of the neck and a high vessel-to-background image contrast even without the administration of contrast media.

Although MRI plays a leading diagnostic role in assessing the musculoskeletal system and imaging of the knee at 7 T has already been published early in 2006, there are still no RF coils present to cover most of the major joints. A multi-purpose RF coil for imaging the musculoskeletal system is presented in chapter 5, including

coil characterization and performance tests and a comprehensive safety assessment. High-resolution images of all major joints, especially of the thus far neglected elbow and shoulder joints, which have been imaged for the first time at 7 T, are given.

Chapters 2 to 5 are in the form of already published work. All results and RF coils are currently used for further clinical studies <sup>25-27</sup> by the Department of Diagnostic and Interventional Radiology and Neuroradiology, University Hospital Essen.

The last chapter provides a brief summary and discussion.



## References

1. Knutsson F. Rontgen and the Nobel Prize. The discussion at the Royal Swedish Academy of Sciences in Stockholm in 1901. *Acta Radiol Diagn (Stockh)*. Sep 1974;15(5):465-473.
2. Purcell EM, Bloembergen N, Pound RV. Resonance Absorption by Nuclear Magnetic Moments in a Single Crystal of Caf<sub>2</sub>. *Physical Review*. 1946;70(11-1):988-988.
3. Bloch F, Hansen WW, Packard M. Nuclear Induction. *Physical Review*. 1946;69(3-4):127-127.
4. Damadian R. Tumor Detection by Nuclear Magnetic Resonance. *Science*. 1971;171(3976):1151-&.
5. Lauterbur P. Image Formation by Induced Local Interactions - Examples Employing Nuclear Magnetic-Resonance. *Nature*. 1973;242(5394):190-191.
6. Bottomley PA, Hart HR, Edelstein WA, et al. Nmr Imaging Spectroscopy System to Study Both Anatomy and Metabolism. *Lancet*. 1983;2(8344):273-274.
7. Klomp DW, Bitz AK, Heerschap A, Scheenen TW. Proton spectroscopic imaging of the human prostate at 7 T. *NMR Biomed*. Jan 23 2009.
8. Kraff O, Bitz AK, Kruszona S, et al. An eight-channel phased array RF coil for spine MR imaging at 7 T. *Invest Radiol*. Nov 2009;44(11):734-740.
9. van Elderen SG, Versluis MJ, Webb AG, et al. Initial results on in vivo human coronary MR angiography at 7 T. *Magn Reson Med*. Dec 2009;62(6):1379-1384.
10. Wu X, Vaughan JT, Ugurbil K, Van de Moortele PF. Parallel excitation in the human brain at 9.4 T counteracting k-space errors with RF pulse design. *Magn Reson Med*. Feb 2010;63(2):524-529.
11. Trattnig S, Pinker K, Ba-Ssalamah A, Nobauer-Huhmann IM. The optimal use of contrast agents at high field MRI. *Eur Radiol*. Jun 2006;16(6):1280-1287.
12. Levitt M. *Spin dynamics, basics of nuclear magnetic resonance*: John Wiley & Sons, Ltd.; 2001.

13. Haacke E, Brown R, Thompson M, Venkatesan R. *Magnetic resonance imaging, physical principles and sequence design*: John Wiley & Sons, Inc.; 1999.
14. Sodickson DK, Manning WJ. Simultaneous acquisition of spatial harmonics (SMASH): fast imaging with radiofrequency coil arrays. *Magn Reson Med*. Oct 1997;38(4):591-603.
15. Pruessmann KP, Weiger M, Scheidegger MB, Boesiger P. SENSE: sensitivity encoding for fast MRI. *Magn Reson Med*. Nov 1999;42(5):952-962.
16. Griswold MA, Jakob PM, Heidemann RM, et al. Generalized autocalibrating partially parallel acquisitions (GRAPPA). *Magn Reson Med*. Jun 2002;47(6):1202-1210.
17. Hoult DI, Chen CN, Sank VJ. The field dependence of NMR imaging. II. Arguments concerning an optimal field strength. *Magn Reson Med*. Oct 1986;3(5):730-746.
18. Carlson JW. Power deposition and noise correlation in NMR samples. *Magn Reson Med*. Jun 1989;10(3):399-403.
19. Roemer PB, Edelstein WA, Hayes CE, Souza SP, Mueller OM. The NMR phased array. *Magn Reson Med*. Nov 1990;16(2):192-225.
20. Hennig J, Nauerth A, Friedburg H. RARE imaging: a fast imaging method for clinical MR. *Magn Reson Med*. Dec 1986;3(6):823-833.
21. International Electrotechnical Commission. Medical electrical equipment - Part 2-33: Particular requirements for the basic safety and essential performance of magnetic resonance equipment for medical diagnosis. *IEC 60601-2-33*. Edition 3.0, 2010
22. Yee K. Numerical solutions of initial boundary value problems involving Maxwell's equations in isotropic media. *IEEE Transactions on antennas and Propagation*. 1966;14:302-307.
23. Oppelt A, ed *Imaging Systems for Medical Diagnostics*: Publicis Corporate Publishing; 2005. Siemens, ed.
24. Chen C, Hoult D. *Biomedical magnetic resonance technology*. Institute of Physics Publishing; 1989.

25. Kerem A, Lehnerdt GF, Gizewski ER, Lang S, Kraff O. Diagnostik der Glandula parotis mittels 7-Tesla-MRT. Paper presented at: 80. Jahresversammlung der Deutschen Gesellschaft für Hals-Nasen-Ohren-Heilkunde, Kopf- und Hals-Chirurgie e.V.2009; Rostock, Germany.
26. Breyer T, Kraff O, Maderwald S, et al. Carotid Plaque Imaging with an Eight-Channel Transmit/Receive RF Array at 7 Tesla: First Results in Patients with Atherosclerosis. Paper presented at: Proceedings Joint Annual Meeting ISMRM-ESMRMB; May, 2010; Stockholm.
27. Grams A, Kraff O, Umutlu L, et al. MRI of the lumbar spine at 7 Tesla in healthy volunteers and a patient with spina bifida. Paper presented at: Proceedings Joint Annual Meeting ISMRM-ESMRMB; May, 2010; Stockholm.

# Chapter 2 High-resolution MRI of the human parotid gland and duct at 7 T \*

## Abstract

MR techniques have been reported as an alternative to conventional sialography. This study aimed to optimize sequences for high-field MR imaging of the parotid gland and duct, as well as the facial nerve at 7 T and show the potential of high field imaging in first in vivo images.

A 10-cm-diameter loop coil was used to optimize various gradient echo (MEDIC, DESS) and spin echo (PD/T2, STIR) sequences to be subsequently tested on four healthy volunteers and four patients. High-resolution images were compared with 1.5 T images both quantitatively (SNR, CNR) and qualitatively (visual rating).

The high 0.6 mm isotropic resolution of the 3D DESS sequence was very useful for defining an oblique orientation with most of the duct being in-plane for subsequent imaging. With the MEDIC sequence, very fine branches of the duct were visible; furthermore, MEDIC yielded a very good depiction of lymph nodes. Severe SAR problems were observed with the STIR sequence at 7 T. Gland tissue in tumor patients can be well characterized with the PD/T2 TSE. Highest CNR between duct and gland was achieved with the 7 T DESS. At 1.5 T, only the STIR sequence showed comparable quality to the overall superiority of the 7 T sequences. The facial nerve could only be depicted close to the skull base.

MR imaging at 7 T provides excellent image contrast and resolution of the parotid gland and duct. The proposed protocol offers a non-invasive examination within about 30 minutes.

\* **Kraff O**, Theysohn JM, Maderwald S, Kokulinsky PC, Dogan Z, Kerem A, Kruszona S, Ladd ME, Gizewski ER, Ladd SC. High-resolution MRI of the human parotid gland and duct at 7 Tesla. *Invest. Radiol.* Sep 2009;44(9):518-524

## 2.1 Introduction

Lesions of the salivary glands can be a suspicious mass, calculi causing obstruction and inflammation, or a diffuse glandular enlargement. Pleomorphic adenomas represent nearly 80% of all benign parotid masses, followed by monomorphic adenomas and myoepitheliomas <sup>1</sup>. Regarding obstructive or inflammatory lesions, sialolithiasis is a very common disease where calculi may occur within the main ducts or within intraglandular ductal tributaries. Sialadenitis may be a direct result from sialolithiasis due to poor outflow of saliva or may represent autoimmune inflammatory conditions. While X-ray sialography has been considered the standard of reference in assessing salivary gland diseases, it has certain drawbacks such as the use of ionizing radiation and invasive cannulation for contrast agent injection through the narrow ducts. Moreover, it is contraindicated in case of acute sialadenitis. In any case, the injection of contrast agents can irritate the duct and can force inflammatory products deep into the gland's parenchyma <sup>2</sup>. Due to its complex anatomy, the parotid gland is a challenging region for surgery. The relative position of abnormalities with respect to intraparotid components (parotid duct, its major tributaries, and facial nerve) must be assessed to avoid potential surgical complications.

MR sialography has been reported as an alternative to conventional sialography <sup>3</sup>. However, MR sialograms, while clearly demonstrating the main duct and primary branching ducts, often fail to demonstrate higher-order branches at clinically established field strengths (1.0 T) <sup>4</sup>. This may be addressed by higher field strengths <sup>5</sup>. High-field systems, especially 3 T, are more and more finding their way into clinical routine. Compared to 1.5 T, imaging at 3 T <sup>6</sup> theoretically improves the signal-to-noise ratio (SNR) by a factor of 2, which allows improving the spatial resolution or reducing the scan time without sacrificing signal- (SNR) and contrast-to-noise (CNR) ratios compared to 1.5 T.

Parotid gland tissue as well as tumors can be well evaluated by MR, including tumor infiltration into surrounding tissue. However, the depiction of the facial nerve, especially its intraparotid course, remains a challenge <sup>7</sup>.

Moving from 1.5 T to 3 T, the sequences and scan protocols require adjustments for optimal image quality<sup>8</sup>. Likewise, sequence parameters which have been optimized for MRI at 3 T or even 1.5 T cannot be transferred to 7 T without major modifications. Specific absorption rate (SAR) limitations, novel image artifacts, e.g. due to increased susceptibility effects, and different tissue relaxation times and contrasts necessitate adjustments of the sequence parameters. To our knowledge, no imaging of the parotid gland at 7 T has yet been reported. Therefore, our study aimed to optimize sequences for high-field MR imaging of the parotid gland, the duct and its tributaries, as well as the facial nerve at 7 T and show the potential of high-field imaging in comparison to 1.5 T MRI in patients.

## 2.2 Materials and Methods

### *Subjects*

Four healthy volunteers (all male, mean age 30.3 years) with no history of salivary gland disease underwent both 1.5 T and 7 T MRI examinations for the sequence optimization process. Subsequently, four patients with clinically diagnosed pathologies, corroborated with ultrasound, were included in this study: one 49-year-old female patient was diagnosed with chronic parotitis, one 28-year-old female had recurrent, unknown swelling of the gland, one 68-year-old female reported with a pleomorphic adenoma, and a 44-year-old male had a cystadenolymphoma. Histology was performed routinely after surgical therapy in the two latter cases. The study was approved by the local institutional review board and all subjects gave written consent prior to the MR examinations at both field strengths.

### *1.5 T examinations*

All 1.5 T examinations were performed on a Magnetom Espree (Siemens Healthcare, Erlangen, Germany) equipped with a gradient coil capable of 33 mT/m gradient strength and 200 mT/m/ms slew rate. A 17-cm-diameter linearly polarized loop coil (Siemens Healthcare, Erlangen, Germany) was used for signal reception and placed laterally against the head to cover the parotid gland. Triangular cushions helped to fixate the subject's head and the coil for the duration of the examination. Images were obtained with manufacturer-provided gradient- (GRE) and spin-echo (SE) sequences, including a fat saturated, T2\*-weighted multi-echo data combination (MEDIC) GRE sequence, a T2-weighted short TI inversion recovery (STIR) turbo spin echo (TSE) sequence, and a double-echo PD- and T2-weighted TSE sequence (Tab. 2.1).

## *7 T examinations*

High-field MR imaging was performed on a 7 T whole-body scanner (Magnetom 7 T, Siemens Healthcare, Erlangen, Germany) equipped with a high performance gradient coil (45 mT/m gradient strength, 200 mT/m/ms slew rate). Due to the absence of a body transmit coil at 7 T, a 10-cm-diameter transmit/receive single loop coil (Rapid Biomedical, Würzburg, Germany) was used for signal excitation and reception. The coil was placed close to the area of interest.

The same sequence types used at 1.5 T were also used at 7 T; only the STIR sequence had to be excluded due to SAR restrictions along with very low contrast and insufficient image quality, probably due to incomplete inversion of the magnetization in regions of  $B_1$  inhomogeneity or strong susceptibility variations. Additionally, a 3D double echo steady-state (DESS) sequence was used at 7 T, as well as a T1-weighted 3D fast low angle shot (FLASH) sequence. The latter was used to image the facial nerve. Within the regulatory and technical limitations, flip angle, repetition and echo time, bandwidth, and number of slices were modified to obtain optimal image contrast (rated visually by a physicist and a senior radiologist), maximum coverage, and the highest spatial resolution within an acquisition time of less than 10 minutes per contrast.

SAR scales approximately with the field strength squared and is the most restricting factor in 7 T MRI. Since T1 relaxation times increase with increasing field strength, this implies longer repetition times to keep SNR and CNR high. However, this also lengthens acquisition time. Therefore, a compromise between SNR, CNR, and examination time had to be made.

All sequences of this protocol were optimized for 7 T in healthy volunteers first and subsequently tested in the four patients. All subjects underwent both 1.5 T and 7 T examinations (protocols see Tab. 2.1) for comparison. Both examinations were performed on the same day. Despite optimization to visualize not only the glandular parenchyma and intraparotid duct but also the facial nerve, the facial nerve could not



be precisely depicted or followed in the healthy volunteer datasets. Hence, the focus of the study was subsequently set to image and analyze the duct and gland only.

	TR [ms]	TE [ms]	slices	alpha [°]	matrix	voxel size [mm <sup>3</sup> ]	BW [Hz/px]	TA [min:sec]
<b>MEDIC 7T</b>	1540	15	39	30	512x512	0.35x0.35x1.5	326	9:53
<b>MEDIC 1.5T</b>	1130	25	39	30	256x256	0.60x0.60x3.0	178	7:15
<b>PD/T2TSE 7T</b>	3500	42/111	12	150	512x512	0.35x0.35x1.5	178	6:06
<b>PD/T2TSE 1.5T</b>	3710	34/101	30	150	256x256	0.70x0.70x3.0	130	3:54
<b>3D-FLASH 7T</b>	7.0	3.1	104	10	320x320	0.60x0.60x0.60	200	4:40
<b>DESS 7T</b>	14.2	5	160	30	256x256	0.60x0.60x0.6	250	5:47
<b>STIR 1.5T</b>	4300	56	20	150	256x256	0.70x0.70x3.0	120	6:11

**Tab. 2.1** – Final sequence parameters. For the 1.5 T STIR sequence, an inversion time of 160 ms was selected. Given is the not interpolated voxel size.

## Image Analysis

Signal-to-noise ratios (SNR) were calculated for duct, gland, and surrounding muscle as well as for lymph nodes in the healthy volunteer data. Additionally, contrast-to-noise ratios ( $CNR = SNR_A - SNR_B$ ) were calculated between duct ( $SNR_A$ ) and surrounding tissue ( $SNR_B$ ). Since diverse pathologies were included, this analysis was not performed in the patient data.

Two senior radiologists were asked to perform a visual evaluation of the overall quality using a five-point scale (from 1 = uninterpretable to 5 = very good) for both the 1.5 T and 7 T images of all eight subjects. The evaluation included delineation of duct and lymph nodes against surrounding tissue, homogeneity of the duct, and depiction of the glandular parenchyma. The mean grades of both readers were used in the subsequent comparisons.

## 2.3 Results

None of the volunteers or patients experienced any clinically relevant side effects, and all eight subjects completed both 1.5 T and 7 T examinations. Tab. 2.1 shows the optimized parameters of all sequences at 7 T and compares them to the parameters used in the 1.5 T protocol. The total examination time of the 7 T protocol is approximately 30 minutes, including 2 to 3 minutes for proper adjustment of frequency, transmitter voltage as well as 3D shim, which had to be performed manually prior to each examination.

### *Protocol Optimization at 7 T*

In order to clearly distinguish between duct and gland with the 3D DESS sequence, repetition time (TR) and echo time (TE) were set to 14.2 ms and 5 ms, respectively. Since SAR is linearly proportional to the radiofrequency bandwidth, it could be reduced significantly (by a factor of 3) using a narrowband pulse for water excitation. This allowed a flip angle  $\alpha$  of  $30^\circ$ . Furthermore, background signal from the muscle was reduced. A high isotropic resolution of  $(0.6 \text{ mm})^3$  proved very useful in finding an adequate oblique orientation for the subsequent sequences with most of the duct being in-plane. Also, as stated in previous investigations at 1.5 T, this 3D steady-state sequence was able to reveal the relationship between the ducts and the intraglandular tumor<sup>9</sup>. Hence, the DESS sequence was acquired at the very beginning of our imaging protocol.

For the 2D MEDIC sequence, a frequency selective fat suppression pulse reduced the fat signal component of the gland, which resulted in an increase of CNR between duct and gland of around 30%. Due to a relatively long TR of 1590 ms and small flip angle  $\alpha = 30^\circ$ , there were less severe SAR problems (compared to TSE, see below) and thus fewer coverage restrictions despite the use of the additional pre-saturation pulse. Aligned according to the best orientation found with the DESS sequence, 39 slices could be acquired with a resolution of  $0.35 \times 0.35 \times 1.5 \text{ mm}^3$ .

Due to the large refocusing flip angle of  $150^\circ$ , SAR was a major issue for the double-echo TSE sequence, limiting the maximum number of slices per acquisition. Hence, the variable-rate selective excitation (VERSE) <sup>10</sup> pulse was selected, which significantly reduced the energy deposition without any noticeable trade-offs in image quality. However, two measurements (12 slices each) were still needed for complete coverage. A turbo factor of 5 was used, and two echoes were read out at TE = 28 ms and 111 ms. The first echo yielded an intermediate PD-weighted contrast with the saliva being hyperintense. Background signal from muscle and glandular tissue was further reduced with the second, heavily T2-weighted echo.

In three out of four healthy volunteers, the facial nerve could presumably be depicted extracranially close to the brain stem with the 0.6 mm isotropic 3D-FLASH sequence at 7 T as a hypointense structure surrounded by hyperintense fatty tissue (see Fig. 2.1). However, the two radiologists were not in all cases convinced that it was indeed the nerve that had been depicted, and even more important, the nerve could not be followed with sufficient confidence into the parotid gland. Within the glandular parenchyma, confusion with vessels is hard to eliminate since both structures, the nerve and some vessels, appear dark in the FLASH. With the other sequences or at 1.5 T, it was either much more difficult or not at all possible to delineate the facial nerve.

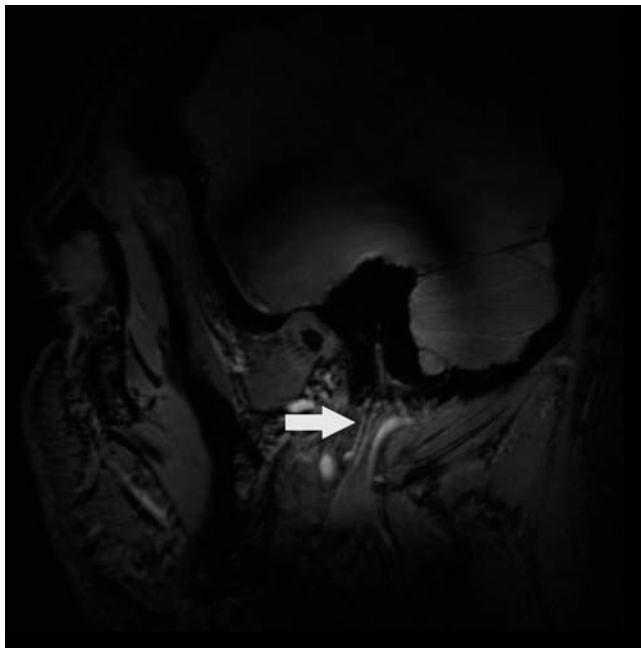


**Fig. 2.1** – Sagittal view of the T1-weighted 3D-FLASH sequence acquired in a healthy volunteer at 7 T. Presumably, the facial nerve is shown as a hypointense trunk surrounded by fatty tissue (arrow).

### *Quantitative Image Analysis*

At 1.5 T, the SNR measurement of the duct was not possible in one out of four healthy volunteers with the MEDIC sequence and in all four volunteers with the PD/T2 TSE sequence. The duct was either too small or could not be identified at all. The 7 T DESS sequence yielded by far the highest SNR of the duct and lymph nodes among all sequences. In a direct comparison between 7 T and 1.5 T, the MEDIC sequence at 7 T showed 3.2 times higher SNR of the duct and 1.9 times higher SNR of the lymph nodes, while 1.5 T STIR yielded the highest SNR of the duct and lymph nodes among all 1.5 T sequences. Comparing the PD/T2 TSE sequence at both field strengths, lower SNR values were found at 7 T for lymph nodes, gland, and muscle. All SNR values are provided in Tab. 2.2.

	<b>SNR duct</b>	<b>SD</b>	<b>SNR LN</b>	<b>SD</b>	<b>SNR gland</b>	<b>SD</b>	<b>SNR muscle</b>	<b>SD</b>
<b>MEDIC 7T</b>	96.4	13.2	67.5	19.7	17.1	6.5	67.3	16.7
<b>MEDIC 1.5T</b>	30.6	7.0	35.6	7.0	17.9	5.7	25.0	6.0
<b>PD TSE 7T</b>	62.0	13.4	55.8	12.7	40.3	8.4	48.4	5.1
<b>PD TSE 1.5T</b>	na	na	65.5	23.3	65.3	5.7	38.1	6.7
<b>T2 TSE 7T</b>	43.0	13.2	20.0	7.4	12.2	1.1	5.2	0.8
<b>T2 TSE 1.5T</b>	na	na	40.7	11.7	36.3	2.2	12.5	1.3
<b>DESS 7T</b>	297.9	90.7	105.7	18.7	42.6	19.6	122.7	12.4
<b>STIR 1.5T</b>	73.6	36.9	74.2	21.5	37.2	14.2	21.5	12.5

**Tab. 2.2** – SNR evaluation. Given are the SNR values of duct, lymph nodes (LN), gland and muscle together with their corresponding standard deviations (SD). The SNR values are not corrected for different voxel sizes, i.e. there is a six- to eight-fold higher resolution at 7 T compared to 1.5 T.

Highest CNR values between duct and gland ( $255.3 \pm 98.2$ ) as well as muscle ( $175.2 \pm 99.2$ ) were achieved with the 7 T DESS sequence, while comparable CNR values between lymph nodes and gland were found in both 7 T DESS ( $63.1 \pm 9.9$ ) and 7 T MEDIC ( $50.4 \pm 15.4$ ). In a direct comparison, the MEDIC yielded 5.4 times higher CNR between duct and gland at 7 T than at 1.5 T. For the CNR between lymph nodes and gland, the ratio was 2.9 times higher at 7 T. Within the 1.5 T protocol, the STIR sequence yielded the highest CNR values. Despite the lower SNR at 7 T for the PD/T2 TSE than at 1.5 T, the CNR between lymph nodes and gland remains the same at both field strengths. Fig. 2.2 shows the results of the complete CNR evaluation.

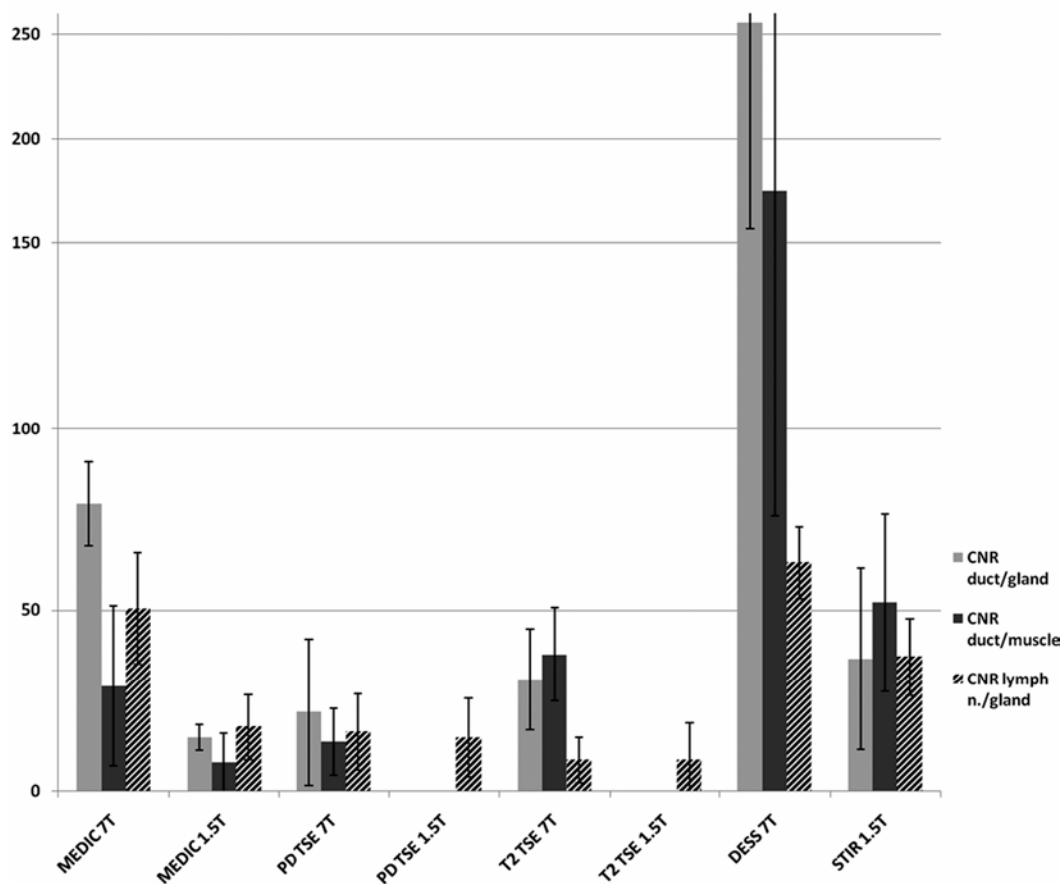


**Fig. 2.2** – Comparison of CNR values calculated between duct and gland, duct and muscle, as well as lymph node and gland.

### Qualitative Image Analysis

The visual assessment of image quality over all eight subjects yielded superiority of the 7 T sequences compared to their 1.5 T counterparts as shown in Tab. 2.3, significantly higher ratings were consistently achieved with the 7 T sequences. Only the 1.5 T STIR sequence showed comparable quality. Regarding delineation of the duct, 7 T MEDIC, 7 T T2 TSE and 7 T DESS were all rated best (4.7), while in the 1.5 T PD and T2 TSE images the duct could hardly be found (1.0 and 1.7, respectively). The same result was found for the homogeneity of the duct (see Fig. 2.3), where 7 T T2 TSE and 7 T DESS yielded the highest score (4.4). In Fig. 2.4, both 1.5 T and 7 T images of a patient with chronic parotitis are presented

for all sequences. The overall quality of the 7 T images is clearly improved if compared to 1.5 T. The higher signal and spatial resolution can also be appreciated in Fig. 2.5, where MEDIC images of a pleomorphic adenoma are shown. A very narrow duct, compressed by the adjacent mass, is visible only at 7 T. Also, the internal tumor structure is better visualized at 7 T. However, due to the compressed duct, a fair evaluation was not possible and the visual rating regarding delineation and homogeneity of the duct could not be performed. The 1.5 T STIR and MEDIC achieved best depiction of glandular parenchyma (3.9), followed by 7 T MEDIC and DESS (3.8).

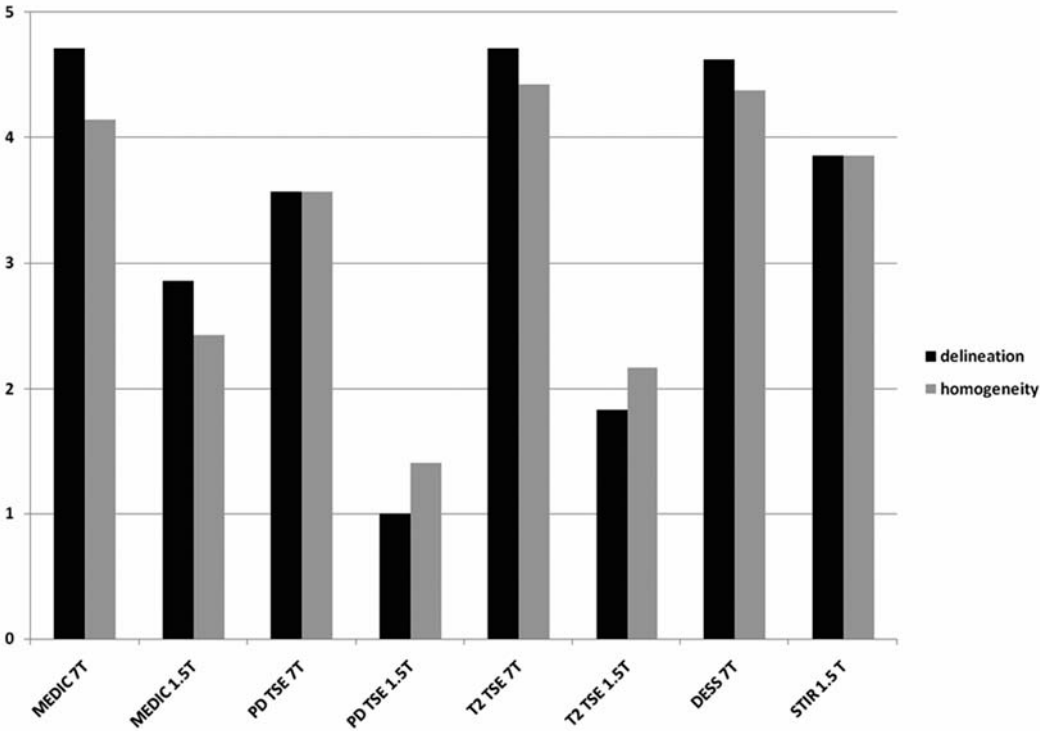


**Fig. 2.3** – Visual evaluation of the delineation and homogeneity of the duct.

The largest discrepancy between the two subject groups, healthy volunteers and patients, was observed with the 7 T T2 TSE sequence in this evaluation. Considered separately, this sequence was rated 1.8 points better in the patient images than in the healthy volunteer images. Lymph nodes were best delineated from background tissue with 7 T MEDIC (4.6), 1.5 T STIR (4.3), and 7 T DESS (4.3).

	Duct			Gland			Lymph Nodes					
	Delineation			Homogeneity			Depiction			Delineation		
	h	p	c	h	p	C	h	p	c	h	p	c
<b>MEDIC 7T</b>	4.5	5.0	4.7	4.0	4.3	4.1	3.8	3.8	3.8	5.0	4.3	4.6
<b>MEDIC 1.5T</b>	2.5	3.3	2.9	2.0	3.0	2.4	3.8	4.0	3.9	3.3	4.0	3.6
<b>PD TSE 7T</b>	4.0	3.0	3.6	4.0	3.0	3.6	3.3	4.0	3.6	3.3	3.8	3.5
<b>PD TSE 1.5T</b>	1.0	1.0	1.0	1.3	1.5	1.4	2.8	3.8	3.3	2.0	1.8	1.9
<b>T2 TSE 7T</b>	5.0	4.3	4.7	4.5	4.3	4.4	2.5	4.3	3.4	2.8	3.0	2.9
<b>T2 TSE 1.5T</b>	1.3	2.3	1.8	1.7	2.7	2.2	3.0	3.5	3.3	2.3	1.8	2.0
<b>DESS 7T</b>	4.8	4.5	4.6	4.3	4.5	4.4	3.5	4.0	3.8	4.3	4.3	4.3
<b>STIR 1.5 T</b>	3.8	4.0	3.9	3.5	4.3	3.9	3.8	4.0	3.9	4.3	4.3	4.3

**Tab. 2.3** – Visual evaluation listed separately for healthy volunteers (h), patients (p), and both groups combined (c). Each value given represents the mean score of both readers.

Superiority of the 7 T MRI compared to 1.5 T is impressively demonstrated in Fig. 2.6 showing fine branches of the intraglandular ductal tributaries up to fourth order in a patient with recurrent swelling of the gland. Dilatation of small ductules is very well rendered by the 7 T image. In Fig. 2.7, corresponding images of a healthy volunteer are also provided for comparison. In the 7 T MEDIC image, lymph nodes can easily be recognized. Furthermore, their fibrous capsule can be delineated from the hilum which is not visible at 1.5 T.



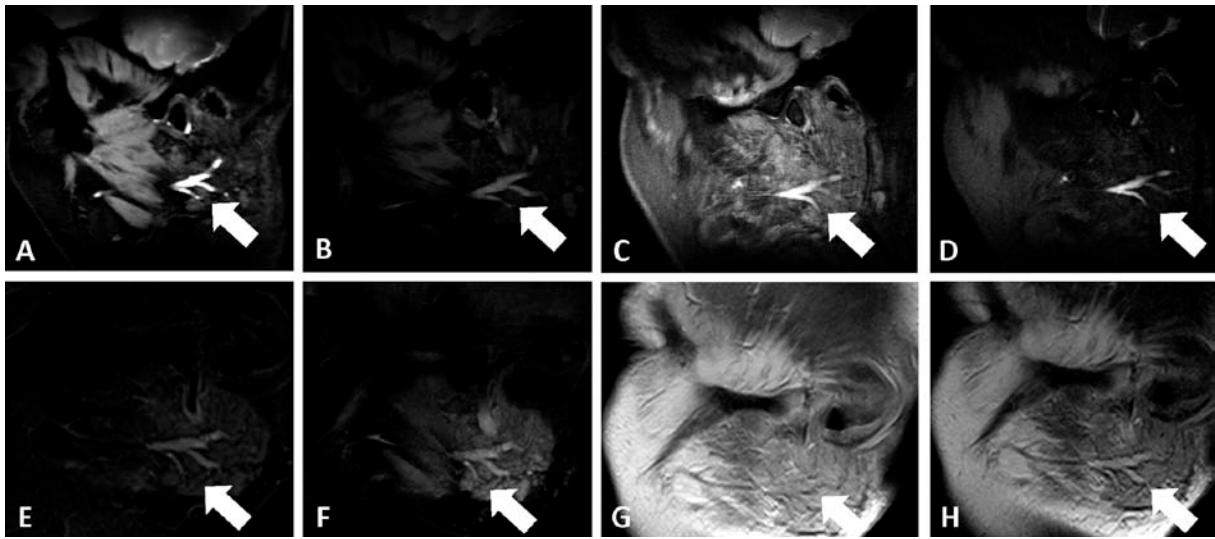


**Fig. 2.4** – Patient with chronic parotitis. Top row shows 7 T images (A: DESS, B: MEDIC, C: PD TSE, D: T2 TSE), which can be compared to the 1.5 T images below (E: STIR, F: MEDIC, G: PD TSE, H: T2 TSE). The arrow marks the enlarged duct. CNR between duct and surrounding tissue is higher at 7 T than at 1.5 T for all contrasts.

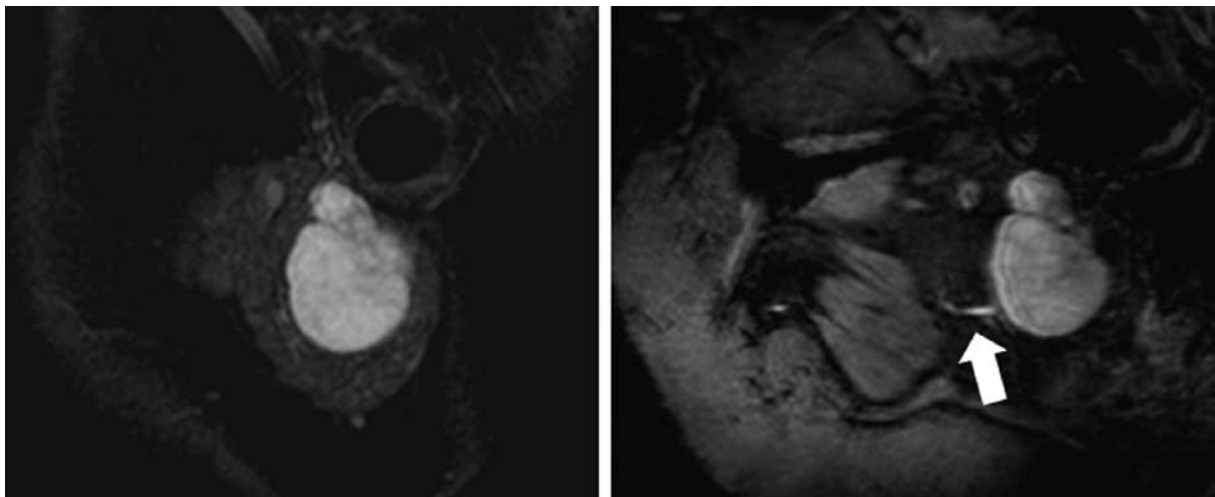


**Fig. 2.5** – Patient with a pleomorphic adenoma. Left side shows the 1.5 T MEDIC image in comparison to the 7 T MEDIC image (right). At 7 T the compressed duct is slightly visible (arrow).

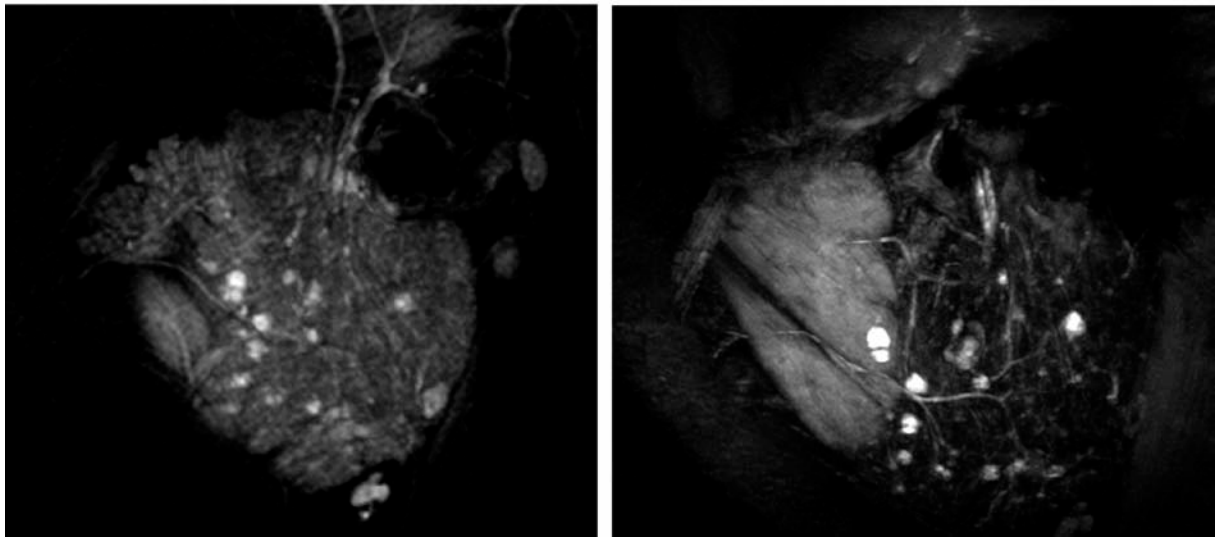


**Fig. 2.6** – MEDIC MIP images at 1.5 T (left) and 7 T (right) from a patient with recurrent gland swelling, which may be compared to corresponding images of a healthy volunteer in Fig. 2.7.

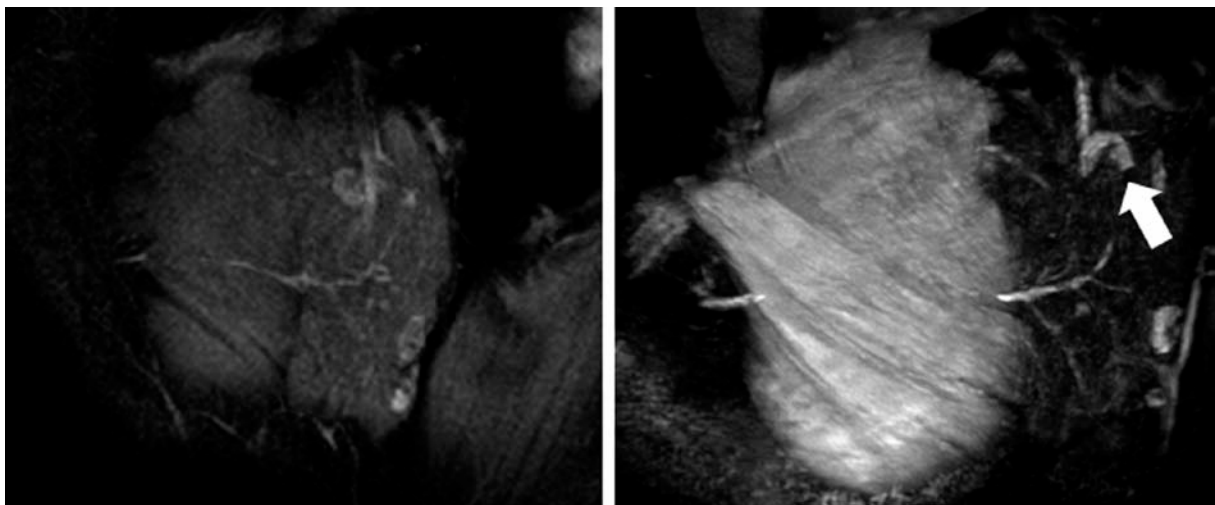


**Fig. 2.7** – MEDIC MIP images at 1.5 T (left) and 7 T (right) from a healthy volunteer. At 7 T, please note the good depiction of the lymph nodes in contrast to the surrounding glandular parenchyma as well as the details of the internal structure and capsule of the lymph nodes themselves (arrow).

## 2.4 Discussion

These initial results demonstrate that high-resolution 7 T MRI of the parotid gland is a promising technique. Although positioning and fixation of the coil is certainly improvable, the examination was well tolerated by all subjects. MR imaging at 7 T provides excellent image contrast and resolution of the parotid gland and duct. While the MEDIC and DESS are advantageous for displaying the duct and branches (rated best in both the qualitative and quantitative evaluation), the gland tissue in tumor patients can be better characterized with the PD/T2 TSE. This was highlighted by the enormous difference between healthy volunteers and patients (1.8 points difference) in the visual evaluation.

Despite the considerable increase in spatial resolution, the comparison of SNR values between field strengths (Tab. 2.2) showed that the GRE sequences still seem to have potential for even smaller voxels at 7 T. However, the TSE sequence yielded only comparable or even less SNR at 7 T compared to 1.5 T. This can be partially explained by the eight-fold higher resolution at 7 T, whereas the increase in field strength provides only a theoretical SNR increase of 4.7 assuming equivalent RF coils. The known  $B_1$  inhomogeneities at 7 T and limited penetration depth due to the smaller coil diameter (which actually favors higher SNR), resulting in an inefficient and inhomogeneous refocusing pulse, have to be considered as factors further reducing SNR. Hence, the combination of long echo times and strong flip angle variation may explain the difference in SNR between GRE and TSE sequences at 7 T.

MEDIC and especially DESS, which allows a high-resolution 3D tracing of the entire duct and which was found to be very useful for the planning of the 2D sequences, form the foundation of the proposed 7 T protocol. The PD/T2 TSE sequence may be included in case of tumor patients or other lesions of the glandular parenchyma. Additional intravenous contrast agent administration for better differentiating between different tumor types <sup>11</sup> is presumably also possible at 7 T <sup>12</sup>.

The facial nerve could presumably be depicted at the base of the skull similar to a publication from L. Jäger and M. Reiser <sup>13</sup>, but in general the results of former publications <sup>7,13-14</sup> could not be reproduced. The difficulty in depicting the intraglandular nerve might also explain why no study could be found by us which can provide an 'all-in-one' protocol for comprehensively diagnosing the parotid gland with all its components. At 7 T, fast imaging with steady state precession, as implemented in a TrueFISP or CISS sequence, which has been recommended in 1.5 T studies of the facial nerve <sup>7,13-14</sup>, suffers from SAR limitations and is inherently prone to strong susceptibility artifacts at 7 T, especially in close proximity to the bony skull base and air-filled areas. Therefore, the focus of the present study concentrated on sequences which show the duct and parenchyma in great detail.

The diagnosis of sialolithiasis is based on signal voids and prestenotic dilatation in MR images <sup>4</sup>, whereas very small, non-obstructing duct stones, which may also cause clinical symptoms, might be missed at clinical field strengths. High-field systems, with their higher ductal signal homogeneity together with the potential increase in spatial resolution and higher sensitivity to susceptibility changes, may address this issue by detecting smaller stones. Although 7 T MRI is still a rare and expensive technique, it might in the future serve as an option for well selected cases, i.e. those needing a very high spatial resolution and/or improved contrast, or those with prior, inconclusive standard imaging (differential diagnosis of sialolithiasis). Additionally, the increase in spatial resolution and good visualization of small tributaries may help in the more accurate diagnosis of sialectasia.

Other techniques can be considered as alternatives: computer tomography (CT), however, is limited in the imaging of inflammatory diseases due to low duct visibility and low soft tissue contrast <sup>15</sup>; ultrasound, on the other hand, offers a widely-available, often-used and rather cheap alternative compared to MRI. Although it is capable of detecting stones, it is less well suited for evaluating the precise extent and location of a lesion. Furthermore, a recent study at 1.5 T suggested MR sialography following prediagnostic ultrasonography as a suitable approach in the diagnosis of salivary duct disorders <sup>16</sup>. Lymph nodes are very well visualized at 7 T, and the

presence of adjacent lymph nodes or intraglandular lymph nodes may suggest the inflammatory nature of a lesion<sup>2</sup>. However, the detectability of adjacent extraglandular lymph nodes depends on the coil size, or more specifically on the available field of view. Using a 10-cm-diameter single loop coil not only confines the available field of view on the side with the pathology, but also does not allow a comparison with the contralateral, presumably healthy side.

Other limitations of the presented study are that the number of subjects was limited and that the included patients had a variety of pathologies. Unfortunately, no patient with an obstructing duct stone could be acquired for this study. However, we believe that our initial results are the basis for a more systematic analysis in patients.

Of course, potential risks and side effects of high-field MRI for patients and medical/service personnel should be taken into account<sup>17</sup>, as commercially available 7 T systems are not certified as medical devices for human use<sup>18-19</sup>. Over the last two years, the number of clinically-oriented studies at 7 T has increased dramatically, driven by emerging RF coil developments, and include potential 7 T applications not only for brain diseases<sup>20-21</sup> but also in other human body regions such as the knee<sup>22-23</sup>, prostate<sup>24</sup>, or even heart<sup>25-26</sup>.

High magnetic fields have been reported to induce several transient physiologic effects (e.g. vertigo, nausea, light flashes). Nevertheless, a recent study on more than 100 subjects exposed to both 1.5 T and 7 T MRI of head, breast, and extremities found a very high acceptance of 7 T MRI. Vertigo during table movement at 7 T, by far the most disturbing phenomenon associated with the magnetic field, was rated less disturbing than some external factors such as acoustic noise and exam duration<sup>27</sup>. Although there is an outstanding need to collect more patient questionnaire data and to systematically investigate these magnetic-field-related phenomena, 7 T MRI appears to be quite tolerable for a clinical diagnostic examination.

In conclusion, the proposed protocol offers a non-invasive examination within about 20-30 minutes and may in the future present a reliable alternative to standard

X-ray sialography and a highly valuable addition to first-line ultrasonography in dedicated or unclear cases (due to high costs). Of course, further studies are needed to discuss the clinical impact of this technique in the assessment of patients with various salivary gland diseases. New sequences and dedicated multi-channel coils allowing parallel acquisition techniques will definitely further improve image quality as well as ameliorate current technical limitations such as SAR and restricted coverage.

## References

1. Freling NJ, Molenaar WM, Vermey A, et al. Malignant parotid tumors: clinical use of MR imaging and histologic correlation. *Radiology* 1992;185(3):691-696.
2. Yousem DM, Kraut MA, Chalian AA. Major salivary gland imaging. *Radiology* 2000;216(1):19-29.
3. Tonami H, Higashi K, Matoba M, Yokota H, Yamamoto I, Sugai S. A comparative study between MR sialography and salivary gland scintigraphy in the diagnosis of Sjogren syndrome. *Journal of computer assisted tomography* 2001;25(2):262-268.
4. Kalinowski M, Heverhagen JT, Rehberg E, Klose KJ, Wagner HJ. Comparative study of MR sialography and digital subtraction sialography for benign salivary gland disorders. *Ajnr* 2002;23(9):1485-1492.
5. Browne RF, Golding SJ, Watt-Smith SR. The role of MRI in facial swelling due to presumed salivary gland disease. *The British journal of radiology* 2001;74(878):127-133.
6. Habermann CR, Gossrau P, Kooijman H, et al. Monitoring of gustatory stimulation of salivary glands by diffusion-weighted MR imaging: comparison of 1.5T and 3T. *Ajnr* 2007;28(8):1547-1551.
7. Takahashi N, Okamoto K, Ohkubo M, Kawana M. High-resolution magnetic resonance of the extracranial facial nerve and parotid duct: demonstration of the branches of the intraparotid facial nerve and its relation to parotid tumours by MRI with a surface coil. *Clinical radiology* 2005;60(3):349-354.
8. Bernstein MA, Huston J, 3rd, Ward HA. Imaging artifacts at 3.0T. *J Magn Reson Imaging* 2006;24(4):735-746.
9. Sumi M, Van Cauteren M, Takagi Y, Nakamura T. Balanced turbo field-echo sequence for MRI of parotid gland diseases. *Ajr* 2007;188(1):228-232.
10. Hargreaves BA, Cunningham CH, Nishimura DG, Conolly SM. Variable-rate selective excitation for rapid MRI sequences. *Magn Reson Med* 2004;52(3):590-597.
11. Alibek S, Zenk J, Bozzato A, et al. The value of dynamic MRI studies in parotid tumors. *Academic radiology* 2007;14(6):701-710.

12. Noebauer-Huhmann I, Kraff O, Juras V, et al. MR Contrast Media at 7Tesla - Preliminary Study on Relaxivities. 2008 April; Toronto. p 1457.
13. Jager L, Reiser M. CT and MR imaging of the normal and pathologic conditions of the facial nerve. *European journal of radiology* 2001;40(2):133-146.
14. Dailiana T, Chakeres D, Schmalbrock P, Williams P, Aletras A. High-resolution MR of the intraparotid facial nerve and parotid duct. *Ajnr* 1997;18(1):165-172.
15. Golding S. Computed tomography in the diagnosis of parotid gland tumours. *The British journal of radiology* 1982;55(651):182-188.
16. Capaccio P, Cuccarini V, Ottaviani F, et al. Comparative ultrasonographic, magnetic resonance sialographic, and videoendoscopic assessment of salivary duct disorders. *The Annals of otology, rhinology, and laryngology* 2008;117(4):245-252.
17. Kangarlu A, Baudendistel KT, Heverhagen JT, Knopp MV. [Clinical high- and ultrahigh-field MR and its interaction with biological systems]. *Der Radiologe* 2004;44(1):19-30.
18. International Electrotechnical Commission. Medical electrical equipment - Part 2-33: Particular requirements for the safety of magnetic resonance diagnostic devices. IEC 60601-2-33; 2002.
19. United States Food and Drug Administration. Guidance for industry and FDA staff: criteria for significant risk investigations of magnetic resonance diagnostic devices. 2003.
20. Kollia K, Maderwald S, Putzki N, et al. First clinical study on ultra-high-field MR imaging in patients with multiple sclerosis: comparison of 1.5T and 7T. *Ajnr* 2009;30(4):699-702.
21. Heverhagen JT, Bourekas E, Sammet S, Knopp MV, Schmalbrock P. Time-of-flight magnetic resonance angiography at 7 Tesla. *Investigative radiology* 2008;43(8):568-573.
22. Welsch GH, Mamisch TC, Hughes T, et al. In vivo biochemical 7.0 Tesla magnetic resonance: preliminary results of dGEMRIC, zonal T2, and T2\* mapping of articular cartilage. *Investigative radiology* 2008;43(9):619-626.



23. Kraff O, Theysohn JM, Maderwald S, et al. MRI of the knee at 7.0 Tesla. *Rofo* 2007;179(12):1231-1235.
24. Metzger GJ, Snyder C, Akgun C, Vaughan T, Ugurbil K, Van de Moortele PF. Local B1+ shimming for prostate imaging with transceiver arrays at 7T based on subject-dependent transmit phase measurements. *Magn Reson Med* 2008;59(2):396-409.
25. Snyder CJ, Delabarre L, Metzger GJ, et al. Initial results of cardiac imaging at 7 tesla. *Magn Reson Med* 2008.
26. van Elderen SG, Versluis MJ, Webb AG, et al. Initial results on in vivo human coronary MR angiography at 7 T. *Magn Reson Med* 2009;62(6):1379-1384.
27. Theysohn JM, Maderwald S, Kraff O, Moenninghoff C, Ladd ME, Ladd SC. Subjective acceptance of 7 Tesla MRI for human imaging. *Magma* 2008;21(1-2):63-72.

## Chapter 3    An eight-channel phased array RF coil for spine MR imaging at 7 T \*

### Abstract

A novel transmit/receive radiofrequency (RF) array for MRI of the human spine at 7 T has been developed. The prototype is characterized in simulations and bench measurements, and the feasibility of high-resolution spinal cord imaging at 7 T is demonstrated in in-vivo images of volunteers.

The RF phased array consists of eight overlapping surface loop coils with a dimension of 12 x 12 cm each. Bench measurements were obtained with a phantom made of body-simulating liquid and assessed with a network analyzer. For safety validation, numerical computations of the RF field distribution and the corresponding specific absorption rate (SAR) were performed based on three different human body models. In vivo images of three volunteers (two with a documented scoliosis) were acquired.

The presented RF coil could be easily integrated into the patient table for examinations of the cervicothoracic or thoracolumbosacral spine. Measurements of the g-factor indicated good image quality for parallel imaging acceleration factors up to 2.7 along the head-foot direction, which could be validated in the in vivo images. The in vivo images demonstrated very fine anatomical features such as the longitudinal ligaments or the venous drainage through the vertebral bodies. A largely homogeneous excitation over an extensive field-of-view of 40 cm could be obtained.

These early results indicate that a multichannel transmit/receive phased array RF coil can be used for in vivo spine imaging at 7 T, thereby rendering high-resolution spine imaging a promising new application in 7 T clinical research.

\* **Kraff O**, Bitz AK, Kruszona S, Orzada S, Schaefer LC, Theysohn JM, Maderwald S, Ladd ME, Quick HH. An eight-channel phased array RF coil for spine MR imaging at 7 T. Invest Radiol. Nov 2009;44(11):734-740.

### 3.1 Introduction

Magnetic resonance imaging (MRI) at high field strength (3 T and above) is currently establishing itself as a clinical standard for imaging the brain, spine, chest, abdomen, pelvis, vasculature, and extremities <sup>1</sup>. Recent studies have shown that MRI of the spine at 3 T provides many improvements over 1.5 T spine MRI, especially in delineation of soft tissue, cerebrospinal fluid (CSF), and disc and bone interfaces <sup>2</sup>. It has also been shown that the magnetic field strength, specifically 3 T compared to 1.5 T, has an influence on the classification of patients with clinically isolated syndrome (CIS) suggestive for multiple sclerosis (MS) <sup>3</sup>, although it has not yet led to earlier diagnosis <sup>4</sup>. Since 3T spinal cord imaging in patients with CIS and MS improves the diagnostic accuracy <sup>5</sup>, MR imaging of the spine at ultra-high field (UHF) strengths, i.e. 7 T and above, may be able to address the issue of earlier diagnosis <sup>6</sup>. Provided that the theoretical 2.3-fold gain in signal-to-noise (SNR) from 3 T to 7 T can be clinically attained, this potentially allows improving the spatial resolution or reducing the scan time without sacrificing signal or contrast-to-noise (CNR) ratios compared to 3 T. Furthermore, the altered soft tissue contrast at 7 T may improve the delineation of gray and white matter in the internal spinal cord. Although it is still challenging to generate clinically useful contrasts at UHF, within the last few years several publications have shown that 7 T MRI renders an exquisite T2\* contrast for demonstrating the venous microvasculature <sup>7</sup> and that it is advantageous in visualizing detailed structural anatomy and abnormalities of MS lesions <sup>8</sup> in the brain. In addition, the prediction that T1 contrast would collapse at higher field strengths due to the convergence of T1 relaxation times has been contradicted by recent in vivo experimental evidence <sup>9</sup>. However, imaging outside the head at 7 T such as in the spine is still in its infancy, and there is a strong need to develop dedicated coils <sup>10</sup>.

Due to the improved sensitivity performance and concomitant high SNR of radiofrequency (RF) surface coils compared to volume RF coils <sup>11</sup>, the phased array RF coil approach for signal reception has been successfully established for 1.5 and 3 T imaging <sup>12-13</sup>. Especially the depiction of the spine with the target anatomy lying

directly below the surface is predestined for the use of multi-channel surface RF arrays.

A potential limitation when moving to higher field strengths, however, is that the RF excitation wavelength is inversely proportional to the field strength used. Thus, effects of electromagnetic wave propagation in tissue leading to destructive interferences and asymmetric distributions of the excitation radiofrequency magnetic ( $B_1^+$ ) field over the imaging sample are already prominent at 3 T. These effects and their associated signal inhomogeneities increase even further when moving to 7 T MRI<sup>14</sup>, rendering large field-of-view (FOV) applications in high field MRI difficult. Thus, recent hardware and software advances have been introduced to produce a homogeneous RF excitation and/or to reduce the specific absorption rate (SAR) for whole-body imaging at 7 T. These techniques are based on multi-channel RF transmit arrays. By optimizing the phase and amplitude of each independent transmit array element, a technique commonly called RF shimming<sup>15-16</sup>, a more homogeneous  $B_1$  field can be achieved in diverse subjects at ultra-high fields<sup>17-18</sup>. It has also been shown that with transmit SENSE<sup>19</sup>, i.e. the simultaneous application of specially-tailored RF and gradient pulses, a uniform, accelerated, slice-selective excitation can be implemented<sup>20</sup>.

In this work we describe a combined transmit/receive RF array, made of eight overlapping loop coils, for imaging the human spine at 7 T. We characterize this prototype in simulations and bench measurements as well as in phantom and in vivo measurements on volunteers for SNR, g-factor, and high-resolution imaging.

## 3.2 Materials and Methods

### *RF Coil Design and Construction*

The spine array was developed for a 7 T whole-body MR scanner (Magnetom 7 T, Siemens Healthcare Sector, Erlangen, Germany) featuring a 60 cm bore. Eight square surface loop coils with a dimension of 12 x 12 cm were machined from FR4 circuit board material (LPKF Laser & Electronics AG, Garbsen, Germany).

Each coil element is 0.8 mm thick and has 1-cm-wide circuits with a copper-clad layer of 35  $\mu\text{m}$  thickness. Three 2 mm gaps in each loop were bridged by 2.7 and 4.7 pF non-magnetic capacitors (Voltronics Corporation, Denville, NJ, USA). Common-mode cable current suppression was provided by a cable trap located directly at each coil element, formed by a 7 cm long semi-rigid coaxial cable wound in two turns in parallel with and a variable capacitor (2.5-10 pF). The cable trap was tuned to approximately 297 MHz. The coil elements were matched to a 50  $\Omega$  flexible coaxial cable (RG58, Huber+Suhner GmbH, Taufkirchen, Germany). In Fig. 3.1, a schematic of the coil design is given.

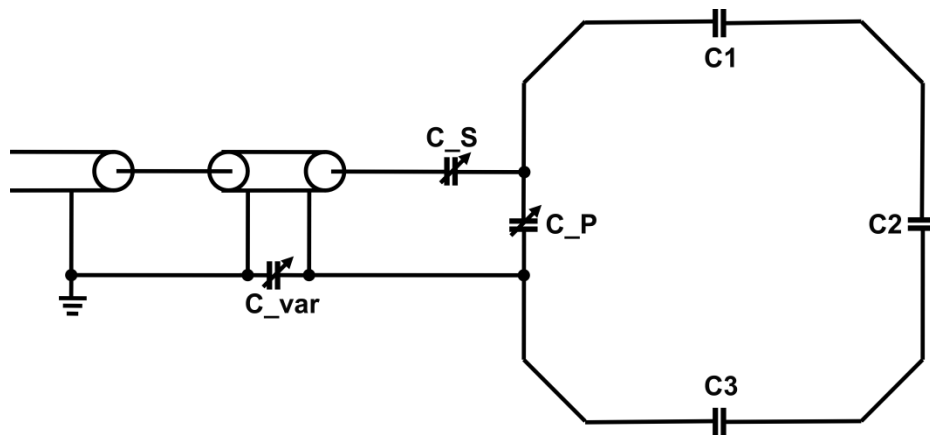


**Fig. 3.1:** Circuit schematic of a coil element and cable trap for common-mode rejection.  $C_{var}$ ,  $C_S$  and  $C_P$  are variable capacitors in the range of 1 pF to 13 pF.  $C_1$ ,  $C_2$  and  $C_3$  are 4.7, 2.7, and 4.7 pF capacitors, respectively.

All neighboring coil pairs were overlapped to reduce the mutual inductance<sup>11</sup>. Furthermore, finite-difference-time-domain (FDTD) simulations<sup>21</sup> of the field distribution indicated use of a shifted and overlapped arrangement of the coil elements as given in Fig. 3.2, which significantly improved the isolation between neighboring as well as next-nearest-neighbor coils approximately by an additional -7 dB compared to the non-shifted design. For the simulations, a rectangular box (35 cm x 22 cm x 15 cm) with homogeneous tissue properties of  $\epsilon_r = 43$  and  $\sigma = 0.8 \text{ S}\cdot\text{m}^{-1}$  was used.

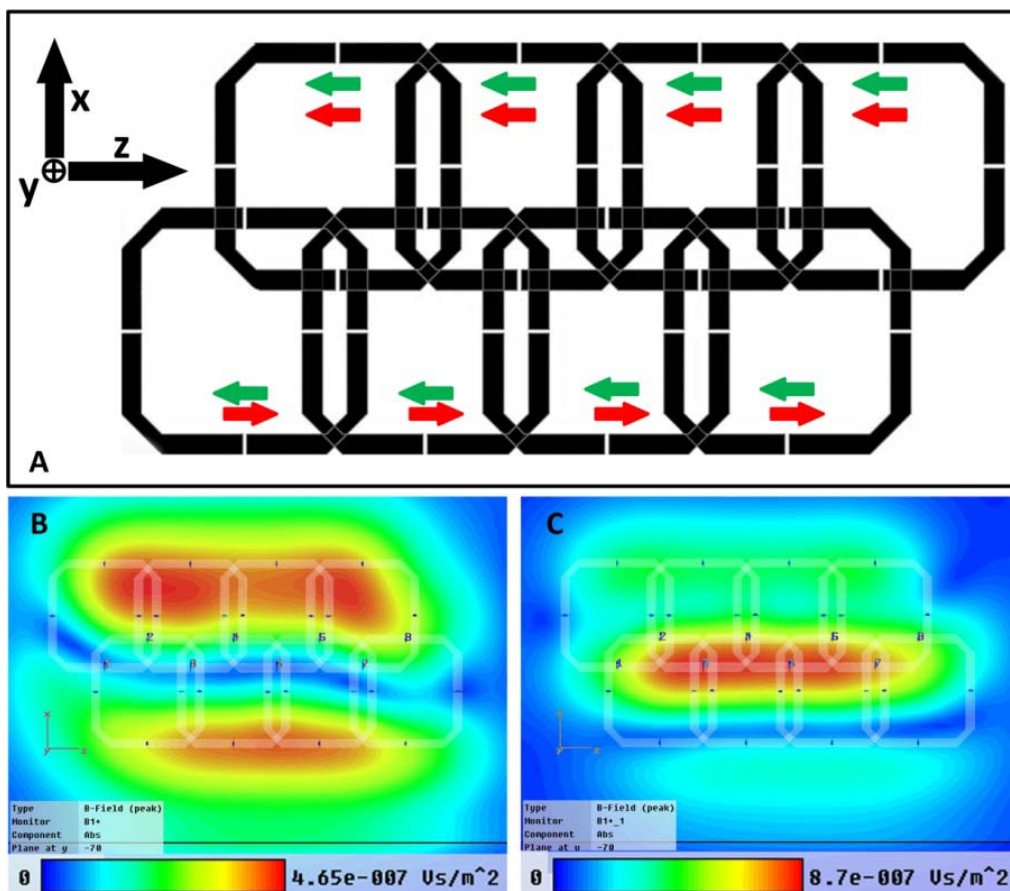


**Fig. 3.2:** Arrangement of the coil elements (top, A). The conductor gaps are 2 mm wide and the corners are chamfered by 45°. Simulations yielded an improved  $B_1^+$  distribution in the region along the center of the array when a 180° phase shift between the upper and lower rows of coil elements was applied, i.e. the currents of all coil elements flow in the negative z direction from the feed points and then in the positive z direction along the center line. The arrows in the top image show the direction of the currents at the outer feed points for the two cases (B: without phase shift / red arrows, C: with phase shift / green arrows).

In Fig. 3.3 an image of the assembled spine array is shown. T/R switches and preamplifiers (Stark Contrast, Erlangen, Germany) are positioned behind the coil at the very end of the patient table and permit connection to eight individual Tx/Rx paths for future RF shimming or Transmit SENSE applications. The switches and amplifiers are not directly integrated with the individual coil elements to allow use for other coil developments, which reduces overall costs. As shown on the right-hand side in Fig. 3.3, the coil can be easily integrated into the patient table for examinations of the cervicothoracic or thoracolumbosacral spine.

The same cable length of 70 cm was used for all eight elements, which were fed with opposite polarity between the two coil rows to provide a  $180^\circ$  phase shift. Hence, currents of both rows point in the positive z direction along the centerline loop paths (see Fig. 3.2). In the FDTD simulations for design optimization, this  $180^\circ$  phase shift increased the  $B_1^+$  amplitude along the centerline of the coil, i.e. in the region of the spine, but created a signal cancellation off-center and parallel to the centerline outside the anatomy of interest.

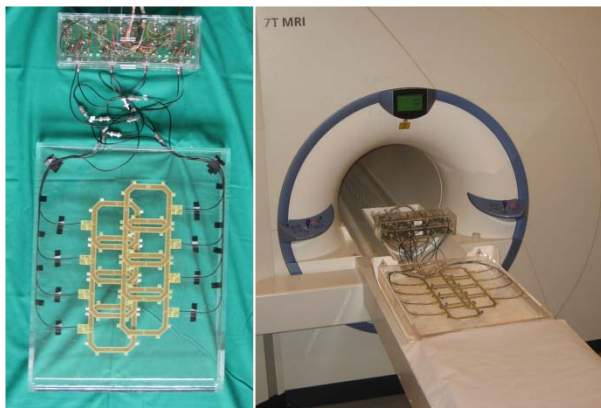


**Fig. 3.3:** Image of the assembled spine array connected to a box with eight pre-amplifiers and T/R switches which can be connected to eight individual Tx/Rx paths (left). Right: spine array coil placed on the patient table.

The elements were matched to 50 Ohms at 297 MHz. Tuning and matching was optimized on the bench with a rectangular phantom (35 cm x 22 cm x 15 cm) filled with body simulating liquid ( $\epsilon_r = 43$ ,  $\sigma = 0.8 \text{ Sm}^{-1}$ ) and assessed with a network analyzer (Agilent E5061A, Santa Clara, CA, USA). S-parameters were determined in the loaded condition and compared for both a phantom and patient load. Additionally, loaded and unloaded Q values were obtained with this set-up.

To acquire data for g-factor maps, MR images of the rectangular phantom were obtained using a FLASH-3D sequence with TR/TE = 3.6/1.76 ms, 10° flip angle, 1 mm<sup>3</sup> resolution, and matrix 512 x 512. Estimates of the g-factor were made with the difference method <sup>22</sup>, which required the acquisition of four images: two with GRAPPA <sup>23</sup> acceleration R (giving SNR<sup>accel.</sup>) and two without acceleration (giving SNR<sup>full</sup>). The difference of each pair of images was used to estimate the standard deviation of the noise. The g-factor maps were calculated pixelwise by the following equation:  $g\text{-factor} = \text{SNR}^{\text{full}} / (\text{SNR}^{\text{accel.}} * \sqrt{R})$ . For the accelerated images, effective GRAPPA acceleration factors of R = 1.9, 2.7 and 3.5 (using 24 reference lines <sup>24</sup>) were chosen.

### *FDTD simulations*

For safety validation, numerical computations <sup>25</sup> of the RF field distribution and the corresponding SAR were performed based on the “Hugo” dataset <sup>26</sup> (male with approximately 1.85 m height and 95 kg weight, 33 different tissue types) as well as on two members of the Virtual Family <sup>27</sup> (“Duke”, 70 kg male, 1.74 m, and “Ella”, 58 kg female, 1.6 m; both of these datasets include more than 80 different tissue types). SAR computations were performed for two regions of interest, i.e. for the cervical spine as well as for the lumbar spine. The array was modeled with the exact physical dimensions including a 1 cm thick plate of acrylic glass which was used for housing the coil. The coil elements were located 1.5 cm (1 cm housing plus 0.5 cm thick neoprene matting) from the back surface of the human body models. The tissue resolution was 2 mm for each model. In all simulations, the elements were excited individually with 1 W peak power and were subsequently vectorially combined. The calculations were done in free space over approximately 7 million grid points.

To validate the numerical model of the array, S parameters were compared between simulation and bench measurements as well as B<sub>1</sub><sup>+</sup> maps between simulation and MR measurement. Later utilized the actual flip angle imaging (AFI) sequence <sup>28</sup> with



the following parameters TR1 = 20 ms, TR2 = 100 ms, nominal flip angle of 60°, 250  $\mu$ s square pulse.

### *In vivo studies*

In vivo studies were performed with signed consent and were approved by the institutional review board. Three volunteers were included: a 31 year-old male (90 kg, 1.86 m), a 29 year-old female (57 kg, 1.62 m), and a 30 year-old male (75 kg, 1.90 m). For the latter two volunteers, a scoliosis had been previously documented. Images were assessed with a FLASH-3D sequence with the following parameters: TR/TE = 20/3.06 ms, 30° flip angle, resolution 0.57 mm isotropic, matrix 704 x 704 x 144, SPAIR fat suppression, and parallel imaging with a GRAPPA<sup>23</sup> acceleration factor 1.9.

### 3.3 Results

S-parameter measurements on the bench yielded an S11 match of the loaded coil between -21 dB and -30 dB for the phantom load for all coil elements. S12 coupling between elements was measured with the loaded coil by transmitting with the network analyzer through one coil element while receiving through another. S12 was found to be in the range of -23 dB to -36 dB for the phantom load. For the case with patient load, the measurements revealed higher reflection and coupling of the coil elements, i.e.  $-13 \text{ dB} > S_{11} > -19 \text{ dB}$  and  $-16 > S_{12} > -27 \text{ dB}$ , respectively. Since the S-parameters differed only at the first decimal between S12 and S21, only half of the scattering matrix is provided in Tab. 3.1 for reasons of clarity.

	S1	S2	S3	S4	S5	S6	S7	S8
S1	-23/-13							
S2	-30/-19	-30/-18						
S3	-23/-16	-23/-16	-21/-19					
S4	-36/-24	-18/-13	-34/-27	-24/-15				
S5	-27/-23	-31/-24	-22/-17	-23/-19	-22/-17			
S6	-21/-18	-27/-20	-27/-22	-18/-14	-36/-26	-27/-19		
S7	-35/-44	-51/-33	-29/-24	-33/-26	-24/-23	-23/-20	-21/-17	
S8	-30/-25	-34/-27	-20/-18	-25/-22	-31/-26	-19/-18	-33/-16	-25/-19

**Tab. 3.1:** S-parameter measurements obtained under two conditions: coil loaded with phantom (left values) and coil loaded with cervicothoracic spine of a volunteer (right values). The values are given in dB.

The unloaded to loaded Q ratio was measured under two conditions. First, the coil with fixed tuning and matching was used, yielding an unloaded to loaded Q ratio of 1.4 for a single element in the presence of all other elements and 2.4 for a single element alone. Second, a single element of the array was used and retuned to 297 MHz for the unloaded case, so that the unloaded to loaded Q ratio, here 6.5, gives a better insight into conductive losses of the coil alone <sup>29</sup>.

Maximum g-factors were 1.35, 1.48, and 1.94 for GRAPPA acceleration factors  $R = 1.9, 2.7,$  and  $3.5$  in the head-feet direction, and  $g = 1.71, 2.32,$  and  $5.64$  for  $R = 1.9, 2.7,$  and  $3.5$  in the right-left direction. In Fig. 3.4, all g-maps are provided for comparison.

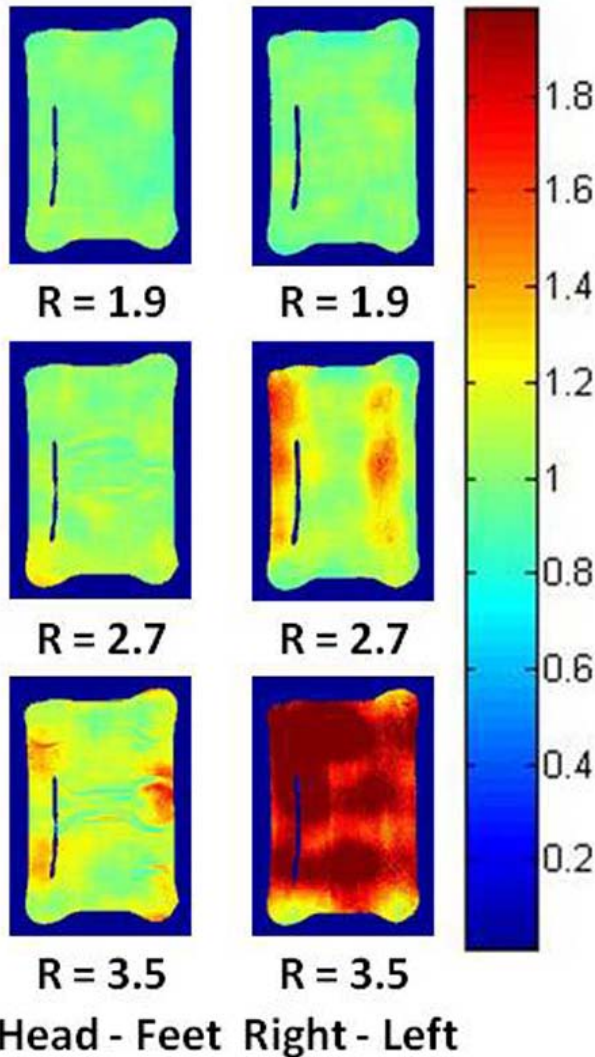


**Fig. 3.4:** G-maps for different GRAPPA acceleration factors applied with phase encoding along head-feet (left) and right-left direction (right), respectively.

In the numerical simulations, similar S-parameters were found compared to the bench measurements. In Fig. 3.5 a comparison between the measured and the simulated  $B_1^+$  distribution of a coronal plane approximately 2 cm inside the phantom is given. In both cases, a similar  $B_1^+$  distribution was found and the maximum  $B_1^+$  values varied by less than 7% (22  $\mu\text{T}$  found in the measurement and 20.7  $\mu\text{T}$  found in the simulation). The maximum permitted input power levels for the lumbar and cervical spine regions are provided in Tab. 3.2 for compliance with the IEC guidelines<sup>30</sup> of 10 W/kg for 10g-averaged local SAR. For the lumbar spine, almost the same maximum permitted power levels were found for the Hugo and Ella datasets, whereas the Duke dataset rendered a 15% lower level. Qualitatively, similar distributions of the deposited power were found for all three datasets as shown in Fig. 3.6. On the other hand, for the calculations in the cervical spine, very similar values were found for the Duke and Ella datasets, but a large discrepancy of 33% was found for the Hugo dataset. For the in vivo examinations, the maximum permitted power levels were set to 12 W for imaging the lumbar spine and to 9 W for imaging the cervical spine.

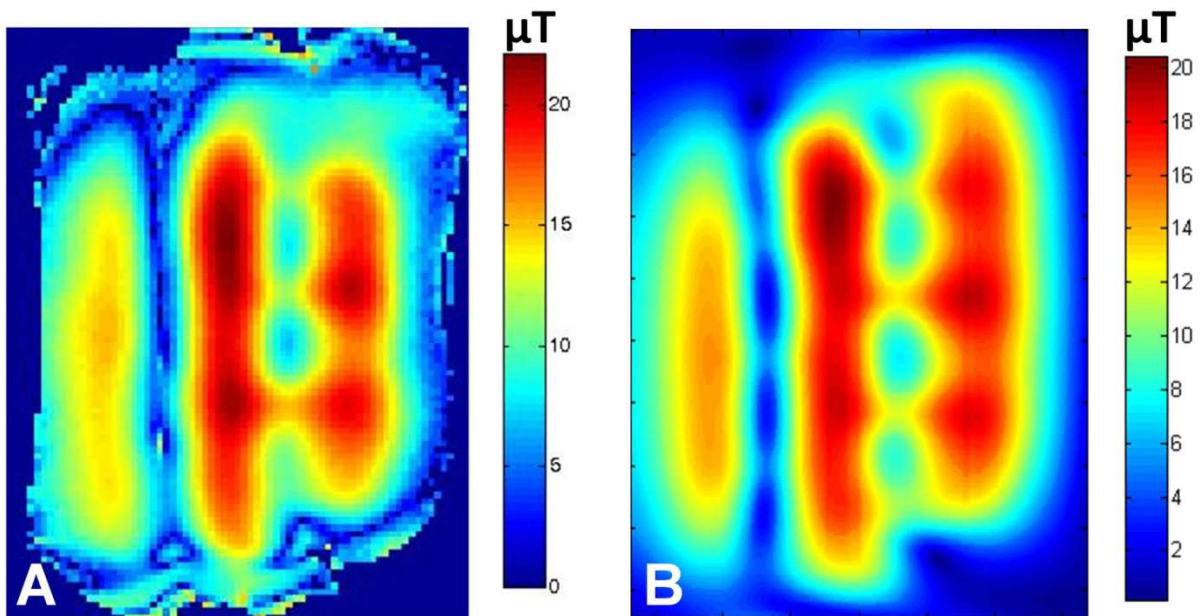


**Fig. 3.5:** For compliance,  $B_1^+$  maps were compared between measurement (A) and simulation (B) using coronal planes 2 cm inside the phantom. In both cases, similar  $B_1^+$  distributions as well as comparable values for maximum  $B_1^+$  were found.

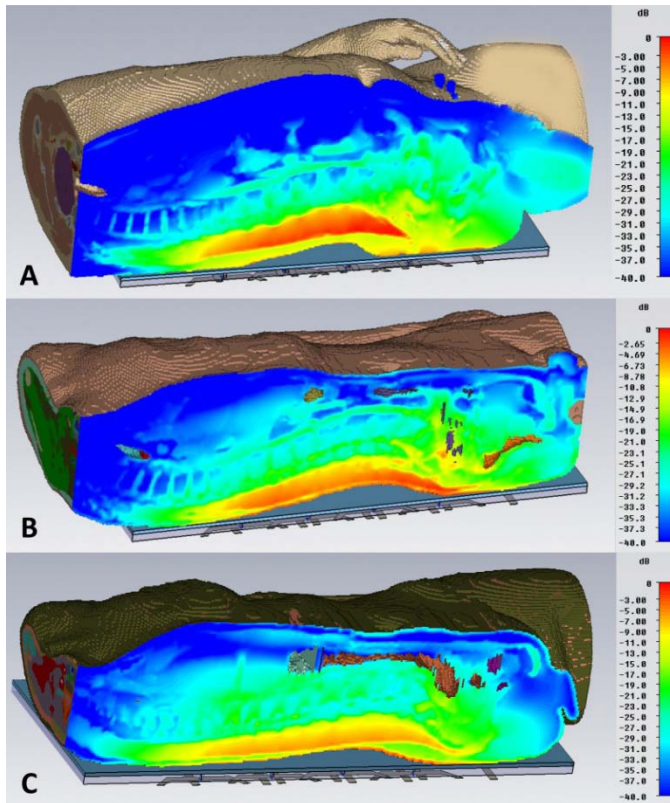


**Fig. 3.6:** SAR calculations using different human body models; Hugo (top, A), Duke (middle, B), and Ella (bottom, C). Shown is the voxel-based SAR (voxel size  $2 \text{ mm}^3$ ) on a logarithmic scale; images were normalized to their individual maximum.

Dataset	Lumbar spine	Cervical spine
Hugo	12.95 W	13.59 W
Duke	10.91 W	9.13 W
Ella	12.77 W	9.12 W
$P_{in}$ for in vivo measurements	12 W	9 W

**Tab. 3.2:** Maximum permitted input power (time-averaged)  $P_{in}$  in Watts calculated from numerical simulations using different human body models for which the localized (10 g averaged) SAR complies with the limit of 10 W/kg given in the guidelines.

In vivo images revealed a good and homogeneous excitation along the spine over a 40 cm FOV (see Fig. 3.7-3.9). Anatomic details such as the vertebral bodies, the longitudinal ligaments, and the venous drainage through the vertebrae were well visualized (Fig. 3.7). In a coronal scan, the predicted  $B_1^+$  signal cancellation parallel

to the centerline is outside the region of interest as expected; see Fig. 3.7. On the FLASH images, the vertebrae could be very well delineated, for example the dens in Fig. 3.8 (A, C). In a scan of the cervicothoracic spine, contrast between CSF and myelin was found to be good in the thoracic region but diminished caudally presumably due to flip angle variation (see Fig. 3.8 A). Additionally,  $B_1$  inhomogeneity caused a strong signal cancellation at vertebra T8 in Fig. 3.8 B. Nerve fibers of the cauda equina could be followed through the neural foramen in a sagittal scan of the thoracolumbosacral spine (see Fig. 3.8 B).

In Fig. 3.9 (A-C), coronal images of the male volunteer with a documented biconvex scoliosis are presented. The lateral curvature is visible over the whole spine (Fig. 3.9 A, C). As expected from the g-factor evaluation, a GRAPPA acceleration factor of 2.7 revealed good image quality compared to a 1.9-fold acceleration shown in Fig. 3.9 (A, B). On axial slices, nerve roots could be followed from the spinal cord (see Fig. 3.9 D).

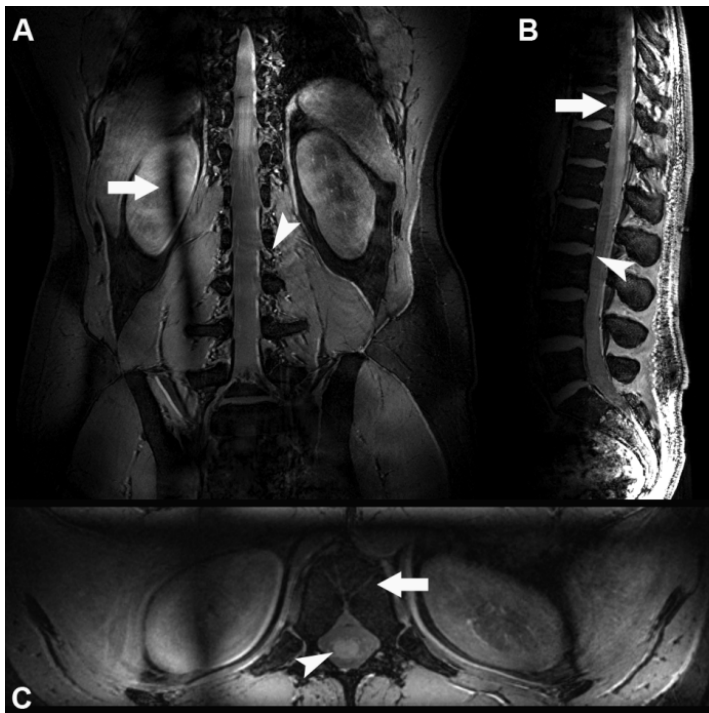


**Fig. 3.7:** Images of the thoracolumbosacral spine of a 31-year-old volunteer. In (A) note the residual longitudinal signal inhomogeneity (arrow) seen as a hypointense region in the otherwise homogeneous signal distribution. The arrowhead points to the good delineation of nerve root sleeves in this coronal view. In (B) the high spatial resolution is reflected by the depiction of the posterior longitudinal ligament (arrowhead), and by the delineation of the entry points of veins into the vertebrae

(arrow). The latter are also shown in an axial view in (C), arrow, with the spinal cord marked by the arrowhead.

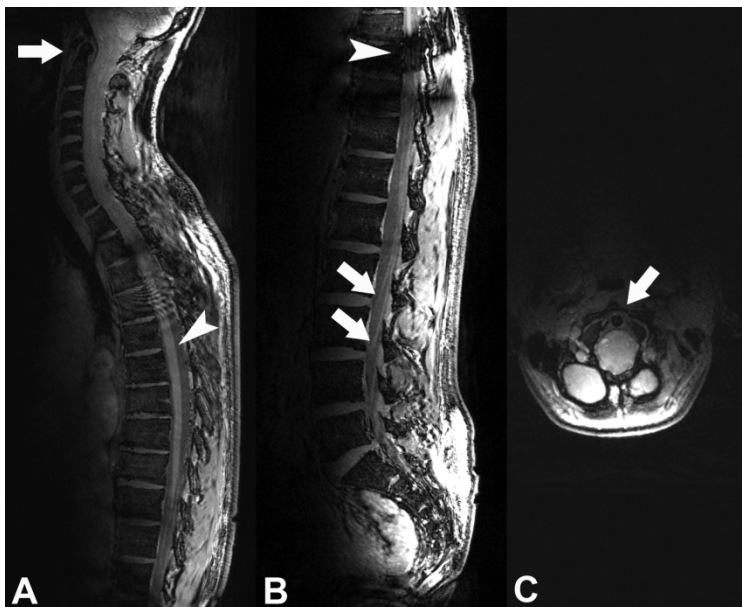


**Fig. 3.8:** Sagittal views of (A) cervicothoracic and (B) thoracolumbosacral spine of a female volunteer. Note the good visualization of the dens (A, arrow), which is also shown in an axial view in (C). In (A), the good contrast between myelin and CSF is pointed out (arrowhead), which diminishes cranially presumably due to flip angle variation. An artifact, assumedly from pulsation of the aorta, is also visible right above the arrowhead. In (B), B1 inhomogeneity caused a strong signal cancellation at vertebra T8 (arrowhead). Caudally, nerve fibers of the cauda equina can be followed very well through the neural foramen (arrows).



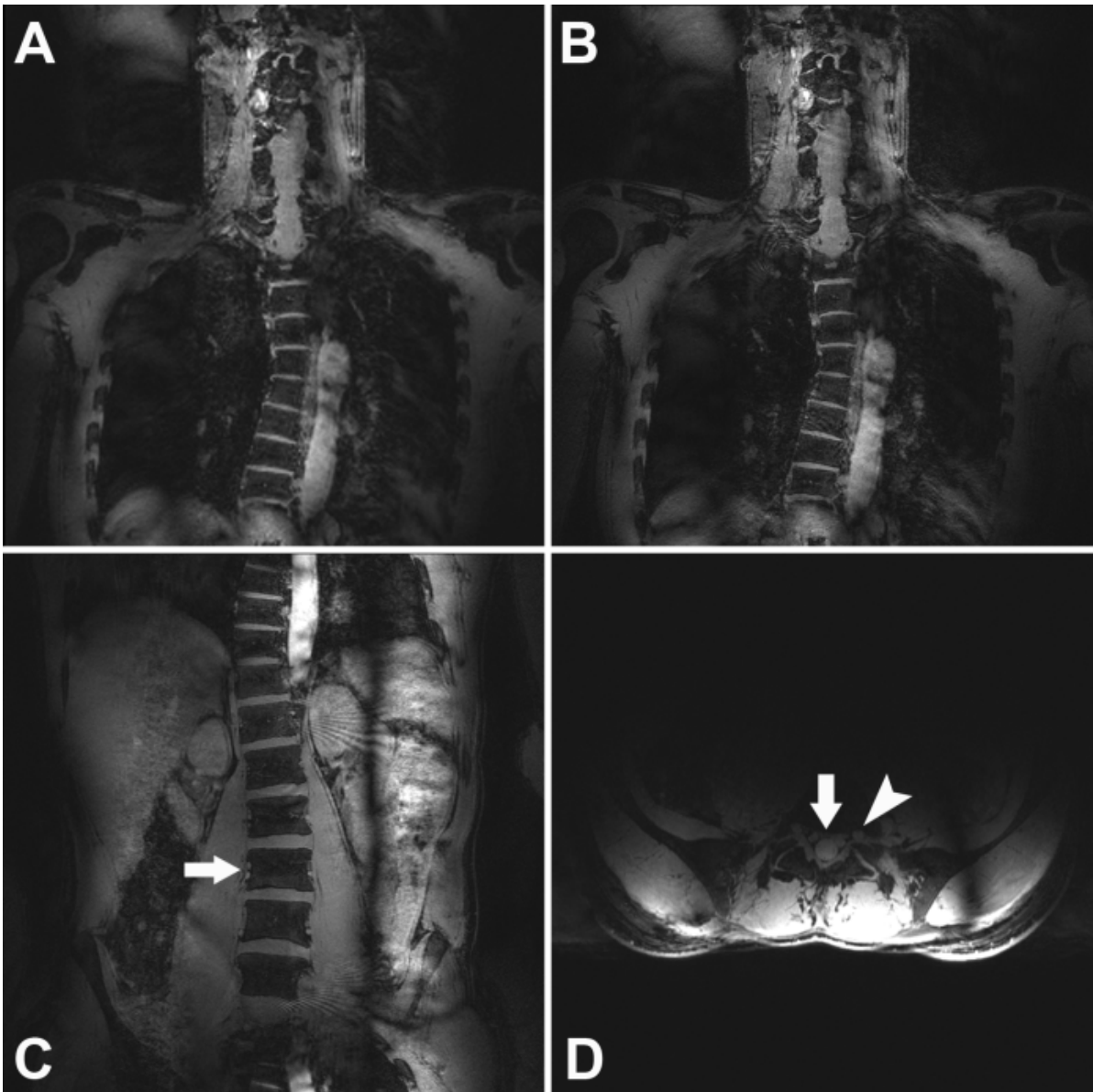


**Fig. 3.9:** Images of a male volunteer with a documented biconvex scoliosis. A comparison of GRAPPA acceleration factors of 1.9 and 2.7 is given in (A) and (B), respectively. Coronal views of the scoliosis of the (A) cervicothoracic and (C) thoracolumbosacral spine are presented. In (C), vessels are visible at the vertebrae (arrow). Nerve roots (arrowhead) can be followed from the spinal cord (arrow) on their way through the neural foramen in the axial slices of the lumbar spine (D).



### 3.4 Discussion

These early results indicate that a multi-channel transmit/receive phased array RF coil has successfully been designed and evaluated for in vivo spine imaging at 7 T, thereby rendering high-resolution spine imaging a promising new application in 7 T clinical research. To our knowledge, for the first time MR images with a large field of view of 40 cm could be obtained of a human spine at 7 T.

Since the coil has been developed for use in upcoming clinical studies, it is not intended that the coil be tuned in individual patients. Hence, a phantom of tissue simulating liquid was used as a load for tuning and matching, and the capacitor values were kept fixed after that. Of course, the S-parameters in Tab. 1 measured with a phantom load yielded better transmission and isolation values compared to those measured with a patient load, since the phantom could be positioned planar on the coil whereas the human spine is curved and introduces gaps between the coil elements and the tissue. Nevertheless, the transmission and isolation of the single elements with the patient load remained sufficient. For example, Element 1 yielded an S11 of -13 dB, but this means that only 5% of the input power will be reflected at the port.

The measurement of the ratio of unloaded to loaded Q showed that when the coil is individually tuned for the loaded and unloaded case, the ratio is relatively high. This is generally to be expected at 7 T with a loop coil of this size, where sample losses should be dominant. However, this retuning changes the characteristics of the coil. The measurement in which the unloaded coil was not retuned rendered a very low Q ratio which is in contradiction to the subjectively good image quality obtained with this coil. Although the ratio of unloaded to loaded Q is the most common coil-quality metric, it is more useful for homogenous volume coils and may be misleading for surface and array coils<sup>31</sup>, so that its significance should not be overweighted.

For an acceleration factor of 2.7 along the head-feet direction, the g-factor remained below 1.5 indicating adequate image quality not compromised by amplified noise and reconstruction artifacts, which could be validated subjectively in the in vivo

images. Since the array consists of two rows of four elements each, g-factors for acceleration in the right-left direction were significantly higher, as expected.

SAR scales approximately with the field strength squared and is a critical factor in 7 T MRI. For a transmit coil an intensive compliance test is obligatory including a validation of the coil model used in the numerical simulations. The presented  $B_1^+$  map comparison indicated a good coil model for the performed SAR calculations which were based on three different human body models to take SAR relevant variables such as bodyweight and physique into account. Similar values for the maximum permitted power level were found for all three datasets when the coil was placed for imaging the lumbar spine region. However, for imaging the cervical spine, the result from the Hugo dataset deviated significantly from those obtained with the Virtual Family datasets. The much higher allowed input power with the Hugo dataset calculation can be explained by a much larger distance between coil and neck. The anatomical configuration of the Hugo model did not allow optimal positioning of the spine array in the cervical region. In contrast to the Virtual Family datasets, the Hugo dataset was not obtained from an MRI examination but from a dissected male corpse portioned into several thousand slices. Hence, the posture of the Hugo model is fundamentally different from the Virtual Family models. Furthermore, the Hugo model consists of only 33 different tissues, whereas the Virtual Family models are based on over 80.

In the in vivo images, the delineation of very fine structures such as the longitudinal ligaments or the venous plexus as well as its drainage through the vertebral bodies reflects the very high resolution of 0.57 mm isotropic. Osseous structures appear ideally on the 7 T images with a high contrast to intervertebral disks and ligaments, which might aid in the diagnosis of herniated disk and disk degeneration.

Large FOV imaging is important for assessing patients with metastases or multiple sclerosis lesions in the spinal cord, for example. Although good contrast between CSF and myelin was achieved over a substantial part of the FOV, apparent flip angle variations diminished contrast in some regions and need to be addressed.

With the ability to apply recent developments like RF shimming <sup>16</sup> or Transmit SENSE techniques <sup>19</sup> using the proposed multi-channel transmit coil, further improvements in image quality can be expected.

Driven by emerging RF coil and other technical developments, the number of clinically-oriented studies at UHF has increased dramatically over the last two years. While most of the recent research at 7 T has been conducted in the brain investigating non-contrast enhanced MR angiography <sup>32</sup> or new techniques for functional MRI <sup>33</sup>, for example, 7 T MRI is more and more expanding its potential to whole-body imaging as well. Quantitative MRI for assessing the musculoskeletal system is advancing and offers potential advantages for analyzing cartilage degeneration <sup>10,34</sup>. Furthermore, the feasibility of imaging abdominal organs such as the prostate <sup>35</sup> or heart <sup>36</sup> at 7 T has been shown.

Of course, 7 T ultra-high field MR imaging of the spine with the presented coil needs to be evaluated for a variety of pathologies and patients to further discuss the clinical impact of this technology. Additionally, gradient and especially spin echo sequences have to be optimized for contrast, SAR, and spatial coverage to be included in a dedicated 7T spine imaging protocol. Currently, work is underway to pursue this task.

## References

1. Tanenbaum LN. Clinical 3T MR imaging: mastering the challenges. *Magnetic resonance imaging clinics of North America* 2006;14(1):1-15.
2. Shapiro MD. MR imaging of the spine at 3T. *Magnetic resonance imaging clinics of North America* 2006;14(1):97-108.
3. Wattjes MP, Harzheim M, Kuhl CK, et al. Does high-field MR imaging have an influence on the classification of patients with clinically isolated syndromes according to current diagnostic mr imaging criteria for multiple sclerosis? *Ajnr* 2006;27(8):1794-1798.
4. Wattjes MP, Harzheim M, Lutterbey GG, et al. Does high field MRI allow an earlier diagnosis of multiple sclerosis? *Journal of neurology* 2008.
5. Bot JC, Barkhof F, Polman CH, et al. Spinal cord abnormalities in recently diagnosed MS patients: added value of spinal MRI examination. *Neurology* 2004;62(2):226-233.
6. Bakshi R, Thompson AJ, Rocca MA, et al. MRI in multiple sclerosis: current status and future prospects. *Lancet neurology* 2008;7(7):615-625.
7. Schenck JF, Zimmerman EA. High-field magnetic resonance imaging of brain iron: birth of a biomarker? *NMR in biomedicine* 2004;17(7):433-445.
8. Kollia K, Maderwald S, Putzki N, et al. First clinical study on ultra-high-field MR imaging in patients with multiple sclerosis: comparison of 1.5T and 7T. *Ajnr* 2009;30(4):699-702.
9. Rooney WD, Johnson G, Li X, et al. Magnetic field and tissue dependencies of human brain longitudinal  $1\text{H}_2\text{O}$  relaxation in vivo. *Magn Reson Med* 2007;57(2):308-318.
10. Krug R, Stehling C, Kelley DA, Majumdar S, Link TM. Imaging of the musculoskeletal system in vivo using ultra-high field magnetic resonance at 7 Tesla. *Invest Radiol* 2009;44(9):613–618.
11. Roemer PB, Edelstein WA, Hayes CE, Souza SP, Mueller OM. The NMR phased array. *Magn Reson Med* 1990;16(2):192-225.
12. Hayes CE, Hattes N, Roemer PB. Volume imaging with MR phased arrays. *Magn Reson Med* 1991;18(2):309-319.

13. Peterson DM, Duensing GR, Caserta J, Fitzsimmons JR. An MR transceiver phased array designed for spinal cord imaging at 3 Tesla: preliminary investigations of spinal cord imaging at 3 T. *Investigative radiology* 2003;38(7):428-435.
14. Van de Moortele PF, Akgun C, Adriany G, et al. B(1) destructive interferences and spatial phase patterns at 7 T with a head transceiver array coil. *Magn Reson Med* 2005;54(6):1503-1518.
15. Hoult DI, Phil D. Sensitivity and power deposition in a high-field imaging experiment. *J Magn Reson Imaging* 2000;12(1):46-67.
16. Mao W, Smith MB, Collins CM. Exploring the limits of RF shimming for high-field MRI of the human head. *Magn Reson Med* 2006;56(4):918-922.
17. Metzger GJ, Snyder C, Akgun C, Vaughan T, Ugurbil K, Van de Moortele PF. Local B1+ shimming for prostate imaging with transceiver arrays at 7T based on subject-dependent transmit phase measurements. *Magn Reson Med* 2008;59(2):396-409.
18. van den Bergen B, Van den Berg CA, Bartels LW, Lagendijk JJ. 7 T body MRI: B1 shimming with simultaneous SAR reduction. *Physics in medicine and biology* 2007;52(17):5429-5441.
19. Katscher U, Bornert P, Leussler C, van den Brink JS. Transmit SENSE. *Magn Reson Med* 2003;49(1):144-150.
20. Setsompop K, Wald LL, Alagappan V, et al. Parallel RF transmission with eight channels at 3 Tesla. *Magn Reson Med* 2006;56(5):1163-1171.
21. Yee K. Numerical solutions of initial boundary value problems involving Maxwell's equations in isotropic media. *IEEE Transactions on antennas and Propagation* 1966;14:302-307.
22. Firbank MJ, Coulthard A, Harrison RM, Williams ED. A comparison of two methods for measuring the signal to noise ratio on MR images. *Physics in medicine and biology* 1999;44(12):N261-264.
23. Griswold MA, Jakob PM, Heidemann RM, et al. Generalized autocalibrating partially parallel acquisitions (GRAPPA). *Magn Reson Med* 2002;47(6):1202-1210.

24. Porter JR, Wright SM, Reykowski A. A 16-element phased-array head coil. *Magn Reson Med* 1998;40(2):272-279.
25. CST MICROWAVE STUDIO®, CST GmbH. User Manual Version 2008. Darmstadt, Germany.
26. The Visible Human Project, <http://vhp.ntu.edu.sg/>.
27. Christ A, Kainz W, Hahn EG, et al. The Virtual Family--development of surface-based anatomical models of two adults and two children for dosimetric simulations. *Physics in medicine and biology* 2010;55(2), N23-38.
28. Yarnykh VL. Actual flip-angle imaging in the pulsed steady state: a method for rapid three-dimensional mapping of the transmitted radiofrequency field. *Magn Reson Med* 2007;57(1):192-200.
29. Vizmuller P. RF design guide: systems, circuits, and equations Artech House, Inc.; 1995. 233-237 p.
30. International Electrotechnical Commission. Medical electrical equipment - Part 2-33: Particular requirements for the safety of magnetic resonance diagnostic devices. IEC 60601-2-33; 2002.
31. Doty FD, Entzminger G, Kulkarni J, et al. Radio frequency coil technology for small-animal MRI. *NMR in biomedicine* 2007;20(3):304-325.
32. Maderwald S, Ladd SC, Gizewski ER, et al. To TOF or not to TOF: strategies for non-contrast-enhanced intracranial MRA at 7 T. *Magma* 2008;21(1-2):159-167.
33. Utting JF, Kozerke S, Luechinger R, et al. Feasibility of k-t BLAST for BOLD fMRI with a spin echo acquisition at 3 Tesla and 7 Tesla. *Invest Radiol* 2009;44(9):495–502.
34. Welsch GH, Mamisch TC, Hughes T, et al. In vivo biochemical 7.0 Tesla magnetic resonance: preliminary results of dGEMRIC, zonal T2, and T2\* mapping of articular cartilage. *Invest Radiol* 2008;43(9):619-626.
35. Klomp DW, Bitz AK, Heerschap A, Scheenen TW. Proton spectroscopic imaging of the human prostate at 7 T. *NMR in biomedicine* 2009.
36. van Elderen SG, Versluis MJ, Webb AG, et al. Initial results on in vivo human coronary MR angiography at 7 T. *Magn Reson Med* 2009;62(6):1379-1384.

# Chapter 4    **A transmit/receive RF array for imaging the carotid arteries at 7 T: Coil design and first in-vivo results\***

## Abstract

This study presents a novel transmit/receive RF array for MRI of the carotid arteries at 7 T. The prototype is characterized in numerical simulations and bench measurements, and the feasibility of plaque imaging at 7 T is demonstrated in first in-vivo images.

The RF phased array coil consists of eight surface loop coils. To allow imaging of both sides of the neck, the RF array is divided into two coil clusters, each with four overlapping loop elements. For safety validation, numerical computations of the RF field distribution and the corresponding SAR were performed based on a heterogeneous human body model. To validate the coil model, maps of the transmit  $B_1^+$  field were compared between simulation and measurement. In vivo images of a healthy volunteer and a patient were acquired.

A similar distribution and a very good match of the absolute values were found between the measured and simulated  $B_1^+$  transmit RF field for the validation of the coil model. In vivo images revealed good signal excitation of both sides of the neck and a high vessel-to-background image contrast for the non-contrast-enhanced 3D FLASH sequence. 7 T could depict the extent of stenosis, and revealed the disruption and ulcer of the plaque.

This study demonstrates that two four-channel transmit/receive RF arrays for each side of the neck is a suitable concept for in vivo MR imaging of the carotid arteries at 7 T.

\* **Kraff O**, Bitz AK, Breyer T, Kruszona S, Maderwald S, Brote I, Gizewski ER, Ladd ME, Quick HH. A transmit/receive RF array for imaging the carotid arteries at 7 Tesla: Coil design and first in-vivo results. *Invest Radiol.* 2011;46(4): 246-254.

## 4.1 Introduction

Driven by emerging radiofrequency (RF) coil and other technical developments, the number of clinically-oriented magnetic resonance imaging (MRI) studies at ultra-high magnetic field strengths, i.e. 7 Tesla (T) and above, has increased dramatically over the recent years. While most of the current research at 7 T has been conducted on the brain, investigating, for example, non-contrast-enhanced magnetic resonance angiography (MRA) of subtle microvascular diseases <sup>1</sup> or new techniques for functional studies <sup>2</sup>, 7 T MRI is more and more expanding its potential to whole-body imaging as well <sup>3-5</sup>. MRI at 7 T is of significant interest since it provides an opportunity for increases in spatial resolution or acquisition speed while revealing novel imaging contrasts <sup>6-7</sup>. At 7 T, fast gradient echo sequences show hyperintense vascular signal even without administration of contrast agent <sup>8</sup>. A first look at the potential of 7 T carotid imaging was presented at recent conferences <sup>9-11</sup>, indicating a need for new dedicated high-field local transmit receive RF coils to allow both parallel imaging techniques as well as simultaneous imaging of both carotid arteries for a side-by-side comparison.

Challenges at 7 T include increases in the specific absorption rate (SAR), severe RF field inhomogeneities, as well as enhanced susceptibility and chemical shift artifacts. Hence, RF technology, imaging sequences, and scan protocols require major modifications to provide optimal image quality and to obey safety regulations. Any 7 T RF coil must include transmit capability, since integrated transmit body RF coils are not routinely available at this field strength. Effects of electromagnetic wave propagation in tissue leading to destructive interferences and asymmetric distributions of the excitation radiofrequency magnetic field ( $B_1^+$ ) over the imaging sample are already prominent at 3 T. These effects and their associated signal inhomogeneities increase even further when moving to 7 T <sup>12</sup>. This necessitates numerical simulations for both the design process of a 7 T coil and for subsequent characterization and safety compliance testing.

3 T MRI has already demonstrated improved vascular imaging with increased signal-to-noise ratio (SNR) and contrast-to-noise ratio (CNR) compared to 1.5 T MRI <sup>13</sup>. Vascular diseases, atherosclerosis in particular, cause high morbidity and



disability worldwide. Accurate characterization and quantification of the plaque components in relation to the fibrous cap and the vascular lumen are important to identify and monitor high-risk patients <sup>14-15</sup>. Contrast-enhanced MRA is currently the most widely performed imaging technique (at 1.5 T and 3 T) for an accurate estimation of carotid stenosis <sup>16-18</sup>. Additionally, preoperative MRA provides important anatomical information not easily visible on ultrasounds (US) as well as a high reproducibility of imaging results <sup>19</sup> that is inherently less user-dependent than US imaging. Furthermore, for diagnostic purposes, MRA can replace digital subtraction angiography (DSA), which is an invasive procedure associated with a low but definite incidence of complications <sup>20-21</sup>.

The carotid artery bifurcation has the highest incidence of plaque formation, and since it tends to be relatively superficial, surface RF coils and phased-array coils <sup>22</sup> in particular are advantageous <sup>23-24</sup>. In this work, an eight-channel transmit/receive RF array was built for imaging the carotid arteries at 7 T. The array was made of four overlapping surface loop coils per side to form a 2 x 4-channel RF array to assess both arteries in one acquisition. We characterize this prototype in simulations and bench measurements and show first in vivo results.

## 4.2 Methods:

### *RF Coil Design and Construction*

The carotid array was developed for a 7 T whole-body MR scanner (Magnetom 7 T, Siemens Healthcare Sector, Erlangen, Germany) featuring a 60 cm bore. Eight square surface loop coils with a dimension of 6 x 7 cm were machined from FR4 circuit board material (LPKF Laser & Electronics AG, Garbsen, Germany).

Each coil element was 0.8 mm thick and has 5-mm-wide circuits with a copper-clad layer of 35  $\mu\text{m}$  thickness. Three 2-mm gaps in each loop were bridged by 8.2 pF non-magnetic capacitors (Voltronics Corporation, Denville, NJ, USA). Common-mode cable current suppression was provided by a cable trap formed by a 6.5 cm long semi-rigid coaxial cable wound in two turns in parallel with a variable capacitor (2.5-10 pF, Murata Manufacturing Co., Ltd.). The cable trap was tuned to approximately 297 MHz. To keep the overall dimensions of the array minimal, the cable trap was placed directly at each coil element and orthogonal to the loop plane (Fig. 4.1).

To allow imaging of both sides of the neck, two coil clusters, each with four loop elements, were combined to one RF array. All neighboring coil pairs were overlapped to reduce the mutual inductance<sup>22</sup>. Furthermore, finite-difference-time-domain (FDTD)<sup>25</sup> simulations of the field distribution indicated use of a shifted (by 21 mm) and overlapped (12 mm) arrangement of the coil elements as given in Fig. 4.1, which was validated experimentally when loading the coil with a bottle phantom (22.0 cm x 13.5 cm x 13.5 cm) with homogeneous electrical properties of  $\epsilon_r = 43$  and  $\sigma = 0.8 \text{ S}\cdot\text{m}^{-1}$ . For the numerical simulations, a phantom with the same dimensions and electrical properties was used, and different overlaps and shifts of the coil rows were evaluated.

An identical cable length of 85 cm was used for all eight elements as determined by preamplifier decoupling<sup>22</sup>. The elements were fed with opposite polarity between the two coil rows to provide a 180° phase shift (i.e., between elements 1/2 and 3/4, as well as between 5/6 and 7/8). Hence, the currents of both

rows pointed in the positive z direction along the centerline loop paths and increased the  $B_1^+$  amplitude in the region of interest, i.e. along the carotid artery.

The elements were each matched to 50 Ohms at 297 MHz. Tuning and matching were optimized on the bench with a nearly square cylindrical bottle phantom (22.0 cm x 13.5 cm x 13.5 cm) filled with body-simulating liquid ( $\epsilon_r = 43$ ,  $\sigma = 0.8 \text{ Sm}^{-1}$ ) and assessed with a network analyzer (Agilent E5061A, Santa Clara, CA, USA). S-parameters were determined in the loaded condition both with the bottle phantom and with the neck of a human volunteer. Additionally, loaded and unloaded Q values were obtained.

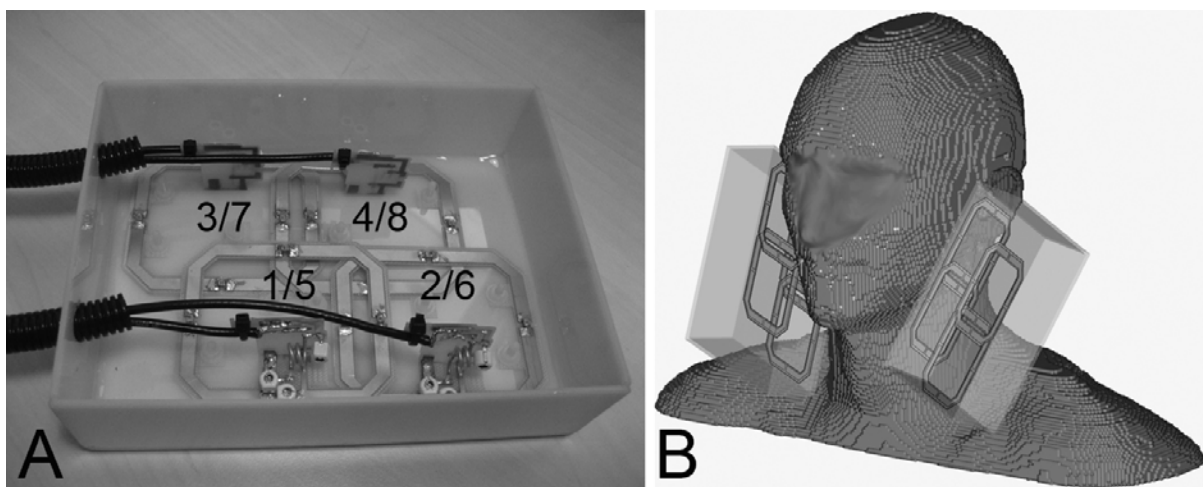


**Fig. 4.1:** Photograph of the carotid RF coil (A) and model for numerical simulations (B). (A) shows one side of the carotid array coil featuring 4 geometrically overlapping RF transmit/receive loop coil elements. The numbering gives the element numbers used in the text for the two coil clusters. (B) shows the angled positioning of the RF coil model on the human model, similar to the actual *in vivo* measurements.

To acquire data for g-factor maps, two fully sampled datasets of the phantom were obtained using a gradient echo sequence with  $TR/TE = 26/12 \text{ ms}$ ,  $20^\circ$  flip angle,  $0.7 \times 0.7 \times 5.0 \text{ mm}^3$  resolution, and matrix  $384 \times 384$ . Undersampled datasets were generated by omitting phase encoding lines using the OpenGRAPPA algorithm<sup>26</sup> with effective acceleration factors of  $R = 1.8, 2.4$  and  $2.9$  (using 48 reference lines<sup>27</sup>). Estimates of the SNR were made with the difference method<sup>28</sup>. By subtracting the two images, a noise image was generated; the signal was determined in the sum

image of the two images. Finally, g-factor maps were calculated pixelwise by the following equation:  $g\text{-factor} = \text{SNR}^{\text{full}} / (\text{SNR}^{\text{accel.}} * \sqrt{R})$ .

Additionally, a noise correlation matrix was calculated out of uncombined single-channel images using a turbo-fast low-angle shot (TurboFLASH) sequence without RF pulses.

### *FDTD simulations*

For safety validation, numerical computations<sup>25</sup> of the RF field distribution and the corresponding SAR were performed on the male member “Duke” of the Virtual Family<sup>29</sup> (70 kg weight, 1.74 m height, including more than 80 different tissue types). The tissue resolution was 2 mm. The carotid array was modeled using the exact dimensions and characteristics of the physical coil including array geometry, conductor width, gap sizes of the capacitors as well as their capacitance of 8.2 pF, and the 2-mm-thick plate of Makrolon (Bayer Material Science AG, Leverkusen, Germany) which was used for housing the coil. The cable traps were orthogonal to the loop plane, i.e. pointing away from the patient. Since a sufficiently large distance of approximately 2 cm to the body tissue was maintained, their influence on  $B_1^+$  and SAR distribution in the human body is negligible. For this reason the cable traps were not simulated to avoid the significantly higher computational cost. The coil elements were located 7 mm (2 mm housing plus 5-mm-thick neoprene matting) from the neck surface of the human body model and were angled similar to the real imaging situation. Care was taken to place the center of the coil over the carotid bifurcation. In the simulation, the elements were excited individually with 0.5 W power and were subsequently vectorially combined. The calculations were done in free space over approximately 40 million grid points.

To validate the numerical model of the array, S-parameters were compared between simulation and bench measurements. Additionally,  $B_1^+$  maps were compared. Experimental  $B_1^+$  maps utilized the actual flip angle imaging (AFI) sequence<sup>30</sup> with the following parameters: TR1 = 20 ms, TR2 = 100 ms, TE = 2.04 ms, nominal flip angle of 45°, 250  $\mu$ s square pulse, matrix 64 x 64, resolution 3.0 x 3.0 x 5.0 mm<sup>3</sup>.

For further safety validation, temperature measurements were performed during typical gradient and spin echo sequences, as introduced in the next section. Four fiber optic probes (Luxtron, California, USA), which can monitor the temperature during MRI measurements, were carefully placed at various positions across a phantom filled with body-simulating liquid. One probe was placed approximately 1-2 mm within the phantom at the location of maximum calculated SAR, where the highest temperature elevation is expected. Two probes were placed 15 mm and 50 mm within the phantom, and the fourth probe served as a reference.

### *In vivo studies*

In vivo studies were performed with signed consent and were approved by the institutional review board. Three volunteers were included.

A 28-year-old healthy male (70 kg, 1.74 m) with no history of vascular disease and a 69-year-old male (80 kg, 1.87 m) with a known ulcerating plaque and a 50% stenosis of the right internal carotid artery were assessed with high-resolution MR angiography (MRA) images of the entire neck with a 0.54 mm isotropic, non-contrast-enhanced 3D FLASH sequence with the following parameters: TR/TE = 5.5/2.2 ms, 15° flip angle, BW = 385 Hz/pixel, GRAPPA acceleration factor 1.8, TA = 3:47 min. Additionally, axial, pulse-triggered PD/T2-weighted turbo spin echo (TSE) images with TE = 29/77 ms, 180° flip angle, BW = 280 Hz/pixel, GRAPPA acceleration factor 1.8, matrix = 512 x 512, and 0.35 x 0.35 x 3 mm<sup>3</sup> resolution were acquired.

Furthermore, a 26-year-old healthy male (82 kg, 1.83 m) was imaged for a comparison of the 7 T FLASH sequence with a clinical 1.5 T time-of-flight (3D TOF) sequence. At 1.5 T, a Magnetom Espree system (Siemens Healthcare Sector, Erlangen, Germany) in combination with a vendor-provided 4-channel neck RF receive coil was used. The TOF sequence used the following parameters: TR/TE = 26/7 ms, 25° flip angle, 3 slabs, BW = 100 Hz/pixel, 0.7 x 0.7 x 1 mm<sup>3</sup> resolution, and TA = 7:15 min. A 3D FLASH sequence with the same parameters as at 7 T but lower resolution (0.8 mm isotropic) was also performed at 1.5 T for comparison.

## 4.2 Results:

S-parameter measurements on the bench yielded an  $S_{11}$  match of the loaded coil between -18 dB and -26 dB for the phantom load for all coil elements.  $S_{12}$  coupling between elements was measured with the loaded coil by transmitting with the network analyzer through one coil element while receiving through another. The shifted arrangement of the two coil rows significantly improved the isolation between neighboring as well as next-nearest-neighbor coils by approximately an additional -7 dB compared to the non-shifted design. With the final design,  $S_{12}$  was found to be -13 dB or better for the phantom load. Similar values were found for the patient load, i.e.  $S_{11}$  was between -19 dB and -25 dB and  $S_{12}$  was better than -12 dB. Since the S-parameters differed only at the first decimal between  $S_{12}$  and  $S_{21}$ , only half of the scattering matrix is provided in Table 1 for reasons of clarity. In the numerical simulations, similar S-parameters were found compared to the bench measurements.

The unloaded to loaded Q ratio was measured under two conditions. First, the coil with fixed tuning and matching was used, yielding an unloaded to loaded Q ratio of 1.7 for a single element in the presence of all other elements. Second, a single element of the array was used alone and retuned to 297 MHz for the unloaded case, so that the unloaded to loaded Q ratio, here 3.2, gives a better insight into conductive losses of the coil alone<sup>31</sup>.

Coronal and axial g-factor maps are given in Fig. 4.2 for effective acceleration factors of 1.8, 2.4, and 2.9 with phase-encoding directions along head-feet (HF) and anterior-posterior (AP). Mean g-factors were 1.1, 1.2, and 1.4 for the coronal maps (HF) and 1.1, 1.4, and 1.7 for the axial maps (AP). Additionally, the maps give a feeling for the signal penetration depth of the coil in the given directions.

Noise correlation was found to be better than -18 dB on average between neighboring elements which is shown in Fig. 4.3.

	S1	S2	S3	S4	S5	S6	S7	S8
S1	-23 / -19							
S2	-17 / -16	-21 / -22						
S3	-17 / -16	-17 / -19	-20 / -20					
S4	-16 / -17	-14 / -13	-13 / -12	-26 / -25				
S5	-40 / -42	-44 / -43	-48 / -46	-44 / -44	-23 / -19			
S6	-45 / -44	-40 / -40	-41 / -40	-41 / -42	-15 / -15	-22 / -23		
S7	-41 / -41	-45 / -44	-42 / -42	-47 / -44	-14 / -14	-16 / -15	-24 / -23	
S8	-40 / -42	-46 / -45	-50 / -44	-41 / -43	-16 / -18	-16 / -14	-16 / -14	-18 / -19

**Tab. 4.1:** S-parameter measurements obtained under two conditions: coil loaded with phantom (left values) and coil loaded with the neck of a volunteer (right values). The values for both load conditions show good correlation indicating load insensitive performance of the carotid RF coil and, hence, no need for individual patient tuning. The values are given in dB.

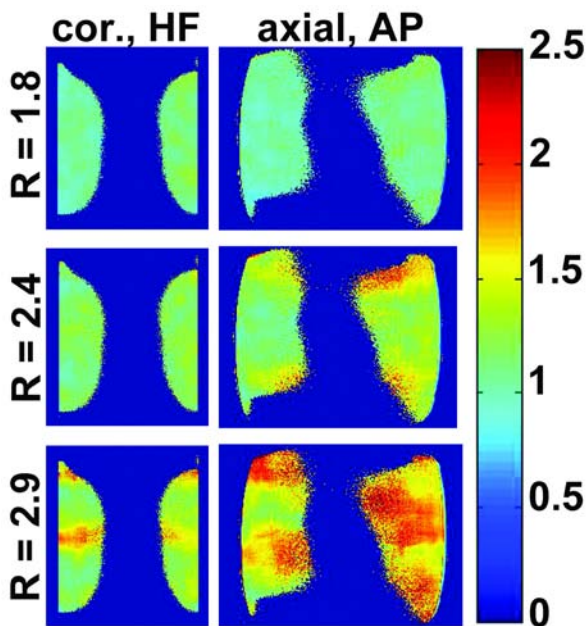


**Fig. 4.2:** GRAPPA g-factor maps of the 2x4-channel carotid RF coil acquired on a bottle phantom simulating the human neck. The g-factor maps show the spatially variant noise distribution of the coil in two orientations (coronal with phase-encoding direction in head-feet (HF), and axial with phase-encoding direction in anterior-posterior (AP)) as a function of increasing effective acceleration factor ( $R=1.8$ ;  $R=2.4$ ;  $R=2.9$ ). Red color indicates areas with high g-factors for acceleration factors  $R$  above 2.4.

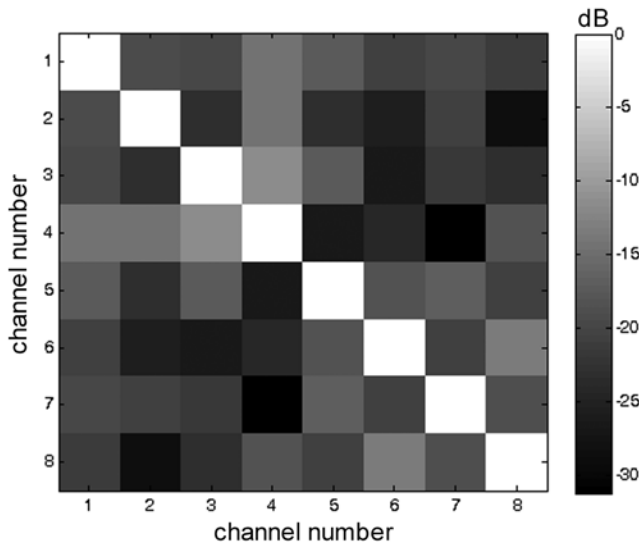


**Fig. 4.3:** Noise correlation matrix. Self-correlation of the elements along the diagonal of the matrix has been normalized to 0 dB. The average noise coupling between individual elements in the coil remained low (mean coupling = -18 dB, peak = -11 dB).

In Fig. 4.4, comparisons between the measured and the simulated  $B_1^+$  distribution of two sagittal planes approximately 0.8 cm and 2 cm inside the phantom are given. A similar  $B_1^+$  distribution was found for both planes between measurement and simulation, and the maximum  $B_1^+$  values varied by less than 9%. The maximum permitted input power level (accepted power, i.e. forward minus reflected) for compliance with the IEC guidelines<sup>32</sup> of 10 W/kg for 10 g-averaged local SAR was 7.9 W (total RF power at coil plug, equally split to all coil channels). In Fig. 4.5, the SAR distribution is shown on a lateral view as well as on an axial plane. The latter was taken at the SAR hot spot.

For the RF-intense TSE sequence with 7.9 W input power and 1:31 min acquisition time, a temperature increase of  $0.25^\circ$  was measured for the probe at the calculated RF hot spot. The second probe, 15 mm within the phantom, registered a temperature increase of only  $0.1^\circ$ , while the other two probes did not detect any significant changes in temperature. A temperature increase of  $0.15^\circ$  was measured at the RF hot spot for the FLASH sequence with 1.8 W input power and 3:47 min acquisition time.



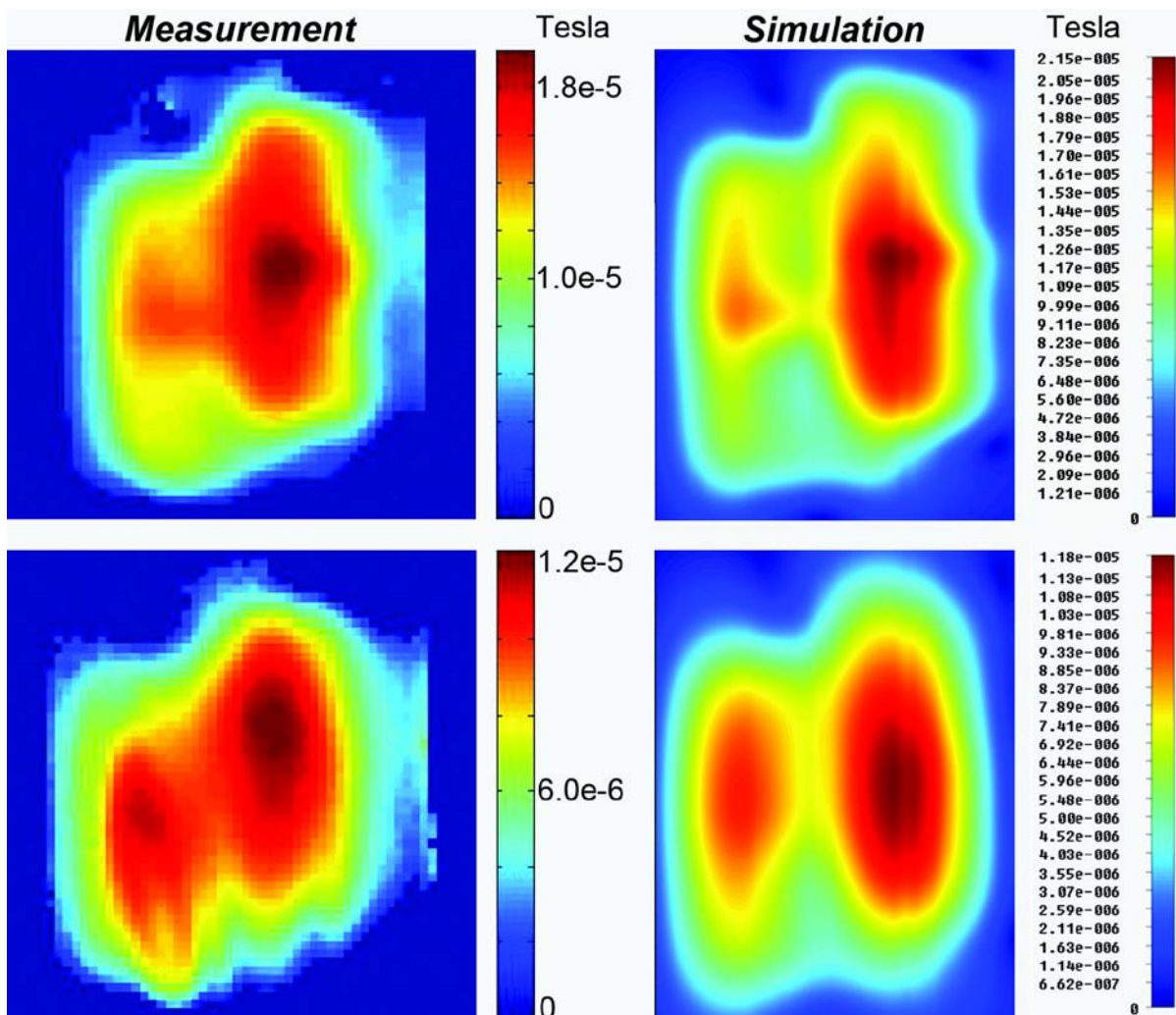


**Fig. 4.4:** Validation of the coil model used in the numerical simulation. Measured  $B_1^+$  maps (left) were compared with simulated  $B_1^+$  maps (right) regarding field distribution and maximum  $B_1^+$  values for two sagittal planes 0.8 cm (upper row) and 2.0 cm (lower row) inside the phantom. The planes are shown exemplarily for one side only. The maximum  $B_1^+$  values found were 19.6  $\mu\text{T}$  vs. 21.5  $\mu\text{T}$ , and 12.4  $\mu\text{T}$  vs. 11.8  $\mu\text{T}$ , respectively.

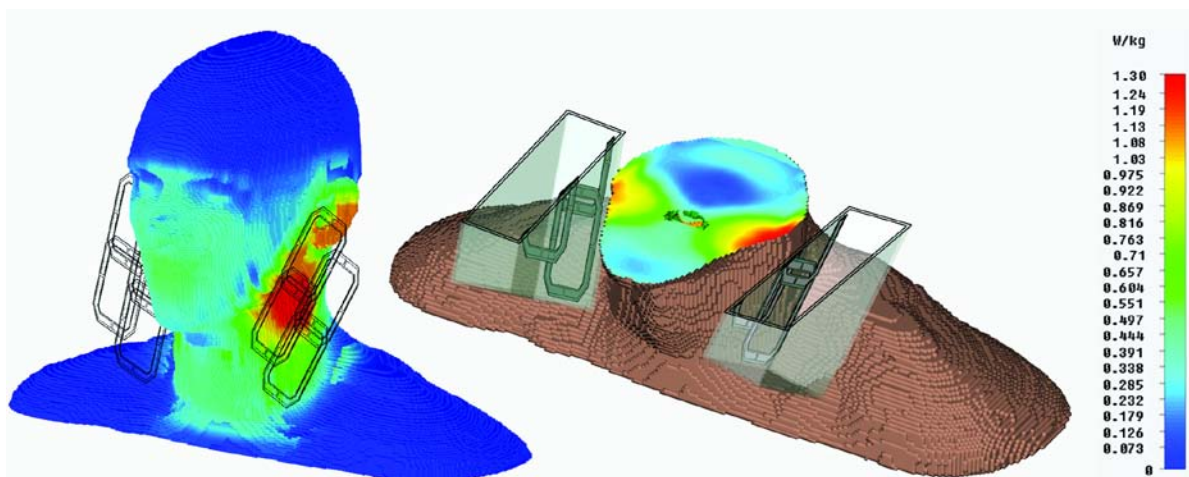


**Fig. 4.5:** SAR calculations using the Virtual Family human body model “Duke”<sup>29</sup>. Shown is the 10-g-averaged SAR on a logarithmic scale. The axial view (right) shows the plane with the highest SAR value (1.27 W/kg). Please note that the most critical region in the human head, the eyes, show relatively low SAR values.

Although this prototype was built with a rigid, non-flexible housing and has relatively large overall dimensions, it could be positioned well on the two subjects. A strip of Velcro around the neck was used to fixate the two coil clusters.

A comparison of the non-contrast enhanced sequences (3D TOF at 1.5 T and 3D FLASH at 7 T) for MR angiography of the carotid arteries is provided in Fig. 4.6. While the 1.5 T TOF sequence provides adequate vessel-to-background signal and good background signal suppression, the 3D FLASH sequence at this field strength (not shown in Fig. 4.6) does not provide any signal enhancement. At 7 T, however, 3D FLASH imaging provides strong vascular signal enhancement combined with more vascular detail compared to 1.5 T TOF due to the higher spatial resolution acquired in the 7 T data set.



**Fig. 4.6:** Comparison of the non-contrast enhanced sequences 3D TOF at 1.5 T and 3D FLASH at 7 T for MR angiography of the carotid arteries. While the 1.5 T TOF sequence provides adequate vessel-to-background signal and good background signal suppression (A), the 3D FLASH sequence at this field strength does not provide any signal enhancement (not shown). At 7 T, however, 3D FLASH imaging (B) provides strong vascular signal enhancement combined with more vascular detail due to the higher spatial resolution acquired in the 7 T dataset.

In vivo images reveal good signal excitation of both sides and a high vessel-to-background image contrast for the non-contrast-enhanced 3D FLASH sequence (Fig. 4.7 A-D). Although the signal intensity is less for the pulse-triggered TSE compared to the 3D FLASH, the vessel walls of the internal and external carotid arteries are well visualized (Fig. 4.7 E,F).

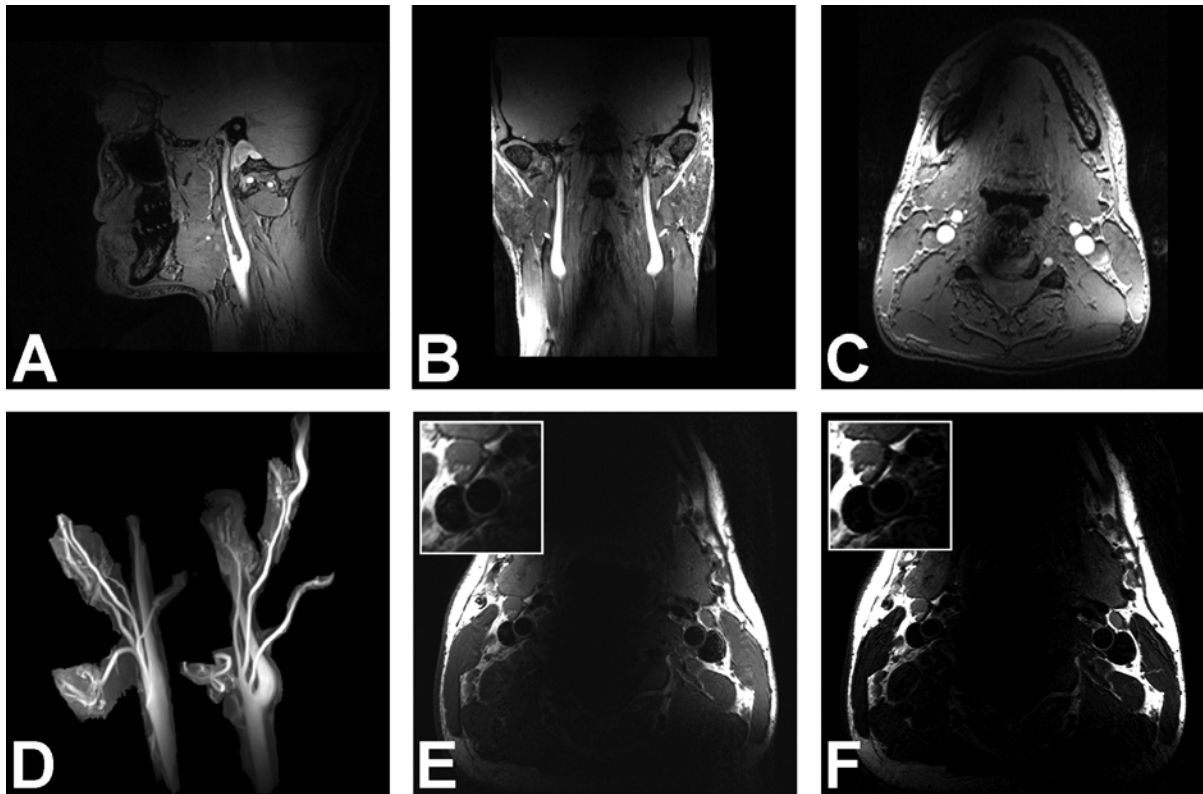


**Fig. 4.7:** Images of a healthy volunteer. All three orientations are given in (A)-(C) for the non-contrast-enhanced 3D FLASH sequence. In (D) a MIP of the 3D FLASH shows excellent angiographic visualization of both carotid arteries. A classification of the vessel walls can be obtained from the axial PD- and T2-weighted TSE images in (E) and (F), respectively. Magnifications of the right carotid arteries are provided in (E) and (F).

A side-by-side comparison of different imaging modalities (digital subtraction angiography (DSA), 1.5 T contrast-enhanced MRA, and 7 T non-contrast-enhanced MRA) is given in Fig. 4.8 for the case of the patient with a stenosis of the right internal carotid artery with an ulcerated plaque. Without the administration of contrast agent, 7 T could render the extent of the stenosis as well as the plaque ulceration with the same quality as compared to the other two techniques. As is known for maximum-intensity-projection (MIP) techniques in MRI, the stenosis is overestimated using this technique compared to DSA. However, in the axial source images the lumen in the stenotic region can be well visualized (lower row of Fig. 4.8).

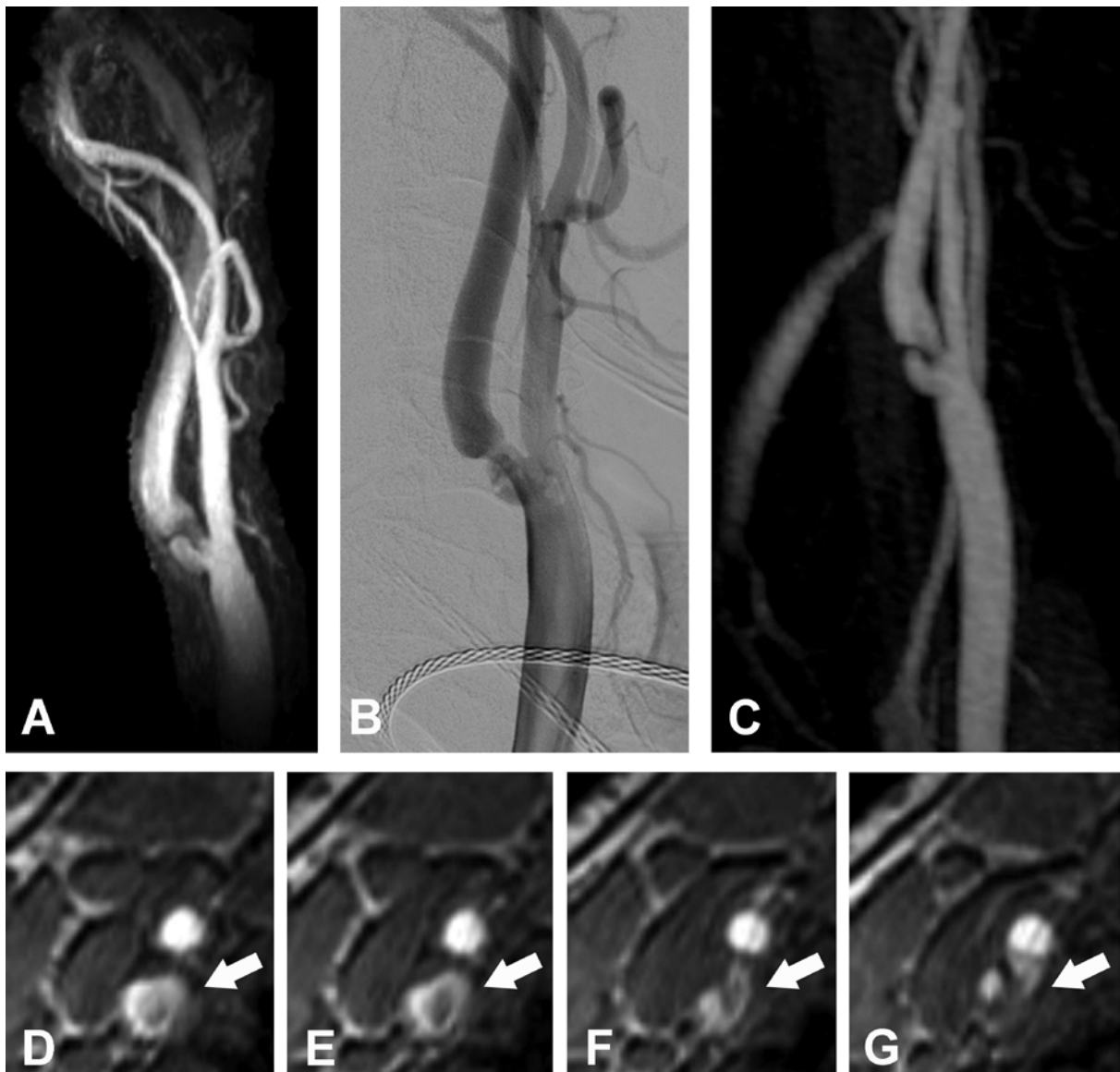


**Fig. 4.8:** Images of a patient with an ulcerated atherotic plaque and 50% stenosis in the right internal carotid artery. Top row (A-C): A MIP of the 7 T non-contrast-enhanced 3D FLASH sequence (A) is compared to the correlating gold standard digital subtraction angiography (DSA) image (B) and MIP of a 1.5 T contrast-enhanced MRA (C). The bottom row (D-G) shows axial 7 T 3D FLASH images of the stenosis and plaque ulceration in the right internal carotid artery (arrows).

For further differentiation of intraplaque compartments, axial 7 T PD- and T2-weighted TSE images were compared to the corresponding computer tomography (CT) angiography image (Fig. 4.9). Axial 7 T images revealed the disruption and ulcer of the plaque as well as the flow of (unenhanced) blood as low T2-signal flow

void through the narrowed lumen, corresponding well to the contrast agent inflow in the respective CT-angiographic section. In addition, in the plaque an area of marked T2-hyperintensity is visible both in the T2- as well as PD-weighted images. One could hypothesize that this reflects the lipid core in the plaque, since the hyperintensity presents a similar signal compared to adjacent adipose tissue, although at present no histological proof is available in this patient, who underwent carotid stenting after MRI.

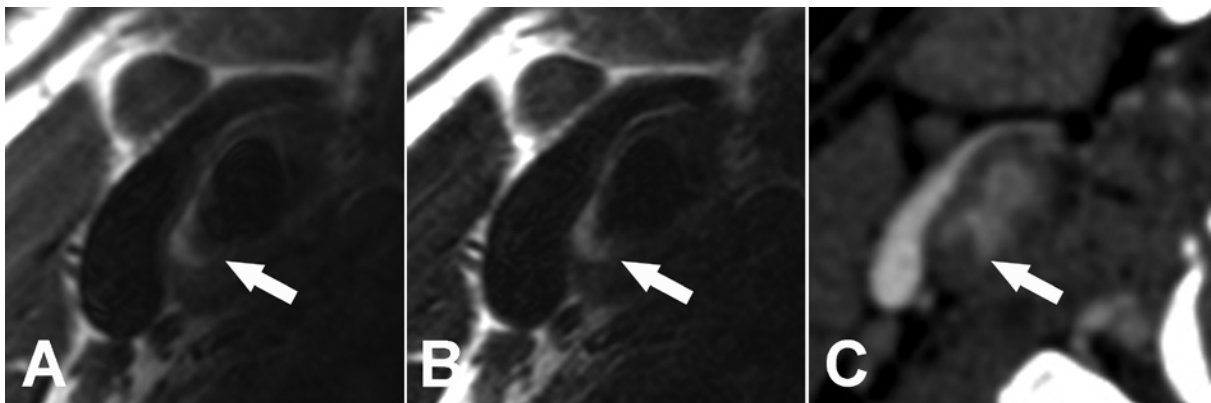


**Fig. 4.9:** Axial 7 T PD- and T2-weighted TSE images (A, B) of the patient are compared to the corresponding CT angiographic image (C). The images show marked wall thickening of the internal carotid artery (arrows).

### 4.3 Discussion

This study demonstrates that the concept of two four-channel transmit/receive RF arrays, one for each side of the neck, can be used for in vivo MR imaging of the carotid arteries at 7 Tesla. High-resolution MRA images of the carotid arteries were shown as well as first experience with cross-sectional high-resolution plaque imaging at 7 T.

The design criteria for this combined transmit/receive RF coil included a rigid geometry rather than a flexible design to maintain a fixed coil element relationship during transmit. The rigid setup, on the other hand, decreased the receive capability of the coil, as the coil elements could not be adapted to different neck shapes, which can vary significantly among the population. Although publications on the analysis of the g-factors of various coil designs have demonstrated that two loops should be slightly separated instead of overlapped to obtain the best g-factors and therefore the best parallel imaging capability<sup>33</sup>, decoupling of this coil was performed geometrically with an optimum overlap of nearest-neighbor coils<sup>22</sup>. An alternative to geometrical decoupling would be to insert either capacitors or inductors between the two coils so that the mutual inductance is canceled<sup>34-37</sup>. However, SAR may be increased around these lumped elements.

The carotid RF coil was developed for future use in upcoming clinical studies, making a fixed-tuned design mandatory. Although an individually-tuned coil might achieve slightly better image quality, a fixed-tuned coil is not only easier to handle by a radiographer and saves time for setup, it is also more robust and more accepted by a patient because of the reduced examination time. Hence, a bottle with similar dimensions as a human neck was filled with tissue-simulating liquid and used for a single tuning and matching procedure. The comparison of S-parameters obtained in this set-up with the coil loaded with a human neck rendered similar results, so that the coil performs relatively insensitively to different loads. Reflection and isolation of the individual elements were found to be sufficient: less than 2% of the input power will be reflected at the port and less than 5% of the transmit power will be coupled into neighboring elements.

Measurements of the g-factors as a function of different acceleration factors rendered adequate image quality that was not compromised by amplified noise and reconstruction artifacts up to an acceleration factor of 2.4 along the head-feet direction (for anterior-posterior only up to  $R = 1.8$ ). Acceleration along the head-feet direction performed slightly better than along anterior-posterior, as expected, since the sensitivities of the coil elements are further disjoint along head-feet.

An intensive compliance test with regards to patient safety is obligatory for a RF transmit coil at 7 T, since SAR scales approximately with the field strength squared and becomes a non-negligible, critical factor for high-field MRI. Thus, the coil model used in the numerical simulations needs to be validated in order to validate the SAR calculations. The presented  $B_1^+$  map comparison indicated a satisfactory coil model (close to reality) for the performed SAR calculations. We assume the worst case error in the E-fields to be of the same order as the difference in the absolute values of  $B_1^+$  fields between measurement and simulation. Additionally, within the limitations of the temperature measurements (being point-wise and having been made at only a few locations), they were in good agreement with the SAR calculations and confirmed the calculated maximum input power level as well as the location of the SAR hot spot. For the numerical simulations, the “Duke” model was chosen because it contains more than twice as many different tissue types compared to the standard “Hugo” dataset<sup>38</sup> (33 different tissue types). Furthermore, the Virtual Family<sup>29</sup> datasets were obtained from an actual MRI experiment, which facilitates an exact and realistic positioning of the coil. Hence, with the validated SAR calculations, a reliable compliance test with 3-dimensional information could be achieved.

The in vivo images revealed that high-resolution MR angiography as well as detailed plaque characterization in patients are feasible at 7 T. Even in the presence of a severely calcified carotid plaque, the differentiation of blood flow in the remnant vessel lumen as well as differentiation of distinct intraplaque components and surface ulcerations were possible without the administration of a contrast agent. This is of particular importance, since especially patients with relevant atherosclerosis commonly have relative or absolute contraindications against the administration of



gadolinium contrast material. Another inherent advantage of 7 T field strength has also been shown in Fig. 4.6, comparing the non-contrast-enhanced sequences 3D TOF at 1.5 T and 3D FLASH at 7 T. At 7 T, 3D FLASH imaging provides strong vascular signal enhancement<sup>8</sup> combined with more vascular detail due to the 3 times higher spatial resolution acquired within half of the acquisition time of the 1.5 T TOF dataset.

For perfectly timed and triggered plaque images, electrocardiogram (ECG) triggering is mandatory<sup>39-40</sup>. At 7 T, however, the ECG signal is corrupted by interferences with the electromagnetic fields of the imager and, in particular, by magneto-hydrodynamic effects<sup>41-42</sup>. Hence, cardiac triggering in this study had to be performed with pulse triggering, which is less exact and leads to residual in-plane vessel wall movement during data acquisition with potential degradation of image sharpness and signal smearing. New, more reliable ECG gating techniques, such as recently introduced acoustic cardiac triggering<sup>43</sup>, might further improve image quality at 7 T.

The results of the present study demonstrate that many of the major RF coil related challenges of 7 T carotid MRI can be successfully addressed. The 2x4-channel transmit/receive carotid RF coil presented in this study provides sufficient SNR for high image resolution and signal penetration depths for assessment of the carotid vessel wall, while the transmit energy levels all stay within the patient safety relevant SAR limits. This study, with a focus on RF coil development and first clinical demonstration, forms the groundwork for further studies with a focus on the imaging protocols and clinical applications in patients with atherosclerosis. Especially for plaque characterization, gradient and spin-echo sequences have to be optimized for soft tissue contrast, SAR, and spatial volume coverage. With RF shimming<sup>44-45</sup> and hence potentially different phase settings between coil elements for each individual patient,  $B_1^+$  may be increased in a defined ROI around the plaque, which may be advantageous especially for the TSE sequence. SAR restrictions, difficulties with the ECG trigger, and high-field related image artifacts have been identified as key challenges of 7 T carotid MRI. Therefore, the known and well established standard imaging contrasts for multicontrast carotid imaging (PD, T1, T2, TOF, and black

blood imaging) at 1.5 T and 3 T<sup>46-50</sup> will have to be adapted for the 7 T imaging regime in order to exploit the full potential of 7 T high-field MRI for atherosclerotic plaque imaging.

## References

1. Heverhagen JT, Bourekas E, Sammet S, Knopp MV, Schmalbrock P. Time-of-flight magnetic resonance angiography at 7 Tesla. *Invest Radiol.* Aug 2008;43(8):568-573.
2. Utting JF, Kozerke S, Luechinger R, et al. Feasibility of k-t BLAST for BOLD fMRI with a spin echo acquisition at 3 Tesla and 7 Tesla. *Invest Radiol.* 2009;44(9):495–502.
3. Krug R, Stehling C, Kelley DA, Majumdar S, Link TM. Imaging of the musculoskeletal system in vivo using ultra-high field magnetic resonance at 7 Tesla. *Invest Radiol.* 2009;44(9):613–618.
4. Kraff O, Bitz AK, Kruszona S, et al. An eight-channel phased array RF coil for spine MR imaging at 7 T. *Invest Radiol.* Nov 2009;44(11):734-740.
5. Snyder CJ, DelaBarre L, Metzger GJ, et al. Initial results of cardiac imaging at 7 Tesla. *Magn Reson Med.* Mar 2009;61(3):517-524.
6. Ladd ME. High-field-strength magnetic resonance: potential and limits. *Top Magn Reson Imaging.* Apr 2007;18(2):139-152.
7. Schenck JF, Zimmerman EA. High-field magnetic resonance imaging of brain iron: birth of a biomarker? *NMR Biomed.* Nov 2004;17(7):433-445.
8. Maderwald S, Ladd SC, Gizewski ER, et al. To TOF or not to TOF: strategies for non-contrast-enhanced intracranial MRA at 7 T. *MAGMA.* Mar 2008;21(1-2):159-167.
9. Kraff O, Maderwald S, Hahn S, et al. In-Vivo Plaque Imaging of the Carotid Arteries at 7 Tesla: First Results. Paper presented at: Proceedings 16th Scientific Meeting, International Society for Magnetic Resonance in Medicine; April, 2008; Toronto.
10. Piccirelli M, DeZanche N, Nordmeyer-Massner J, et al. Carotid Artery Imaging at 7T: SNR Improvements using Anatomically Tailored Surface Coils. Paper presented at: Proceedings 16th Scientific Meeting, International Society for Magnetic Resonance in Medicine; April, 2008; Toronto.
11. Wiggins G, Zhang B, Duan Q, et al. 7 Tesla Transmit-Receive Array for Carotid Imaging: Simulation and Experiment. Paper presented at: Proceedings

- 17th Scientific Meeting, International Society for Magnetic Resonance in Medicine; April, 2009; Honolulu.
12. Van de Moortele PF, Akgun C, Adriany G, et al. B(1) destructive interferences and spatial phase patterns at 7 T with a head transceiver array coil. *Magn Reson Med*. Dec 2005;54(6):1503-1518.
  13. Cury RC, Houser SL, Furie KL, et al. Vulnerable plaque detection by 3.0 tesla magnetic resonance imaging. *Invest Radiol*. Feb 2006;41(2):112-115.
  14. Virmani R, Burke AP, Kolodgie FD, Farb A. Pathology of the thin-cap fibroatheroma: a type of vulnerable plaque. *J Interv Cardiol*. Jun 2003;16(3):267-272.
  15. Yuan C, Kerwin WS, Yarnykh VL, et al. MRI of atherosclerosis in clinical trials. *NMR Biomed*. Oct 2006;19(6):636-654.
  16. Yuan C, Kerwin WS, Ferguson MS, et al. Contrast-enhanced high resolution MRI for atherosclerotic carotid artery tissue characterization. *J Magn Reson Imaging*. Jan 2002;15(1):62-67.
  17. Kwee RM, van Oostenbrugge RJ, Mess WH, et al. Carotid Plaques in Transient Ischemic Attack and Stroke Patients: One-Year Follow-up Study by Magnetic Resonance Imaging. *Invest Radiol*. Sep 8 2010.
  18. Lobbes MB, Heeneman S, Passos VL, et al. Gadofosveset-enhanced magnetic resonance imaging of human carotid atherosclerotic plaques: a proof-of-concept study. *Invest Radiol*. May 2010;45(5):275-281.
  19. Li F, Yarnykh VL, Hatsukami TS, et al. Scan-rescan reproducibility of carotid atherosclerotic plaque morphology and tissue composition measurements using multicontrast MRI at 3T. *J Magn Reson Imaging*. Jan 2010;31(1):168-176.
  20. Raghavan P, Mukherjee S, Gaughen J, Phillips CD. Magnetic resonance angiography of the extracranial carotid system. *Top Magn Reson Imaging*. Oct 2008;19(5):241-249.
  21. Heiserman JE, Dean BL, Hodak JA, et al. Neurologic complications of cerebral angiography. *AJNR Am J Neuroradiol*. Sep 1994;15(8):1401-1407; discussion 1408-1411.

22. Roemer PB, Edelstein WA, Hayes CE, Souza SP, Mueller OM. The NMR phased array. *Magn Reson Med*. Nov 1990;16(2):192-225.
23. Hayes CE, Mathis CM, Yuan C. Surface coil phased arrays for high-resolution imaging of the carotid arteries. *J Magn Reson Imaging*. Jan-Feb 1996;6(1):109-112.
24. Balu N, Yarnykh VL, Scholnick J, Chu B, Yuan C, Hayes C. Improvements in carotid plaque imaging using a new eight-element phased array coil at 3T. *J Magn Reson Imaging*. Sep 24 2009.
25. *CST MICROWAVE STUDIO®*, CST GmbH [computer program]. Version User Manual Version 2009. Darmstadt, Germany.
26. Griswold MA, Jakob PM, Heidemann RM, et al. Generalized autocalibrating partially parallel acquisitions (GRAPPA). *Magn Reson Med*. Jun 2002;47(6):1202-1210.
27. Porter JR, Wright SM, Reykowski A. A 16-element phased-array head coil. *Magn Reson Med*. Aug 1998;40(2):272-279.
28. Firbank MJ, Coulthard A, Harrison RM, Williams ED. A comparison of two methods for measuring the signal to noise ratio on MR images. *Phys Med Biol*. Dec 1999;44(12):N261-264.
29. Christ A, Kainz W, Hahn EG, et al. The Virtual Family--development of surface-based anatomical models of two adults and two children for dosimetric simulations. *Phys Med Biol*. Jan 21 2010;55(2):N23-38.
30. Yarnykh VL. Actual flip-angle imaging in the pulsed steady state: a method for rapid three-dimensional mapping of the transmitted radiofrequency field. *Magn Reson Med*. Jan 2007;57(1):192-200.
31. Vizmuller P. *RF design guide: systems, circuits, and equations* Artech House, Inc.; 1995.
32. International Electrotechnical Commission. Medical electrical equipment - Part 2-33: Particular requirements for the safety of magnetic resonance diagnostic devices. *IEC 60601-2-33*. Vol 2002.

33. Weiger M, Pruessmann KP, Leussler C, Roschmann P, Boesiger P. Specific coil design for SENSE: a six-element cardiac array. *Magn Reson Med*. Mar 2001;45(3):495-504.
34. Duensing GR, Brooker HR, Fitzsimmons JR. Maximizing signal-to-noise ratio in the presence of coil coupling. *J Magn Reson B*. Jun 1996;111(3):230-235.
35. Wang J. A novel method to reduce the signal coupling of surface coils for MRI. *Proceedings of the 4th Annual Meeting of ISMRM*. Vol New York 1996:1434.
36. Lian J, Roemer PB, Inventors. MRI RF Coils. US patent 5,804,969 1998.
37. Nabeshima T, Takahashi T, Matsunaga Y, Yamamoto E, Inventors. RF probe for MRI. US patent 5,489,847 1996.
38. The Visible Human Project, <http://vhp.ntu.edu.sg/>.
39. Yuan C, Mitsumori LM, Beach KW, Maravilla KR. Carotid atherosclerotic plaque: noninvasive MR characterization and identification of vulnerable lesions. *Radiology*. Nov 2001;221(2):285-299.
40. Hinton-Yates DP, Cury RC, Wald LL, et al. 3.0 T plaque imaging. *Top Magn Reson Imaging*. Oct 2007;18(5):389-400.
41. Stuber M, Botnar RM, Fischer SE, et al. Preliminary report on in vivo coronary MRA at 3 Tesla in humans. *Magn Reson Med*. Sep 2002;48(3):425-429.
42. Nijm GM, Swiryn S, Larson AC, Sahakian AV. Extraction of the magnetohydrodynamic blood flow potential from the surface electrocardiogram in magnetic resonance imaging. *Med Biol Eng Comput*. Jul 2008;46(7):729-733.
43. Frauenrath T, Hezel F, Heinrichs U, et al. Feasibility of cardiac gating free of interference with electro-magnetic fields at 1.5 Tesla, 3.0 Tesla and 7.0 Tesla using an MR-stethoscope. *Invest Radiol*. 2009;44(9):539–547.
44. Hoult DI, Phil D. Sensitivity and power deposition in a high-field imaging experiment. *J Magn Reson Imaging*. Jul 2000;12(1):46-67.
45. Ibrahim TS, Lee R, Baertlein BA, Abduljalil AM, Zhu H, Robitaille PM. Effect of RF coil excitation on field inhomogeneity at ultra high fields: a field optimized TEM resonator. *Magn Reson Imaging*. Dec 2001;19(10):1339-1347.

46. Quick HH, Debatin JF, Ladd ME. MR imaging of the vessel wall. *Eur Radiol.* Apr 2002;12(4):889-900.
47. Fayad ZA, Fuster V. Clinical imaging of the high-risk or vulnerable atherosclerotic plaque. *Circ Res.* Aug 17 2001;89(4):305-316.
48. Yarnykh VL, Terashima M, Hayes CE, et al. Multicontrast black-blood MRI of carotid arteries: comparison between 1.5 and 3 tesla magnetic field strengths. *J Magn Reson Imaging.* May 2006;23(5):691-698.
49. Underhill HR, Yarnykh VL, Hatsukami TS, et al. Carotid plaque morphology and composition: initial comparison between 1.5- and 3.0-T magnetic field strengths. *Radiology.* Aug 2008;248(2):550-560.
50. Zhao X, Underhill HR, Yuan C, et al. Minimization of MR contrast weightings for the comprehensive evaluation of carotid atherosclerotic disease. *Invest Radiol.* Jan 2010;45(1):36-41.

# Chapter 5 An Eight-Channel Transmit / Receive Multi-Purpose Coil for Musculoskeletal MR Imaging at 7 T \*

## Abstract

MRI plays a leading diagnostic role in assessing the musculoskeletal (MSK) system and is well established for most questions at clinically-used field strengths (up to 3 T). 7 T MRI of the knee has already received increasing attention in the current published literature, but there is a strong need to develop new radiofrequency (RF) coils to assess more regions of the MSK system. In this work, an eight-channel transmit/receive RF array was built as a multi-purpose coil for imaging some of the thus far neglected regions. An extensive coil characterization protocol and first in vivo results of the human wrist, shoulder, elbow, knee, and ankle imaged at 7 T will be presented. For safety validation, a detailed compliance test was performed including full wave simulations of the RF field distribution and the corresponding specific absorption rate (SAR) for all joints. In vivo images of four volunteers were assessed with gradient echo (GRE) and turbo spin echo sequences (TSE) modified to obtain optimal image contrast, full anatomic coverage, and the highest spatial resolution within a reasonable acquisition time. The performance of the RF coil was additionally evaluated by in vivo B1 mapping.

This study demonstrates that the presented concept can be used as a multi-purpose coil for high-resolution in vivo MR imaging of the MSK system at 7 T. Not only GRE but also typical clinical and SAR intensive sequences such as STIR and TSE performed well. Imaging of cartilage and nerves could in particular benefit from this technique.

\* **Kraff O**, Bitz AK, Dammann P, Ladd SC, Ladd ME, Quick HH. An Eight-Channel Transmit / Receive Multi-Purpose Coil for Musculoskeletal MR Imaging at 7T. *Med Phys.* Dec 2010; 37(12):6368-6376.



## 5.1 Introduction

With its superior tissue contrast and sensitivity to tissue composition, magnetic resonance imaging (MRI) plays a leading diagnostic role in assessing the musculoskeletal (MSK) system and is well established for most questions at clinically-used field strengths (up to 3 T)<sup>1</sup>. Although low-field MR imaging (up to but not including 1.5 T) may be used efficiently in daily clinical practice<sup>2-3</sup>, most musculoskeletal MR examinations are performed at magnetic field strengths of 1.5 T or 3 T<sup>4</sup>. While at 1.5 T most musculoskeletal tissues (cartilage, muscle, tendon, ligaments, bones etc.) exhibit sufficient signal-to-noise ratio (SNR), which is limited by the small field of view (FOV) that is usually utilized, 3 T MRI has recently demonstrated improved imaging quality and speed and provided preliminary evidence for concomitant improvement in diagnostic accuracy<sup>5-6</sup>.

However, there is still a need for further improvement, in particular for small defects and an accurate assessment of cartilage abnormalities, for example<sup>7-8</sup>. Cartilage is one of the most important biomarkers in degenerative and traumatic joint disease. While early recognition of degeneration is important, of course, there is also a pressing need for reliable and objective monitoring in order to evaluate and compare various treatment options in cartilage surgery<sup>9</sup>. Additionally, the in vivo evaluation of peripheral nerves for the differentiation of inflammatory and degenerative changes is limited by SNR and spatial resolution on clinical systems<sup>10</sup>.

The current literature shows increasing evidence that ultra-high field (UHF, 7 T and above) MRI can provide improved diagnostic capabilities compared with MRI performed at standard clinical field strengths<sup>11-17</sup>. Especially 7 T MRI of the knee<sup>11-15, 17-23</sup> has received increasing attention in the published literature, whereas other joints have been addressed less (wrist<sup>11, 14, 16-17, 24-26</sup>, ankle<sup>14, 17</sup>) or not at all (shoulder, elbow). This may be explained by the technical challenges of performing UHF MRI in general: changes in T1 and T2 relaxation times, enhanced susceptibility and chemical shift artifacts, no integrated transmit body coil indicating the necessity for local transmit/receive radiofrequency (RF) coils, the challenges of verifying patient safety with respect to coil placement, and greater RF energy deposition. The effects of electromagnetic wave propagation in tissue leading to destructive interferences

and asymmetric distributions of the excitation RF magnetic field ( $B_1^+$ ) over the imaging sample are already prominent at 3 T. These effects and their associated signal inhomogeneities increase even further with increasing field strength <sup>27</sup>, necessitating numerical simulations for both the design process of a 7 T coil and for subsequent characterization and safety compliance testing.

In this work, an eight-channel transmit/receive (T/R) RF array was built as a multi-purpose coil for imaging some of the thus far neglected musculoskeletal regions. The array was made of four overlapping loop coils per side to enable flexible positioning. First in vivo results of the human shoulder, elbow, wrist, knee, and ankle as well as an extensive characterization of the coil in these body parts will be presented.

## 5.2 Materials and Methods

### *RF Coil Design and Construction*

The multi-purpose coil was developed for a 7 T whole-body MR scanner (Magnetom 7 T, Siemens Healthcare Sector, Erlangen, Germany). Eight square surface loop coils with a dimension of  $6 \times 7 \text{ cm}^2$  each were machined from 0.8-mm-thick FR4 circuit board material (LPKF Laser & Electronics AG, Garbsen, Germany).

Each coil element has 5-mm-wide circuits with a copper-clad layer of  $35 \mu\text{m}$  thickness, and three 2 mm gaps bridged by 8.2 pF non-magnetic capacitors (Voltronics Corporation, Denville, NJ, USA). Common-mode cable current suppression was provided by a cable trap formed by a 6 cm long semi-rigid coaxial cable wound in two turns (5-mm-diameter inductor) in parallel with a variable capacitor (2.5-10 pF, Murata Manufacturing Co., Ltd., Kyoto, Japan). The cable trap was tuned to approximately 297 MHz and placed directly at each coil element (Fig. 5.1).

To facilitate easy positioning on different joints, two coil clusters, each with four loop elements, were combined to form one RF transmit/receive array. An overlapped and shifted arrangement of the coil elements was chosen to reduce the mutual inductance between neighboring and next-nearest-neighbor coils<sup>28</sup> as shown in Fig. 5.1. The elements were fed with opposite polarity between the two coil rows to provide a  $180^\circ$  phase shift. Hence, the currents of both rows pointed in the same direction along the centerline loop paths to increase the  $B_1^+$  amplitude in the region of interest. The phase shift was implemented directly on the coil elements by inverting the drive polarity.

Despite a very intensive safety assessment of the T/R RF coil described below, which ensured a safe usage for in vivo measurements, additional attention was given to the cabling (as known from commercially available RF coils). Since the loop elements were not shielded, the cables (2.5 times wavelength in length) were led directly away from the elements (Fig. 5.1). This minimized the risk of common-mode currents, as the cables were routed away from the local transmit fields. The length of the cables was chosen to be sufficient for positioning on various joints, and

care was taken to maintain a suitable distance (filled with pads) between patient and cable. The elements were then connected to a box with eight circuit boards containing T/R switches and preamplifiers (Stark Contrast, Erlangen, Germany). The transmit paths of the T/R switch box were connected to the individual output ports of an 8 x 1kW RF power amplifier (Dressler, Stolberg, Germany).

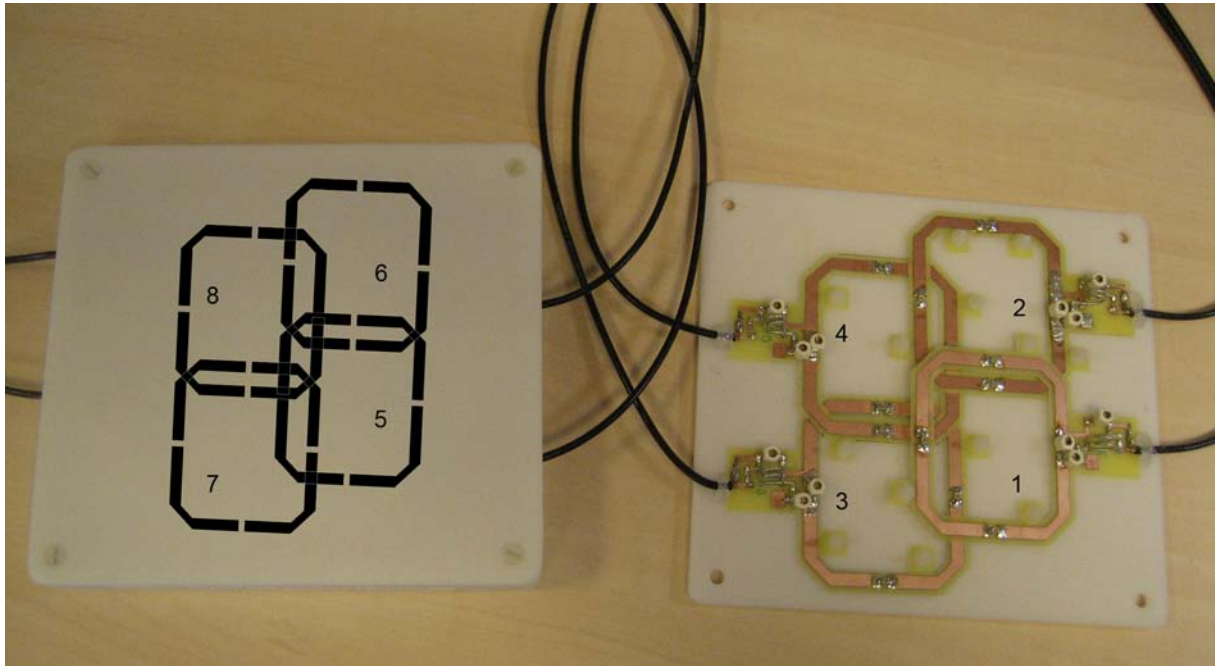


**Fig. 5.1:** Photograph of the multi-purpose RF coil. Each coil cluster is made of 4 geometrically overlapping RF transmit/receive loop coil elements. The coil row of Elements 1 and 2 (5 and 6, respectively) was shifted by 2.1 cm with respect to the row of Elements 3 and 4 (7 and 8, respectively) to reduce the mutual inductance between next-nearest-neighboring elements. The numbering gives the element numbers used in the text for the two coil clusters.

The elements were each matched to 50 Ohms at 297 MHz. Tuning and matching were optimized on the bench with a nearly square cylindrical bottle phantom ( $22.0 \times 13.5 \times 13.5 \text{ cm}^3$ ) filled with body-simulating liquid ( $\epsilon_r = 43$ ,  $\sigma = 0.8 \text{ Sm}^{-1}$ ) and assessed with a network analyzer (Agilent E5061A, Santa Clara, CA, USA). S-parameters were determined in the loaded condition with the bottle phantom. Additionally, it was verified that touching the cables had no effect on the resonance peak; sensitivity to cable handling could be a hint for common-mode

currents or an ineffective cable trap. Afterwards, the S-parameters were verified on a human wrist, elbow, and shoulder.

## *Phantom Study*

To acquire data for g-factor maps, two fully sampled datasets of the phantom used for tuning and matching were obtained with a spin echo sequence with TR/TE = 500/25 ms, 180° flip angle, 0.7 x 0.7 x 5.0 mm<sup>3</sup> resolution, and matrix 384 x 384. Undersampled datasets were generated by omitting phase encoding lines using the OpenGRAPPA algorithm<sup>29</sup> with effective acceleration factors of R = 1.8, 2.4, and 2.9 (using 48 reference lines<sup>30</sup>). Estimates of the SNR were made with the difference method<sup>31</sup>. By subtracting the two images, a noise image was generated; the signal was determined in the sum image of the two images. Finally, g-factor maps were calculated pixelwise by the following equation:  $g\text{-factor} = \text{SNR}^{\text{full}} / (\text{SNR}^{\text{accel.}} * \sqrt{R})$ .

A noise correlation matrix was calculated out of uncombined single-channel images using a turbo fast low-angle shot (TurboFLASH) sequence without RF pulses.

Additionally,  $B_1^+$  maps were acquired to validate the numerical model of the coil used in the finite difference time domain (FDTD) simulations (next section). Both the qualitative pattern of the  $B_1^+$  field in defined sagittal planes (1, 2, and 3 cm within the phantom; on the left and right sides) as well as the quantitative maximum  $B_1^+$  value in the measured  $B_1^+$  maps were compared with simulated  $B_1^+$  maps. Experimental  $B_1^+$  maps utilized the actual flip angle imaging (AFI) sequence<sup>32</sup> with the following parameters: TR<sub>1</sub> = 20 ms, TR<sub>2</sub> = 100 ms, TE = 2.04 ms, 250 μs square pulse with an amplitude of 100 V, matrix 64 x 64, resolution 3.0 mm isotropic.

To further verify that only one cable trap per element was sufficient despite the rather long cables, gradient and spin echo images were obtained in a special setup: One of the two coil clusters was placed under a large phantom (35 cm x 22 cm x 15 cm), so that the cables could be routed along the phantom. Since common-mode currents have an effect on image homogeneity<sup>33</sup>, the cables should then be visible in images acquired with a large 500 mm field-of-view covering the whole phantom if such currents are present.

## *FDTD simulations*

For safety validation, numerical computations<sup>34</sup> of the RF field distribution were performed on a homogeneous phantom (same size and electrical properties as the phantom used in the phantom study) as well as on a heterogeneous body model. The male member “Duke” of the Virtual Family<sup>35</sup> (70 kg weight, 1.74 m height, including more than 80 different tissue types) was chosen for computations of the RF field and of the corresponding SAR for all joints: shoulder, elbow, wrist, knee, and ankle. The tissue resolution of the voxel model was 1 or 2 mm edge length depending on the anatomical region. The multi-purpose coil was modeled using the exact dimensions of the physical coil including the complete cover of the coil made of 2-mm-thick Makrolon (Bayer Material Science AG, Leverkusen, Germany), which was used for housing the coil. The cable traps, however, were not included in the model, since their inclusion would have otherwise resulted in the need for significantly higher computing power. The coil elements were located 7 mm (2 mm housing plus 5-mm-thick neoprene matting) from the joint surface of the human body model. To take asymmetric loading next to, for example, curved joints into account, coil positioning and alignment and a realistic posture of the body model analogous to the real imaging case were used. In the simulation, the elements were excited individually with 0.5 W time-averaged RF power and were subsequently vectorially combined. The calculations were performed in free space over 5 to 30 million grid points depending on the anatomical region.

## In Vivo Study

In vivo studies were approved by the institutional review board and were performed with signed consent. Four healthy volunteers were included: a 27-year-old female (60 kg, 1.67 m; shoulder), a 30-year-old male (82 kg, 1.87 m; elbow), a 32-year-old male (88 kg, 1.86 m; wrist with known ganglion, knee, ankle), and a 50-year-old female (86 kg, 1.78 m; ankle). For MRI of the wrist and elbow the subjects were scanned in the head-first prone position with the joint extended in front of them, while the supine position was chosen for imaging the shoulder (head-first) and the knee and ankle (feet-first). The two coil clusters were placed as a “sandwich” on top and below the individual joints and fixated with a strip of Velcro® tape.

A set of different sequences was used to test the coil on the different joints: (1) clinical gradient and spin echo sequences such as 2D multi-echo data image combination (MEDIC), 3D double-echo steady state (DESS) with and without water excitation, 2D short tau inversion recovery (STIR), and 2D PD/T2-weighted turbo spin echo (TSE); and (2) actual flip angle imaging (AFI) to map the  $B_1^+$  field in vivo. The sequence parameters are summarized in Tab. 5.1. The  $B_1^+$  maps were normalized to the accepted peak power and, together with the flip angle distribution, compared with corresponding anatomical images (MEDIC).

	TR [ms]	TE [ms]	slices	alpha [deg]	matrix	voxel size [mm <sup>3</sup> ]	TA [min:sec]
<b>MEDIC</b>	1000	15	39	30	512x512	0.4x0.4x1.5	5:33
<b>3D-DESS</b>	11	4	128	15	512x512	0.4x0.4x1.5	6:15
<b>STIR</b>	5000	35	9	120	256x256	0.6x0.6x3.0	1:37
<b>PD/T2 TSE</b>	4350	34/91	15	180	512x512	0.4x0.4x2.0	3:26
<b>AFI</b>	120	2	64	45	64x64	3.0x3.0x5.0	8:12

**Tab. 5.1:** Sequence parameters. For the STIR sequence, an inversion time of 250 ms was selected. A rectangular pulse of 250  $\mu$ s length was used for the AFI sequence at two different TR's of 20 ms and 100 ms. Given is the non-interpolated voxel size.

## 5.3 Results

### *Phantom Study*

Measured reflection and coupling between neighboring elements of the coil loaded with the phantom were  $S_{11} = -16$  dB and  $S_{12} = -17$  dB, respectively. Similar values were found for the verification on the human wrist and slightly better values of around -20 dB were found with the elbow and shoulder load. In the numerical simulations, similar S-parameters ( $S_{11} = -20$  dB,  $S_{12} = -12$  dB) were found compared to the bench measurements.

Coronal and axial g-factor maps are given in Fig. 5.2 for effective acceleration factors of 1.8, 2.4, and 2.9 with phase-encoding directions along head-feet (HF) or anterior-posterior (AP). Mean g-factors were 1.25, 1.36, and 1.73 for the coronal maps (HF) and 1.05, 1.32, and 1.65 for the axial maps (AP).

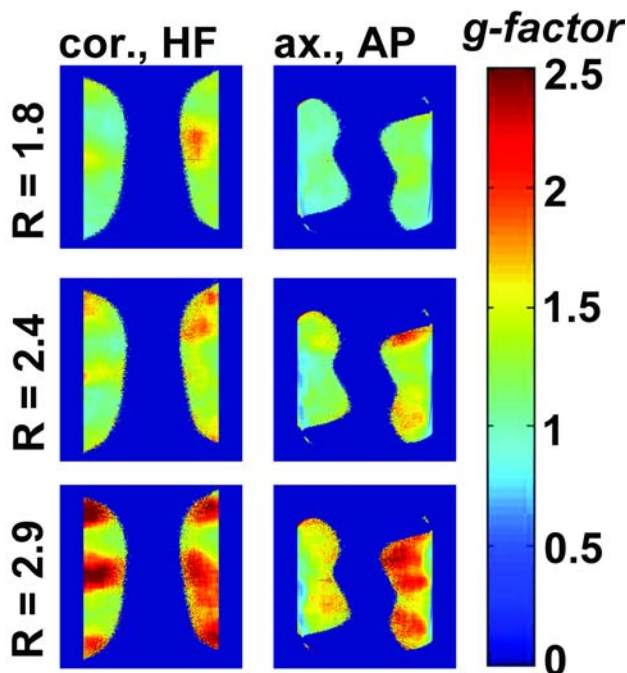


*Fig. 5.2: GRAPPA g-factor maps of the 2x4-channel multi-purpose RF coil acquired in a bottle phantom. The g-factor maps show the spatially variant noise distribution of the coil in two orientations (coronal with the phase-encoding direction in head-feet (HF), and axial with the phase-encoding direction in anterior-posterior (AP)) as a function of increasing effective acceleration factor ( $R=1.8$ ;  $R=2.4$ ;  $R=2.9$ ). Orange/red colors indicate areas with amplified noise which may diminish image quality.*

Noise correlation was found to be better than -18.7 dB on average between neighboring elements, which is shown in Fig. 5.3. Coil pairs that were overlapped and shifted showed lowest noise correlation, while those pairs that were not shifted (e.g. Elements 1 and 2) showed highest correlation values (-11 dB maximum).



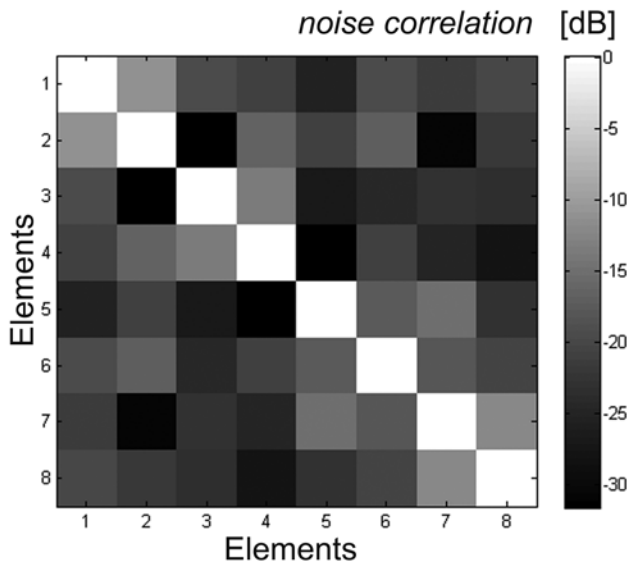


**Fig. 5.3:** Noise correlation matrix (left: measured, right: calculated from simulation). Self-correlation of the elements along the diagonal of the matrix has been normalized to 0 dB. The average noise coupling between individual elements in the coil remained low, with a mean coupling of -18.7 dB for the measurement.

For the safety assessment, the performance of the cable traps was evaluated in a phantom measurement. Even with extreme windowing in the large field-of-view gradient and spin echo images (Fig. 5.4), no effects of the long cables were visible. A comparison between the measured and the simulated  $B_1^+$  distribution is shown qualitatively in Fig. 5.5 for three defined planes on the right side of the phantom. A similar  $B_1^+$  distribution was found between measurement and simulation for both the right and left side, which is also reflected in Tab. 5.2 which gives absolute values of maximum  $B_1^+$ . Here, a difference of less than 7% was found between measurement and simulation.

### *FDTD Simulations*

The maximum permitted input power levels (accepted power, i.e. forward minus reflected) for compliance with the IEC guidelines<sup>36</sup> of 20 W/kg for 10 g-averaged local SAR are shown in Tab. 5.3 for all extremities. In Fig. 5.6, the SAR distributions are provided in two orientations for each joint. The most critical aspect for all joints was the localized SAR (10 g-averaged), and locations of highest RF deposition were close to the coil clusters, i.e. in the skin and subcutaneous fat. For imaging the shoulder and elbow, no significant exposure of the head could be observed.

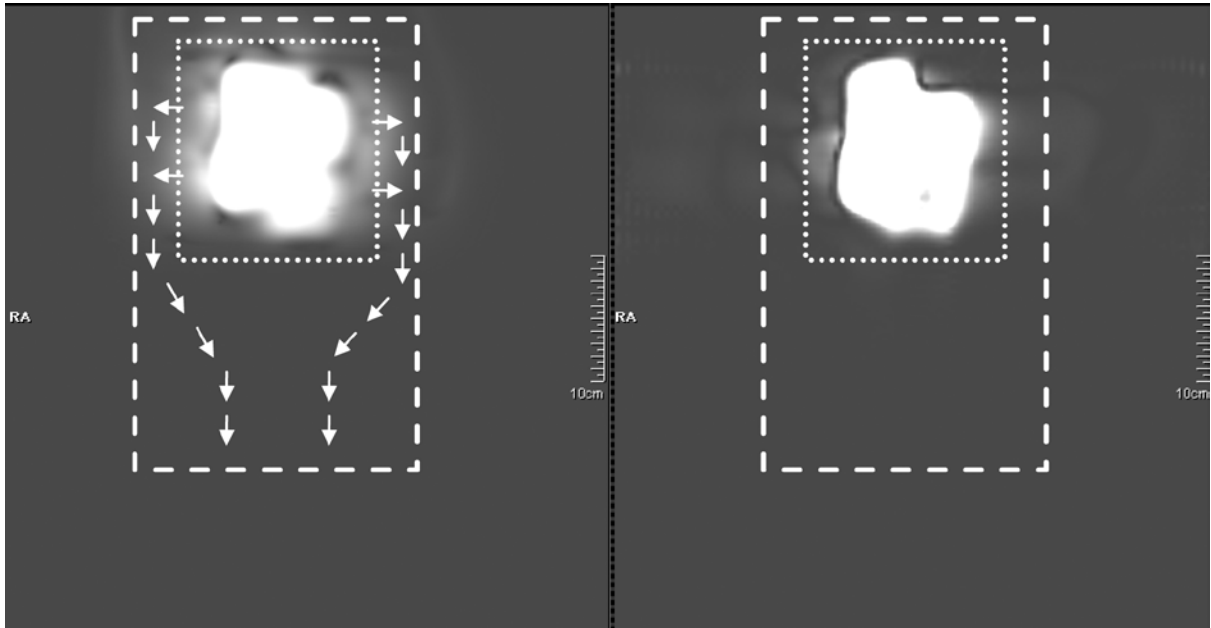


**Fig. 5.4:** Validation of the cable traps. Shown are 500 mm field-of-view images obtained with gradient (left) and spin echo images (right). The dashed line indicates the dimension of the phantom with one coil array placed under its upper half (dotted line), while the arrows show the routing of the cables along the lower half of the phantom. No effects on signal homogeneity and hence common-mode currents were visible.

Slice position	Measurement max. $B_1^+$ [ $\mu\text{T}$ ]	Simulation max. $B_1^+$ [ $\mu\text{T}$ ]	Difference [%]
right, 1 cm	17.1	17.8	4.1
right, 2 cm	11.6	12.0	3.4
right, 3 cm	8.1	8.6	6.2
left, 1 cm	15.5	16.3	5.2
left, 2 cm	10.5	11.2	6.7
left, 3 cm	7.8	8.2	5.1

**Tab. 5.2:** Comparison of absolute values of  $B_1^+$  between measurement and FDTD simulation for validation of the coil model. Given are the values for maximum  $B_1^+$  at defined planes on both sides (i.e., for each coil cluster) within the phantom.

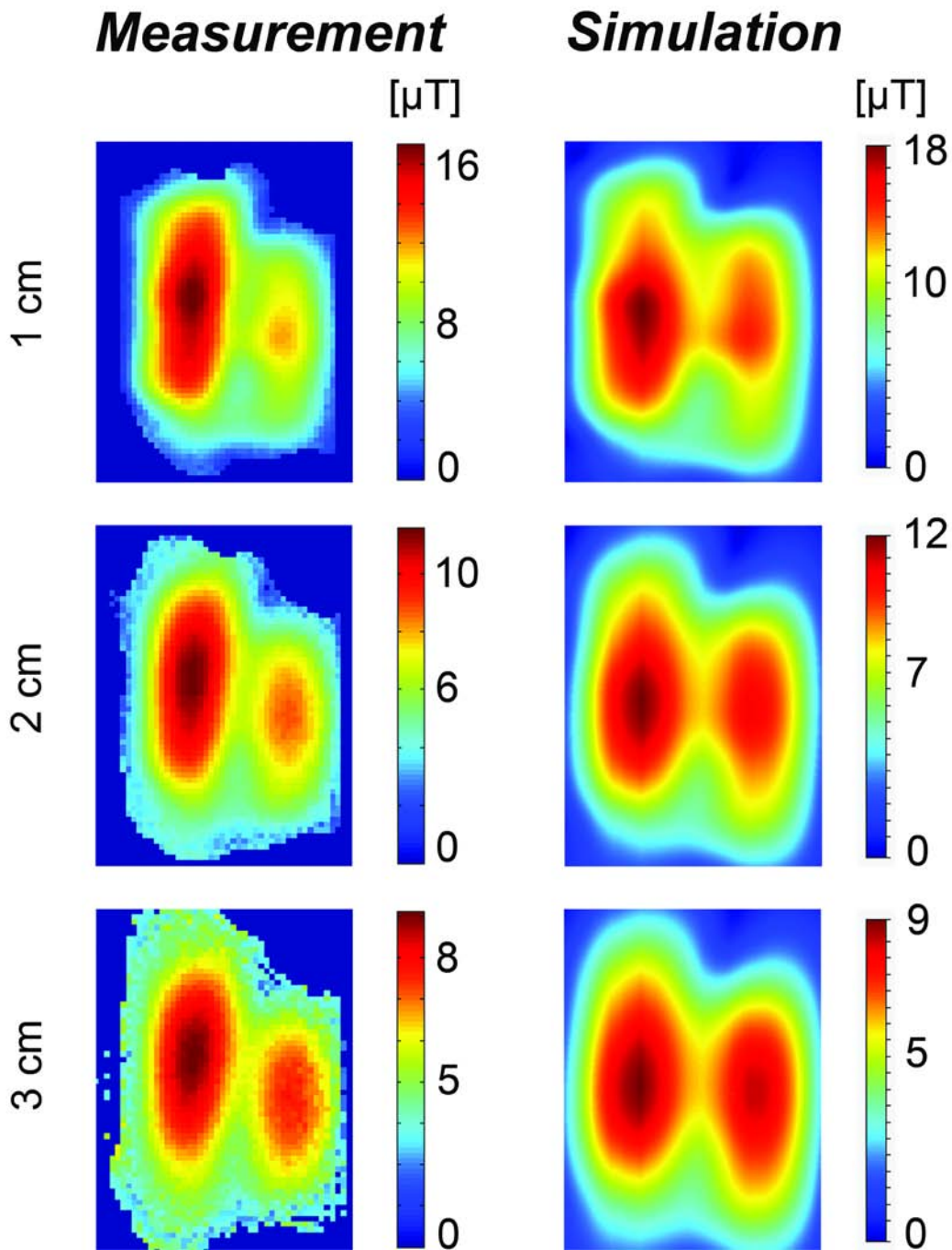


**Fig. 5.5:** To validate the coil model used in the numerical simulation, measured  $B_1^+$  maps (left) were compared with simulated  $B_1^+$  maps (right) regarding field distribution and maximum  $B_1^+$  values for three sagittal planes 1 cm (upper row), 2 cm (middle row), and 3 cm (lower row) inside the phantom. The planes are shown exemplarily for one side only.

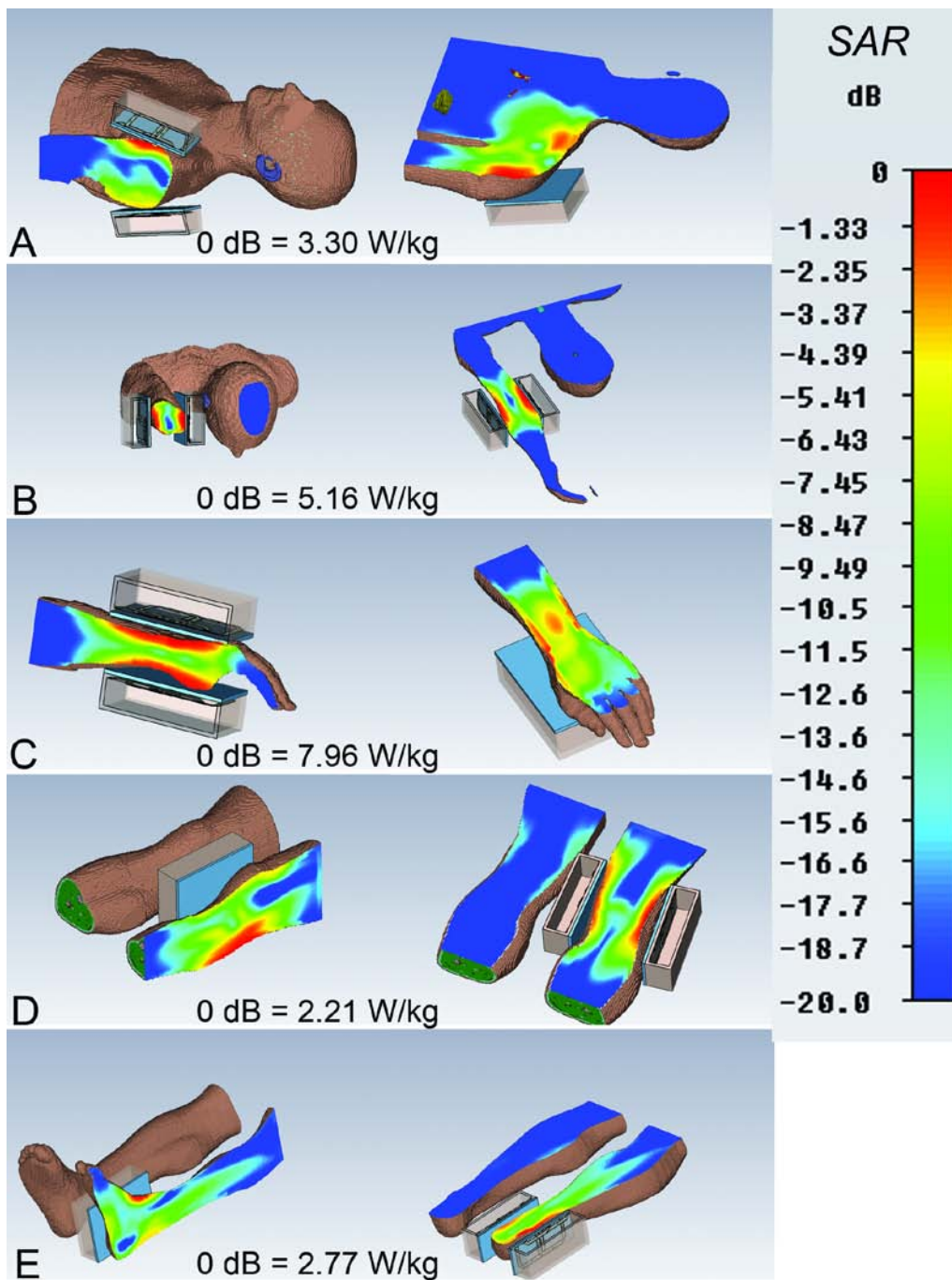


**Fig. 5.6:** For each joint the localized SAR (10 g-averaged) has been calculated using the Virtual Family human body model “Duke”. Care was taken to align the coil model to the anatomy similar to the real imaging case as well as to include the posture of the patient (in B, for example). The SAR distribution in two orientations is shown in each case. For scaling, the reference point of 0 dB is given in W/kg in the images.

Anatomy	$P_{in}$ [W]
Shoulder	6.0
Elbow	3.9
Wrist	2.5
Knee	9.0
Ankle	7.2

**Tab. 5.3:** Maximum permitted input power (time-averaged)  $P_{in}$  in Watts calculated from numerical simulations for different joints for which the localized (10 g-averaged) SAR complies with the limit of 20 W/kg given in the safety guidelines. Given is the total RF power at the coil plug, which is equally split to all coil elements.

### *In Vivo Study*

The multi-purpose coil was tested in vivo for imaging various joints. To judge the performance of the RF coil for this variability of applications, maps of the  $B_1^+$  field as well as the corresponding flip angle distribution were acquired in vivo and compared to anatomic MEDIC images (Fig. 5.7). The highest mean values of  $B_1^+$  per unit peak power were measured for the smaller joints: wrist ( $1.58 \pm 0.19 \mu\text{T}/\sqrt{\text{W}}$ ), ankle ( $1.02 \pm 0.21 \mu\text{T}/\sqrt{\text{W}}$ ), and elbow ( $0.85 \pm 0.11 \mu\text{T}/\sqrt{\text{W}}$ ), while the larger joints rendered slightly lower values: knee ( $0.76 \pm 0.20 \mu\text{T}/\sqrt{\text{W}}$ ) and shoulder ( $0.70 \pm 0.20 \mu\text{T}/\sqrt{\text{W}}$ ). Similarly, in the wrist the flip angle distribution was much more homogeneous while a strong drop-off was found in the center of the knee. The anatomical images correspond very well with the maps with regards to homogeneity and penetration depth.

Using typical clinical sequences, the shoulder joint could be imaged in vivo with full coverage with a 3D-DESS sequence with  $0.35 \times 0.35 \times 1.5 \text{ mm}^3$  resolution (Fig. 5.8A) revealing a good excitation over a 180 mm field-of-view in 6:15 min. Fine anatomic details such as labrum and cartilage could be depicted. In Fig. 5.8B and 8C, MEDIC and PD-weighted TSE images of the elbow joint are shown. Due to the high spatial resolution, fascicles of the median nerve could be rendered clearly (Fig. 5.8B), which is also shown in the axial wrist image in Fig. 5.8D. In a coronal orientation (Fig. 5.8E), branching of the median nerve bundles could be depicted with great detail using a DESS sequence with water excitation. Also note the good suppression of osseous fat in the image. A ganglion appears hyperintense in the T2-weighted STIR image of a wrist (Fig. 5.8F). Additionally, MRI of the ankle performed

very well as shown in the PD-weighted TSE image (Fig. 5.8G), rendering excellent contrast between peritendineal hyperintense fluid and tendon.

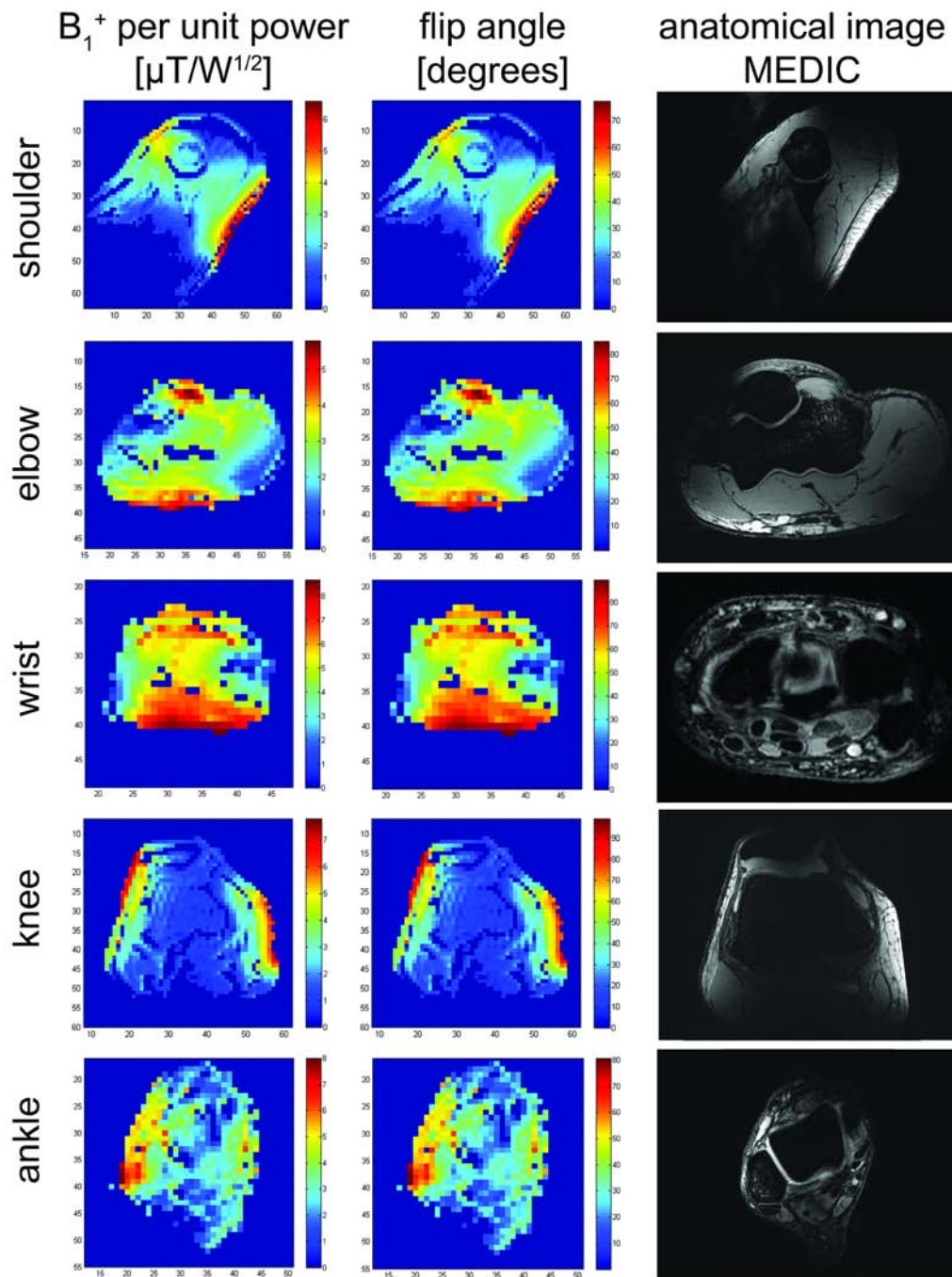


**Fig. 5.7:** For each joint, flip angle distribution (left column, left scale),  $B_1^+$  per unit peak power (left column, right scale), and anatomic MEDIC image (right column) were compared. Maximum  $B_1^+$  per unit power values were  $2.3 \mu\text{T}/\sqrt{\text{W}}$  (shoulder),  $2.0 \mu\text{T}/\sqrt{\text{W}}$  (elbow),  $3.0 \mu\text{T}/\sqrt{\text{W}}$  (wrist),  $2.7 \mu\text{T}/\sqrt{\text{W}}$  (knee), and  $2.8 \mu\text{T}/\sqrt{\text{W}}$  (ankle).



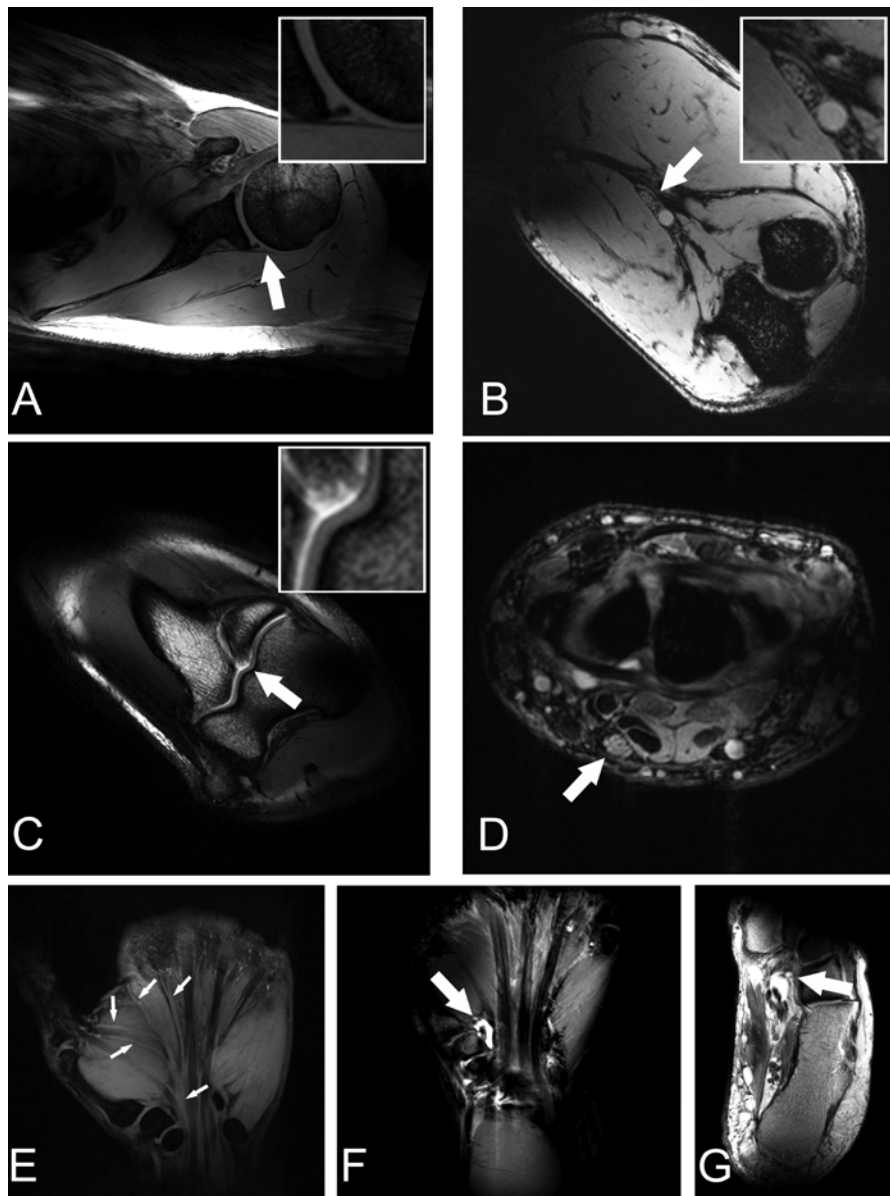


**Fig. 5.8:** *In vivo* images. In (A) a DESS image of the shoulder joint is given, rendering fine anatomic details such as cartilage and labrum (arrow, magnification). Fascicles of the median nerve (arrows) are shown in the MEDIC images of the elbow (B, and magnification) and wrist (D), while the branching of median nerve bundles (arrows) can be appreciated in the coronal DESS image in (E). In (C), a PD-weighted TSE image of the elbow reflects the potential for cartilage imaging (arrow, magnification). A ganglion appears hyperintense in the coronal STIR image of a wrist (F, arrow). An axial, PD-weighted TSE image of an ankle renders excellent contrast between peritendineal hyperintense fluid and tendon (G, arrow).



## 5.4 Discussion

An eight-channel multi-purpose RF coil for high-resolution in vivo MR imaging of the musculoskeletal system at 7 T has been developed and successfully tested. The design of two coil clusters allowed easy positioning of the RF coil for imaging various joints. Although an individually-tuned coil might achieve slightly better image quality, a fixed-tuned design was chosen since it is not only easier to handle by a radiographer and saves time for setup, but it is also more robust and more acceptable to a patient because of the reduced examination time.

The presented RF coil was connected to an 8 x 1 kW RF power amplifier via an add-on RF shimming system<sup>37</sup> and a multi-channel SAR prediction and online monitoring system<sup>38</sup>, which also allows the user to perform multi-element transmit applications, such as Transmit SENSE<sup>39-40</sup> or RF shimming<sup>41-42</sup> with this coil. However, if the coil is used with the described 180° phase shift only, power splitters can be integrated into the transmit path, which would allow the use of a standard combined transmit line from an RF power amplifier as well as the integrated SAR supervision of the MR system. Further optimization of the coil's performance with regard to SAR or  $B_1^+$  homogeneity in a certain region of interest might be achievable with RF shimming. However, this has not been shown in this work, since with the fixed phase settings described here, which were found to be well-suited for general imaging of the joints, the RF coil is principally transferable to any 7T MR system.

A bottle was filled with tissue-simulating liquid and used for a single tuning and matching procedure. The comparison of S-parameters obtained in this set-up with the coil loaded with a human wrist rendered similar results, and only slightly different results were obtained with larger loads such as elbow and shoulder joints, indicating that the coil is relatively insensitive to different loads. Reflection and isolation of the individual elements were found to be sufficient: less than 3% of the input power will be reflected at the port and less than 2% of the transmit power will be coupled into neighboring elements.

Measurements of the g-factors as a function of different acceleration factors rendered adequate image quality that was not compromised by amplified noise and reconstruction artifacts for an acceleration factor of 1.8 along the anterior-posterior

direction. The performance of the RF coil for parallel imaging is determined largely by the arrangement of elements, i.e., the geometrical overlap. Due to the shift between the two coil rows, the sensitivities of the coil elements are further disjoint along the anterior-posterior direction, resulting in a lower g-factor compared to measurements with phase encoding along head-feet. Other techniques for decoupling by inserting capacitors or inductors between neighboring coils <sup>43-46</sup> may be more advantageous for parallel imaging <sup>47</sup>. However, SAR may be increased around these lumped elements, so that this design strategy was not chosen for the combined transmit/receive multi-purpose coil.

SAR scales approximately with the  $B_0$  field strength squared and becomes a non-negligible, critical factor for high-field MRI. Hence, an intensive compliance test with regard to patient safety is obligatory for a RF transmit coil at 7 T. First, the coil model used in the numerical simulations needs to be validated in order to validate the SAR calculations. Since the cables showed no effect on the image homogeneity in large FOV images, the cable traps could be safely omitted from the simulation. A very good match between measurement and simulation over different positions within a phantom indicated a satisfactory coil model (close to reality both qualitatively and quantitatively) for the performed SAR calculations. The absolute values from the simulation were systematically higher than the measured values (Tab. 5.2), which can be explained with coil losses, for example at capacitors or connectors, which were not accounted for in the simulation; this overestimation provides an additional, albeit minor, safety margin. For the numerical simulations, a member of the Virtual Family <sup>35</sup> was chosen, since these datasets were obtained from an actual MRI experiment, which facilitates an exact and realistic positioning of the coil as well as adaption of the posture of the body model. This is of critical importance, as asymmetric loading of the elements can have an effect on the SAR distribution. Furthermore, the human body model was modified so that the arm was outstretched over the head and possible effects of the unshielded coil on the head could be detected. No exposure of the head was visible in Fig. 5.6B, which would have otherwise resulted in only 10 W/kg 10 g-averaged-SAR for compliance with the IEC guidelines <sup>36</sup>. Hence, with the presented compliance test, reliable 3-dimensional

information could be obtained. However, further safety considerations include attention to deviation of the coil drive compared to the simulation or a failure of elements which could lead to dangerous SAR focusing <sup>48</sup>. These concerns were addressed by implementing the described phase shift between the elements directly on the elements as well as with a multi-channel SAR supervision and monitoring software <sup>38</sup>.

The performance of the multi-purpose coil was evaluated in vivo. The quantitative  $B_1^+$  measurements yielded high  $B_1^+$  values per unit peak power and a fairly homogeneous excitation for smaller joints (wrist, ankle, and elbow) where the two coil clusters were closest to each other. For larger joints, shoulder and especially knee, where the coil clusters were farther apart, a stronger  $B_1^+$  and hence flip angle variation was observed, which reflects the limits in the penetration depth and transmit field of view of this RF coil. However, for the shoulder, most of the joint could be imaged with adequate quality. Given a typical pulse length of 2 ms, 3  $\mu$ T are needed for a 90° excitation. This  $B_1^+$  amplitude could be achieved for all joints at the location of maximum  $B_1^+$  with 1-2 W peak power, whereas to raise the mean  $B_1^+$  to 3  $\mu$ T, 4-16 W peak power were needed. Qualitatively, overall good image quality could be obtained with the multi-purpose coil, as shown in Fig. 5.8. Not only gradient echo but also typical clinical and SAR-intensive sequences such as STIR and TSE, which are most challenging at 7 T <sup>15, 23</sup>, performed well. Imaging of small structures (labrum) and peripheral nerves could be demonstrated, which reflects the high spatial resolution as well as high tissue contrast and, hence, potential for further clinical studies.

In a recent study, Chang et al. <sup>16</sup> presented high-resolution imaging of the wrist with a self-developed RF coil <sup>49</sup>. The coil was also made of loop elements, but the design differs from the coil presented here since the transmit and receive paths were separate: four transmit channels, driven in a CP<sup>+</sup> mode, and eight receive channels, with all electronics (power splitters, preamplifiers, etc.) placed directly at the coil resulting in a rather bulky housing. Furthermore, they chose a coil geometry in which the wrist can be placed between two curved “clamshell” sections, which could be advantageous for a more homogeneous transmit field in this joint but restricts

application to other joints. Chang et al. presented a thorough investigation of the coil performance regarding parallel acceleration and its effect on contrast-to-noise ratio and image quality. The coil performance with regard to the g-factor was similar to the coil concept presented here.

In conclusion, a multi-purpose RF coil for MRI of the musculoskeletal system at 7 T has been presented, which, to our knowledge, allows for the first time high-resolution imaging of all major joints, especially of the thus far neglected elbow and shoulder joints. The performance of the RF coil was demonstrated with an extensive coil characterization protocol as well as with in vivo images. To exploit the full potential of 7 T high field MRI for musculoskeletal imaging and determine its clinical impact, further studies will of course need to be performed.

## References

1. Kuo R, Panchal M, Tanenbaum L, Crues JV, 3rd. 3.0 Tesla imaging of the musculoskeletal system. *J Magn Reson Imaging*. Feb 2007;25(2):245-261.
2. Taouli B, Zaim S, Peterfy CG, et al. Rheumatoid arthritis of the hand and wrist: comparison of three imaging techniques. *AJR Am J Roentgenol*. Apr 2004;182(4):937-943.
3. Savnik A, Malmskov H, Thomsen HS, et al. MRI of the arthritic small joints: comparison of extremity MRI (0.2 T) vs high-field MRI (1.5 T). *Eur Radiol*. 2001;11(6):1030-1038.
4. Bolog N, Nanz D, Weishaupt D. Muskuloskeletal MR imaging at 3.0 T: current status and future perspectives. *Eur Radiol*. Jun 2006;16(6):1298-1307.
5. Saupe N, Prussmann KP, Luechinger R, Bosiger P, Marincek B, Weishaupt D. MR imaging of the wrist: comparison between 1.5- and 3-T MR imaging--preliminary experience. *Radiology*. Jan 2005;234(1):256-264.
6. Gold GE, Suh B, Sawyer-Glover A, Beaulieu C. Musculoskeletal MRI at 3.0 T: initial clinical experience. *AJR Am J Roentgenol*. Nov 2004;183(5):1479-1486.
7. Kneeland JB, Reddy R. Frontiers in musculoskeletal MRI: articular cartilage. *J Magn Reson Imaging*. Feb 2007;25(2):339-344.
8. Link TM, Stahl R, Woertler K. Cartilage imaging: motivation, techniques, current and future significance. *Eur Radiol*. May 2007;17(5):1135-1146.
9. Trattinig S, Domayer S, Welsch GW, Mosher T, Eckstein F. MR imaging of cartilage and its repair in the knee--a review. *Eur Radiol*. Jul 2009;19(7):1582-1594.
10. Heddings A, Bilgen M, Nudo R, Toby B, McIff T, Brooks W. High-resolution magnetic resonance imaging of the human median nerve. *Neurorehabil Neural Repair*. Jun 2004;18(2):80-87.
11. Krug R, Stehling C, Kelley DA, Majumdar S, Link TM. Imaging of the musculoskeletal system in vivo using ultra-high field magnetic resonance at 7 Tesla. *Invest Radiol*. 2009;44(9):613-618.

12. Welsch GH, Mamisch TC, Hughes T, et al. In vivo biochemical 7.0 Tesla magnetic resonance: preliminary results of dGEMRIC, zonal T2, and T2\* mapping of articular cartilage. *Invest Radiol*. Sep 2008;43(9):619-626.
13. Pakin SK, Cavalcanti C, La Rocca R, Schweitzer ME, Regatte RR. Ultra-high-field MRI of knee joint at 7.0T: preliminary experience. *Acad Radiol*. Sep 2006;13(9):1135-1142.
14. Regatte RR, Schweitzer ME. Ultra-high-field MRI of the musculoskeletal system at 7.0T. *J Magn Reson Imaging*. Feb 2007;25(2):262-269.
15. Kraff O, Theysohn JM, Maderwald S, et al. MRI of the knee at 7.0 Tesla. *Rofo*. Dec 2007;179(12):1231-1235.
16. Chang G, Friedrich KM, Wang L, et al. MRI of the wrist at 7 tesla using an eight-channel array coil combined with parallel imaging: preliminary results. *J Magn Reson Imaging*. Mar 2010;31(3):740-746.
17. Banerjee S, Krug R, Carballido-Gamio J, et al. Rapid in vivo musculoskeletal MR with parallel imaging at 7T. *Magn Reson Med*. Mar 2008;59(3):655-660.
18. Regatte RR, Schweitzer ME. Novel contrast mechanisms at 3 Tesla and 7 Tesla. *Semin Musculoskelet Radiol*. Sep 2008;12(3):266-280.
19. Wang L, Wu Y, Chang G, et al. Rapid isotropic 3D-sodium MRI of the knee joint in vivo at 7T. *J Magn Reson Imaging*. Sep 2009;30(3):606-614.
20. Chang G, Pakin SK, Schweitzer ME, Saha PK, Regatte RR. Adaptations in trabecular bone microarchitecture in Olympic athletes determined by 7T MRI. *J Magn Reson Imaging*. May 2008;27(5):1089-1095.
21. Zuo J, Bolbos R, Hammond K, Li X, Majumdar S. Reproducibility of the quantitative assessment of cartilage morphology and trabecular bone structure with magnetic resonance imaging at 7 T. *Magn Reson Imaging*. May 2008;26(4):560-566.
22. Krug R, Carballido-Gamio J, Banerjee S, et al. In vivo bone and cartilage MRI using fully-balanced steady-state free-precession at 7 tesla. *Magn Reson Med*. Dec 2007;58(6):1294-1298.
23. Stahl R, Krug R, Kelley DA, et al. Assessment of cartilage-dedicated sequences at ultra-high-field MRI: comparison of imaging performance and

- diagnostic confidence between 3.0 and 7.0 T with respect to osteoarthritis-induced changes at the knee joint. *Skeletal Radiol.* Aug 2009;38(8):771-783.
24. Behr B, Stadler J, Michaely HJ, Damert HG, Schneider W. MR imaging of the human hand and wrist at 7 T. *Skeletal Radiol.* Sep 2009;38(9):911-917.
  25. Friedrich KM, Chang G, Vieira RL, et al. In vivo 7.0-tesla magnetic resonance imaging of the wrist and hand: technical aspects and applications. *Semin Musculoskelet Radiol.* Mar 2009;13(1):74-84.
  26. Gambarota G, Veltien A, Klomp D, Van Alfen N, Mulkern RV, Heerschap A. Magnetic resonance imaging and T2 relaxometry of human median nerve at 7 Tesla. *Muscle Nerve.* Sep 2007;36(3):368-373.
  27. Van de Moortele PF, Akgun C, Adriany G, et al. B(1) destructive interferences and spatial phase patterns at 7 T with a head transceiver array coil. *Magn Reson Med.* Dec 2005;54(6):1503-1518.
  28. Roemer PB, Edelstein WA, Hayes CE, Souza SP, Mueller OM. The NMR phased array. *Magn Reson Med.* Nov 1990;16(2):192-225.
  29. Griswold MA, Jakob PM, Heidemann RM, et al. Generalized autocalibrating partially parallel acquisitions (GRAPPA). *Magn Reson Med.* Jun 2002;47(6):1202-1210.
  30. Porter JR, Wright SM, Reykowski A. A 16-element phased-array head coil. *Magn Reson Med.* Aug 1998;40(2):272-279.
  31. Firbank MJ, Coulthard A, Harrison RM, Williams ED. A comparison of two methods for measuring the signal to noise ratio on MR images. *Phys Med Biol.* Dec 1999;44(12):N261-264.
  32. Yarnykh VL. Actual flip-angle imaging in the pulsed steady state: a method for rapid three-dimensional mapping of the transmitted radiofrequency field. *Magn Reson Med.* Jan 2007;57(1):192-200.
  33. Seeber DA, Jevtic I, Menon A. Floating shield current suppression trap. *Concepts in Magnetic Resonance Part B-Magnetic Resonance Engineering.* Apr 2004;21B(1):26-31.
  34. *CST MICROWAVE STUDIO®*, CST GmbH [computer program]. Version User Manual Version 2009. Darmstadt, Germany.

35. Christ A, Kainz W, Hahn EG, et al. The Virtual Family--development of surface-based anatomical models of two adults and two children for dosimetric simulations. *Phys Med Biol*. Jan 21 2010;55(2):N23-38.
36. International Electrotechnical Commission. Medical electrical equipment - Part 2-33: Particular requirements for the safety of magnetic resonance diagnostic devices. *IEC 60601-2-33*. Vol 2002.
37. Bitz A, Brote I, Orzada S, et al. An 8-channel add-on RF shimming system for whole-body 7 Tesla MRI including real-time SAR monitoring. Paper presented at: Proceedings 17th Scientific Meeting, International Society for Magnetic Resonance in Medicine; April, 2009; Honolulu.
38. Brote I, Orzada S, Kraff O, et al. A Multi-Channel SAR Prediction and Online Monitoring System at 7T. Paper presented at: Proceedings 17th Scientific Meeting, International Society for Magnetic Resonance in Medicine; April, 2009; Honolulu.
39. Katscher U, Bornert P, Leussler C, van den Brink JS. Transmit SENSE. *Magn Reson Med*. Jan 2003;49(1):144-150.
40. Zhu Y. Parallel excitation with an array of transmit coils. *Magn Reson Med*. Apr 2004;51(4):775-784.
41. Ibrahim TS, Lee R, Baertlein BA, Abduljalil AM, Zhu H, Robitaille PM. Effect of RF coil excitation on field inhomogeneity at ultra high fields: a field optimized TEM resonator. *Magn Reson Imaging*. Dec 2001;19(10):1339-1347.
42. Metzger GJ, Snyder C, Akgun C, Vaughan T, Ugurbil K, Van de Moortele PF. Local B1+ shimming for prostate imaging with transceiver arrays at 7T based on subject-dependent transmit phase measurements. *Magn Reson Med*. Feb 2008;59(2):396-409.
43. Duensing GR, Brooker HR, Fitzsimmons JR. Maximizing signal-to-noise ratio in the presence of coil coupling. *J Magn Reson B*. Jun 1996;111(3):230-235.
44. Wang J. A novel method to reduce the signal coupling of surface coils for MRI. *Proceedings of the 4th Annual Meeting of ISMRM*. Vol New York 1996:1434.
45. Lian J, Roemer PB, Inventors. MRI RF Coils. US patent 5,804,969 1998.



46. Nabeshima T, Takahashi T, Matsunaga Y, Yamamoto E, Inventors. RF probe for MRI. US patent 5,489,847/1996.
47. Weiger M, Pruessmann KP, Leussler C, Roschmann P, Boesiger P. Specific coil design for SENSE: a six-element cardiac array. *Magn Reson Med*. Mar 2001;45(3):495-504.
48. Graesslin I, Falaggis K, Vernickel P, et al. Safety Considerations Concerning SAR During RF Amplifier Malfunctions in Parallel Transmission. Paper presented at: Proceedings 14th Scientific Meeting, International Society for Magnetic Resonance in Medicine; April, 2006; Seattle, Washington.
49. Wiggins G, Zhang B, Duan Q, et al. 7 Tesla Transmit-Receive Array for Carotid Imaging: Simulation and Experiment. Paper presented at: Proceedings 17th Scientific Meeting, International Society for Magnetic Resonance in Medicine; April, 2009; Honolulu.

## Chapter 6 Summary

To date, the 7 T magnetic resonance imaging (MRI) scanner remains a pure research system and there is still a long way ahead till full clinical integration. Most examinations are performed in the brain where technical limitations and challenges are minimal compared to other parts of the human body. Key challenges are the absence of a body transmit radiofrequency (RF) coil as well as of dedicated RF coils in general, short RF wavelengths of the excitation field in the order of the dimensions of a human body leading to signal inhomogeneities, and severe limitations with respect to the specific absorption rate. They all result in a strong need for RF engineering and sequence optimization to explore the potential of MRI at 7 T, and to pave the way for its future clinical application. In this thesis, high-resolution MRI with a rather small field-of-view (FOV) in the head and neck region (parotid gland/duct and carotid arteries), and of the musculoskeletal system as well as with a very large FOV in the abdomen (spine) have been presented. Therefore, a variety of RF coils were used: from a commercially available single-loop coil to novel, specially developed phased array coils each consisting of eight loop elements. Methods to thoroughly characterize and test the developed RF coils were presented, including numerical simulations, bench and MRI measurements. Characterization with respect to performance for parallel acquisition techniques and an extensive compliance testing for patient safety were described in detail. All aspects of the engineering part, from design to optimization, and finally, to the in vivo application in volunteers and patients were covered. Since clinical applicability has always been the purpose, optimized imaging protocols along with a discussion on the clinical relevance was included in each study. Furthermore, for MRI of the parotid gland and duct 1.5 T and 7 T in vivo images were compared both quantitatively (signal- and contrast-to-noise ratio; SNR, CNR) and qualitatively (overall image quality and differentiability of various tissue).

The developed prototype coils were made of loop elements and used as combined transmit and receive RF arrays. Loop elements are known for their good SNR performance and can be found in most commercial coils for MR systems

ranging from 1.5 T to 7 T field strength. On the other hand, transmission line elements, for example, provide better transmit capabilities and can be found mainly in prototype coils used for abdominal imaging at 7 T. When developing novel RF coils for a first-time application at 7 T a compromise between receive and transmit parts has to be made, of course. Further optimization may be achieved by separating receive and transmit elements, and by following a combined approach which uses loop elements for reception and stripline elements for transmission. The presented RF coils and studies may serve as a basis for further developments in RF engineering and ultra-high field MR imaging at 7 T.

In conclusion, this work not only presents new RF loop coils and guidance for their characterization and testing but reveals potential clinical applicability of 7 T MRI outside the brain. The presented RF loop coils widely expand the options for clinical research at 7 T and advance the integration of this technology in a clinical setting.

## Chapter 7 Samenvatting

Tot op de dag van vandaag is de 7 Tesla kernspin resonantie scanner (MRI) puur een onderzoeksapparaat gebleven en is de weg richting volledige integratie in de kliniek nog lang. Huidige onderzoeken zijn meestal beperkt tot de hersenen waar de technische beperkingen en problemen minimaal zijn vergeleken met de rest van het menselijk lichaam. De grootste uitdagingen zijn (i) de afwezigheid van radiofrequente (RF) zendspoelen die het hele lichaam beslaan of, algemener gezien, zend/ontvangst spoelen die juist zeer specifiek zijn toegespitst op één bepaald deel van het lichaam, (ii) de korte golflengte van het radiofrequente veld die van dezelfde orde van grootte is als de afmetingen van het lichaam zelf wat leidt tot een inhomogeen signaal en (iii) zware beperkingen wat betreft de specifieke absorptie ratio (SAR). Hierdoor zijn er ontwikkelingen en optimalisaties nodig op het gebied van puls sequenties en RF om de volledige kracht van 7 T MRI te kunnen benutten en de weg vrij te maken voor toekomstig gebruik in de kliniek. Dit proefschrift bevat studies met hoge resolutie gecombineerd met een klein blikveld (FOV) gefocust op het hoofd/hals gebied alsmede op het spier/skelet systeem maar ook met een groot FOV over het abdomen (ruggengraat). Om dit te bereiken is een breed scala aan RF spoelen gebruikt: van commercieel verkrijgbare spoelen bestaande uit één enkele zogeheten 'loop', tot nieuwe speciaal ontwikkelde, zogeheten 'phased-array' spoelen bestaande uit acht loops. Methoden om de ontwikkelde spoelen grondig te karakteriseren en testen zijn hier gepresenteerd, waaronder numerieke simulaties en metingen in test opstellingen en in de MRI scanner. De prestaties op het gebied van parallelle acquisitie zijn gekarakteriseerd en uitgebreide tests met betrekking tot veiligheid van de patiënt zijn gedetailleerd beschreven. Alle aspecten van het maken van spoelen, van ontwerp tot optimalisatie en uiteindelijk de in vivo toepassing op vrijwilligers en patiënten zijn behandeld. Aangezien klinische toepasbaarheid altijd het doel is geweest, is elke studie voorzien van geoptimaliseerde protocollen voor de kliniek en een discussie van de klinische relevantie. Ook zijn er in vivo 1,5 T en 7 T beelden van de speeksel klier gemaakt die zowel kwantitatief (signaal ruis

verhouding; SNR, CNR) als kwalitatief (algehele beeldkwaliteit en onderscheidbaarheid van verschillende weefsels) zijn vergeleken.

De ontwikkelde prototype spoelen werden opgebouwd uit loop-elementen en gebruikt als gecombineerde zend en ontvangst RF spoelen. Loop-elementen staan bekend om hun goede SNR prestaties en worden gebruikt in de meeste commercieel verkrijgbare spoelen voor MR systemen variërend van 1,5 T tot 7 T veldsterkte. Aan de andere kant zijn er echter bijvoorbeeld ook transmissielijn-elementen, die betere zendeigenschappen hebben en veelal gebruikt worden in prototype 7 T spoelen voor het abdomen. Natuurlijk moet er bij het voor het eerst ontwikkelen van nieuwe RF spoelen voor toepassingen in 7 T MRI een compromis worden gemaakt tussen zend en ontvangst gedeeltes. Verdere optimalisatie kan worden bereikt door het zend en ontvangst gedeelte te scheiden en transmissielijn-elementen te gebruiken voor het zenden en loop-elementen voor de ontvangst. De hier gepresenteerde RF spoelen en studies kunnen als basis dienen voor verdere ontwikkelingen in RF techniek en ultra-hoog veld (7 T) MRI.

Concluderend, dit werk bevat niet alleen nieuwe RF spoel ontwerpen en een beschrijving van hoe deze te karakteriseren en testen maar laat ook de potentiële klinische toepasbaarheid zien van 7 T MRI buiten het brein. De hier gepresenteerde RF spoelen verbreden de mogelijkheden van klinisch onderzoek op 7 T en helpen de integratie van deze technologie in de kliniek een stap vooruit.

## Acknowledgement

Of course, the work on this doctoral thesis was accomplished neither over night nor by me alone. In fact, it would never have been possible without the help and support of many people who I would like to express my gratitude.

First and foremost, I thank Mark Ladd and Harald Quick for taking me without medical or MR physics background as a PhD student, for your continuous support, and, especially, for providing such excellent starting conditions. Thank you for giving me the opportunity to spend a couple of months in Boston and gain first experience with the 7T system long before our own system was installed. Through your guidance and friendship the physics group in Essen became renowned for a lot of things: for some of the world's first and best 7T images and RF technology, for being a small but very effective group with a great spirit, and for lots of merry evenings during conference trips. I am proud and grateful to be part of this group.

I thank my promotor David Norris and co-promotor Harald Quick for giving me the opportunity to do the public defense of this thesis at the University of Twente, as the regulations were new to everyone of us. Thanks for your support and lots of emails where we discussed the rules and procedures.

I owe a very special thank you to three colleagues in particular. Jens Theysohn, I most enjoyed the 2 years of sharing the office with you and I cannot think of any better radiologist at my side to "play around" at the 7T and try out new projects. I hope there will be many more conference trips for the two of us together where we can test another rented SUV for its off-road performance or sleep in clammy tent in the bear country. Andreas Bitz, thank you for your continuous support with the numerical simulations and your theoretic background. Your knowledge and commitment have pushed a lot of projects of our group. I also enjoyed your friendship during some trips we did together after conferences. Stefan Kruszona, you were a great student and friend, and your work contributed a lot to this thesis.

Very big thanks go out to the whole Erwin L. Hahn Institute where just everybody is committed not only to keep the group's spirit high, but has worked hard and helped to

make the institute internationally known within just a few years. You are all part of that productive working atmosphere I have esteemed right from the beginning. In particular, I want to thank Susanne Ladd for always having time to discuss the human anatomy, images, and their clinical relevance. Thanks Stefan Maderwald and Stephan Orzada for your inspiring ideas and knowledge in Matlab or MR sequences. Elke Gizewski, thank you for your support in neuroradiology. What would we do without our best volunteer, Ivonne Braun, or without our excellent radiographer Lena Schäfer? Thanks Beate Fraß for digging up funding in no time to cover the printing costs for two of my publications in Investigative Radiology.

Furthermore, I think, the institute and I have gained a lot from the collaboration with our colleagues from Nijmegen and also from discussions and regular exchanges of experiences with our friends from Utrecht and Leiden. Thank you.

For his kind contribution of the Dutch translation of the summary, I thank Peter Koopmans.

I also thank Larry Wald, Christopher and Graham Wiggins, as well as Andreas and Melanie Potthast for the wonderful time in Boston. You have welcomed me and Simone with open arms, and I have learned a lot from you about RF coils and the 7T system. It was a great time working with you at the Martinos Center.

Last but not least, I owe a very big thank you to my family. Mutti und Vati, ganz lieben Dank, dass Ihr mir das hier alles ermöglicht und mich ununterbrochen unterstützt habt. Ihr habt mir nicht nur das Studium in Aachen und Edinburgh ermöglicht, sondern vor allem Simone und mich nach Davids Geburt in vielerlei Hinsicht sehr stark unterstützt. Ebenso möchte ich an dieser Stelle Dir, Hildegard, für die gleiche Unterstützung und liebevolle Aufnahme in Deine Familie danken. Torsten, ich danke Dir, dass Du immer an mich geglaubt hast und ich mir einfach keinen besseren Bruder vorstellen kann.

Simone, ich kann gar nicht in Worte fassen, was Du mir bedeutest. Du bist der liebste und wunderbarste Mensch auf dieser Welt und ich bin unbeschreiblich glücklich, mit Dir zusammen leben zu dürfen. Du hast mich zwar auch schon im

Studium unterstützt, aber noch viel mehr während der Jahre der Doktorarbeit. Danke für Dein großes Verständnis, dass Wissenschaft nicht immer planbar ist, Arbeitstage spontan sehr lang werden können und gerade vor den deadlines auch mal das eine oder andere Wochenende drauf geht. Danke dass ich auch ohne Dich und David stets ein paar Urlaubstage an die eh schon recht langen Konferenzreisen dranhängen durfte. Vor allem aber danke ich Dir für unseren liebevollen und tollen Sohn David und sein gerade in Dir heranwachsendes Geschwisterchen.

David, auch wenn Du jetzt noch zu klein bist, das hier zu lesen, möchte ich Dir für Deine Liebe danken. Ich bin wahnsinnig stolz auf Dich und so glücklich, Dich aufwachsen zu sehen. Es tut mir leid, dass ich morgens nie so lange mit Dir spielen kann und zur Arbeit muss, und abends auch nicht immer so früh zu Hause bin. Glaube mir, am liebsten wäre ich den ganzen Tag nur mit Dir und Mama zusammen. Danke Euch allen!



## Curriculum Vitae

**Oliver Kraff**, born November 7<sup>th</sup>, 1977 in Mönchengladbach, Germany;  
married with Simone Leyting since 2008 and father of David A. Kraff, born in 2008.

### Education

---

10/1998 – 01/2005	Physics studies at the Rheinisch-Westfälisch Technische Hochschule Aachen, Aachen, Germany
11/2003 – 11/2004	Diploma thesis in High Energy Physics

### Work Experience

---

since 05/2005	PhD candidate at the Dept. of Diagnostic and Interventional Radiology and Neuroradiology, University Hospital Essen, and researcher at the Erwin L. Hahn Institute for Magnetic Resonance Imaging, University Duisburg-Essen, Germany
---------------	---

### International Experience

---

09/2001 – 07/2002	Studying Physics and Astronomy at the University of Edinburgh, Scotland
02/2004	Undergraduate research at the accelerator laboratory Fermilab in Batavia IL, USA
10/2005 – 02/2006	Visiting researcher at the Athinoula A. Martinos Center for Biomedical Imaging, Charlestown MA, USA

### Stipends

---

10/2005 – 03/2008	Research stipend, Dr. Werner Jackstädt Stiftung, Wuppertal
2006 – 2010	Educational stipends, International Society for Magnetic Resonance in Medicine, Berkeley CA, USA
2010, 2011	Travel stipends, German Academic Exchange Service

### Awards

---

2010	Toshiba Research Award, given by the German Society of Medical Physics
------	--

### Scientific Publications

---

Original papers	5 as first author; 20 as co-author
Conference abstracts	17 as first author; > 50 as co-author

## Curriculum Vitae

Oliver Kraff was born in Mönchengladbach, Germany on the 7<sup>th</sup> of November 1977. He grew up with his parents, Anton and Edith Kraff, and older brother, Torsten Kraff. After completing secondary education in 1997 and civil service in 1998, Oliver moved to Aachen to start studying Physics at the Rheinisch-Westfälisch Technische Hochschule Aachen. In 2001, Oliver spent a year abroad at the University of Edinburgh, Scotland, and studied Physics and Astronomy. He returned to Aachen and started in 2003 his diploma thesis in High Energy Physics about "Search for New Physics in Proton-Antiproton Collisions in Final States with Leptons and Jets" where he had the opportunity to visit the accelerator laboratory Fermilab in Batavia, Illinois in 2004. He obtained his diploma in Physics (Diplom-Physiker) in January 2005.

Following his time in Aachen, Oliver moved to Essen to commence his Ph.D. research in the group of Prof. Dr. sc. techn. Mark E. Ladd and Prof. Dr. rer. medic. Harald H. Quick at the Department for Diagnostic and Interventional Radiology and Neuroradiology, University Hospital Essen. After a few months he was sent to the Athinoula A. Martinos Center for Biomedical Imaging at the Massachusetts General Hospital in Charlestown, Massachusetts, to gain first experience with a 7 Tesla MRI system in the group of Prof. Dr. Lawrence L. Wald. When he returned to Essen, Oliver helped with the planning and installation of the 7 Tesla MRI lab at the newly founded Erwin L. Hahn Institute for Magnetic Resonance Imaging and was among the very first researchers to work on the MRI system in Essen. Since then he enjoyed giving technical support for the 7 Tesla MRI system, setting up clinical studies, and he has found a strong interest in developing radiofrequency coils. During his Ph.D. studies, Oliver successfully applied for a research stipend at the Dr. Werner Jackstädt Stiftung and received several educational stipends from the International Society for Magnetic Resonance in Medicine as well as travel stipends from the German Academic Exchange Service. He has also been awarded with the biannual Toshiba Research Award 2010 by the German Society of Medical Physics.

In the meantime, in 2008 Oliver married his wife Simone Leyting who gave birth to their son David Anton in October 2008. As a family they are still living in Essen.

## Peer review publications

Dammann P, **Kraff O**, Wrede KH, Oezkan N, Orzada S, Mueller OM, Sandalcioglu IE, Sure U, Gizewski ER, Ladd ME, Gasser T. Evaluation of Hardware-Related Geometrical Distortion in Structural MRI at 7 Tesla for Image-Guided Applications in Neurosurgery. *Acad Radiol.*, 2011 May 4. [Epub ahead of print]

Theysohn JM, **Kraff O**, Maderwald S, Barth M, Ladd SC, Forsting M, Ladd ME, Gizewski ER. 7 Tesla MRI of microbleeds and white matter lesions as seen in vascular dementia. *J Magn Reson Imaging* 2011 Apr; 33(4):782-91.

Umutlu L, **Kraff O**, Orzada S, Fischer A, Kinner S, Maderwald S, Antoch G, Quick HH, Forsting M, Ladd ME, Lauenstein TC. Dynamic contrast-enhanced renal MRI at 7 Tesla: preliminary results. *Invest Radiol.* 2011 Feb 11. [Epub ahead of print]

Umutlu L, Orzada S, Kinner S, Maderwald S, Brote I, Bitz AK, **Kraff O**, Ladd SC, Antoch G, Ladd ME, Quick HH, Lauenstein TC. Renal imaging at 7 Tesla: preliminary results. *Eur Radiol.* 2011 Apr; 21(4):841-9.

**Kraff O**, Bitz AK, Breyer T, Kruszona S, Maderwald S, Brote I, Gizewski ER, Ladd ME, Quick HH. A transmit/receive RF array for imaging the carotid arteries at 7 Tesla: Coil design and first in-vivo results. *Invest Radiol.* 2011 Apr; 46(4): 246-254.

**Kraff O**, Bitz AK, Dammann P, Ladd SC, Ladd ME, Quick HH. An eight-channel transmit/receive multi-purpose coil for musculoskeletal MR imaging at 7 Tesla. *Med Phys.*, 2010 Dec; 37(12): 6368-76.

Kahlert P, Eggebrecht H, Plicht B, **Kraff O**, McDougall I, Decker B, Erbel R, Ladd ME, Quick HH. Towards real-time cardiovascular magnetic resonance-guided transarterial aortic valve implantation: in vitro evaluation and modification of existing devices. *J Cardiovasc Magn Reson.* 2010 Oct; 13:12-58.

Noebauer-Huhmann IM, Szomolanyi P, Juras V, **Kraff O**, Ladd ME, Trattinig S. Gadolinium-based magnetic resonance contrast agents at 7 Tesla: in vitro T1 relaxivities in human blood plasma. *Invest Radiol.* 2010 Sep; 45(9):554-8.

Umutlu L, Maderwald S, **Kraff O**, Theysohn JM, Kuemmel S, Hauth EA, Forsting M, Antoch G, Ladd ME, Quick HH, Lauenstein TC. Dynamic contrast-enhanced breast MRI at 7 Tesla utilizing a single-loop coil: a feasibility trial. *Acad Radiol*. 2010 Aug; 17(8):1050-6.

Mönninghoff C, Maderwald S, Theysohn JM, Schütt P, Gauler T, **Kraff O**, Ladd ME, Ladd SC, Wanke I. Imaging of brain metastases of bronchial carcinomas with 7 T MRI - initial results. *Rofo*. 2010 Sep; 182(9):764-72.

Schlamann M, Voigt MA, Maderwald S, Bitz AK, **Kraff O**, Ladd SC, Ladd ME, Forsting M, Wilhelm H. Exposure to high-field MRI does not affect cognitive function. *J Magn Reson Imaging*. 2010 May; 31(5):1061-6.

Moenninghoff C, **Kraff O**, Schlamann M, Ladd ME, Katsarava Z, Gizewski ER. Assessing a dysplastic cerebellar gangliocytoma (Lhermitte-Duclos disease) with 7T MR imaging. *Korean J Radiol*. 2010 Mar; 11(2):244-8.

Breyer T, Wanke I, Maderwald S, Woermann FG, **Kraff O**, Theysohn JM, Ebner A, Forsting M, Ladd ME, Schlamann M. Imaging of patients with hippocampal sclerosis at 7 Tesla: initial results. *Acad Radiol*. 2010 Apr; 17(4):421-6.

Schlamann M, Maderwald S, Becker W, **Kraff O**, Theysohn JM, Mueller O, Sure U, Wanke I, Ladd ME, Forsting M, Schaefer L, Gizewski ER. Cerebral cavernous hemangiomas at 7 Tesla: initial experience. *Acad Radiol*. 2010 Jan; 17(1):3-6.

**Kraff O**, Bitz AK, Kruszona S, Orzada S, Schaefer LC, Theysohn JM, Maderwald S, Ladd ME, Quick HH. An eight-channel phased array RF coil for spine MR imaging at 7 T. *Invest Radiol*. 2009 Nov; 44(11):734-40.

Moenninghoff C, Maderwald S, Theysohn JM, **Kraff O**, Ladd ME, El Hindy N, van de Nes J, Forsting M, Wanke I. Imaging of adult astrocytic brain tumours with 7 T MRI: preliminary results. *Eur Radiol*. 2010 Mar; 20(3):704-13.

**Kraff O**, Theysohn JM, Maderwald S, Kokulinsky PC, Dogan Z, Kerem A, Kruszona S, Ladd ME, Gizewski ER, Ladd SC. High-resolution MRI of the human parotid gland and duct at 7 Tesla. *Invest Radiol*. 2009 Sep; 44(9):518-24.

Kollia K, Maderwald S, Putzki N, Schlamann M, Theysohn JM, **Kraff O**, Ladd ME, Forsting M, Wanke I. First clinical study on ultra-high-field MR imaging in patients with multiple sclerosis: comparison of 1.5T and 7T. *AJNR Am J Neuroradiol*. 2009 Apr; 30(4):699-702.

Mönninghoff C, Maderwald S, Theysohn JM, **Kraff O**, Ladd SC, Ladd ME, Forsting M, Quick HH, Wanke I. Evaluation of intracranial aneurysms with 7 T versus 1.5 T time-of-flight MR angiography - initial experience. *Rofo*. 2009 Jan; 181(1):16-23.

Theysohn JM, **Kraff O**, Maderwald S, Schlamann MU, de Greiff A, Forsting M, Ladd SC, Ladd ME, Gizewski ER. The human hippocampus at 7 T--in vivo MRI. *Hippocampus*. 2009 Jan; 19(1):1-7.

Welsch GH, Mamisch TC, Hughes T, Zilkens C, Quirbach S, Scheffler K, **Kraff O**, Schweitzer ME, Szomolanyi P, Trattnig S. In vivo biochemical 7.0 Tesla magnetic resonance: preliminary results of dGEMRIC, zonal T2, and T2\* mapping of articular cartilage. *Invest Radiol*. 2008 Sep; 43(9):619-26.

Maderwald S, Ladd SC, Gizewski ER, **Kraff O**, Theysohn JM, Wicklow K, Moenninghoff C, Wanke I, Ladd ME, Quick HH. To TOF or not to TOF: strategies for non-contrast-enhanced intracranial MRA at 7 T. *MAGMA*. 2008 Mar; 21(1-2):159-67.

Theysohn JM, Maderwald S, **Kraff O**, Moenninghoff C, Ladd ME, Ladd SC. Subjective acceptance of 7 Tesla MRI for human imaging. *MAGMA*. 2008 Mar; 21(1-2):63-72.

Bieri O, Mamisch TC, Trattnig S, **Kraff O**, Ladd ME, Scheffler K. Optimized spectrally selective steady-state free precession sequences for cartilage imaging at ultra-high fields. *MAGMA*. 2008 Mar; 21(1-2):87-94.

**Kraff O**, Theysohn JM, Maderwald S, Saylor C, Ladd SC, Ladd ME, Barkhausen J.  
MRI of the knee at 7.0 Tesla. *Rofo*. 2007 Dec; 179(12):1231-5.